PH.D. DISSERTATION

A WIDE DYNAMIC RANGE MULTI-MODE BAND-PASS CONTINUOUS-TIME DELTA-SIGMA MODULATOR EMPLOYING HIGH-Q SINGLE-OPAMP RESONATOR

높은 품질 인자 단일-연산증폭기 기반의 공진기를 이용한 넓은 동작 대역의 다중 모드 밴드-패스 연속-시간 델타-시그마 모듈레이터

BY

SUSIE Kim

AUGUST 2018

DEPARTMENT OF ELECTRICAL ENGINEERING AND
COMPUTER SCIENCE
COLLEGE OF ENGINEERING
SEOUL NATIONAL UNIVERSITY

A WIDE DYNAMIC RANGE MULTI-MODE BAND-PASS CONTINUOUS-TIME DELTA-SIGMA MODULATOR EMPLOYING HIGH-Q SINGLE-OPAMP RESONATOR

높은 품질 인자 단일-연산증폭기 기반의 공진기를 이용한 넓은 동작 대역의 다중 모드 밴드-패스 연속-시간 델타-시그마 모듈레이터

지도교수 김 수 환

이 논문을 공학박사 학위논문으로 제출함

2018년 8 월

서울대학교 대학원

전기컴퓨터 공학부

김 수 지

김수지의 공학박사 학위논문을 인준함

2018년 8 월

위 원 장 : 이 혁 재 (印)

부위원장 : 김 수 환 (印)

위 원 : 홍 용 택 (印)

위 원 : 조 준 수 (印)

위 원 : 이 현 중 (印)

ABSTRACT

A WIDE DYNAMIC RANGE MULTI-MODE BAND-PASS CONTINUOUS-TIME DELTA-SIGMA MODULATOR EMPLOYING HIGH-Q SINGLE-OPAMP RESONATOR

SUSIE KIM
DEPARTMENT OF ELECTRICAL ENGINEERING AND
COMPUTER SCIENCE
COLLEGE OF ENGINEERING
SEOUL NATIONAL UNIVERSITY

Continuous-wave (CW) Doppler signal, which utilizes pencil transducer with the center frequency of a few MHz to tens of MHz range, is suitable for measuring the high blood velocity in the ultrasound imaging system. The CW Doppler received signal consists of a strong signal from stationary tissue and the much weaker Doppler signal from moving blood. Since the Doppler signal is 40–60 dB below the strong signal, CW Doppler receiver is required to achieve a wide dynamic range (DR). The RF-to-baseband mixing process, which limits the performance of the CW Doppler receiver, can be moved from analog domain to digital domain by using a band-pass continuous-time delta-sigma modulator (BPCTDSM). Since the signal processing for correcting I/Q mismatch can be easily implemented in the digital domain, the CW Doppler receiver that uses BPCTDSM is more efficient than the conventional one. The performance of the BPCTDSM depends

on the quality factor (Q) of a resonator. When Q falls below the ratio of the center frequency to the signal bandwidth, F_C/F_B, the performance degradation becomes significant. In CW Doppler receiver, the center frequencies are in the range of up to tens of MHz and the signal bandwidth is typically 200 kHz, which results in large F_C/F_B and therefore requires high Q resonator.

Recently, a single-opamp resonator is widely used to decrease the power consumption. However, compared to a conventional active resonator, which uses two opamps, the single-opamp resonator is more vulnerable to the effect of finite gain-bandwidth (GBW) of an opamp that results in the degradation of Q. Using a multi-stage opamp can be used to achieve high GBW, but requires enhanced specifications for an opamp as F_C/F_B increases and therefore increases power consumption. Compensating the coefficients of the loop filter that restores the modified noise transfer function of the modulator due to the GBW can be utilized to alleviate to the effect of finite GBW. Additional feedback path can also compensate the loop delay caused by the finite GBW. Although these approaches can be used regardless of F_C/F_B, the compensated coefficients are not guaranteed to be implemented using unit resistance and unit capacitance, which is important to reduce the mismatch between the passive components. Also, an additional feedback DAC is required to implement the compensation feedback path.

To alleviate the effect of finite GBW of an opamp to Q of the resonator, we propose a high Q single-opamp resonator, which compensates the degradation of Q by using a positive feedback resistor while not burdening to the design of an opamp. Also, the passive components that used in the single-opamp resonator are designed by using a unit

resistance and a unit capacitance to minimize the effect of mismatch. In this thesis, a multi-mode wide DR BPCTDSM for pencil probe application is presented. Our BPCTDSM can be applied to measure the blood flow in the heart, vessel, and gingiva, which uses the center frequencies of 2 MHz, 5 MHz, and 20 MHz, respectively. By utilizing the proposed high Q single-opamp resonator, it is available to achieve wide DR despite the finite GBW of an opamp. The prototype is implemented in 180 nm CMOS technology with an active area of 0.845 mm^2. The experimental results show DRs of 88.15/88.42/90.39 dB and peak signal-to-noise distortion ratios of 70.2/70.03/68.58 dB in cardiac/vascular/ gingival-modes. The power consumptions are 14.73/18.77/25.75 mW in cardiac/vascular/ gingival-modes from the supply voltage of 1.8 V.

Keywords: wide dynamic range, band-pass continuous-time delta-sigma modulator, high quality factor, single-opamp resonator, finite gain-bandwidth.
Student Number: 2011-20806

CONTENTS

LIST OF FIGURES

LIST OF TABLES

CHAPTER 1

INTRODUCTION

1.1 ULTRASOUND IMAGING SYSTEM

Ultrasound is one of the most widely used modalities in medical imaging. Ultrasound imaging is regularly used in cardiology, obstetrics, gynecology, abdominal imaging, etc. Its popularity arises from the fact that it provides high-resolution images without the use of ionizing radiation. It is also mostly non-invasive, although an invasive technique like intra-vascular imaging is also possible. Non-diagnostic use of ultrasound is finding increased use in clinical applications. There are also novel non-imaging uses of ultrasound like bone densitometer where the ultrasound speed difference is used to measure the depth or width of bones non-invasively. Compared to X-ray and computer tomography (CT) devices that exposes the human body to radiation, the ultrasound medical imaging has advantages in terms of safety, cost, and portability. Table 1.1.1 summarizes the characteristics of various imaging modalities [1.1.1].

In general, the acoustic spectrums in the range of a few MHz to tens of MHz are used for the ultrasound medical imaging. Frequencies of a few MHz (below 5 MHz) are

Table 1.1.1 Comparison of imaging modalities

Modality	**Ultrasound**	**X-ray**	**CT**	**MRI**
What is Imaged	Mechanical Properties	Mean Tissue Absorption	Tissue Absorption	Biochemistry
Spatial Resolution	0.3-3 mm	~1 mm	~1 mm	~1 mm
Penetration	3-25 cm	Excellent	Excellent	Excellent
Safety	Very Good	Ionizing Radiation	Ionizing Radiation	Very Good
Cost	Cheap	Cheap	Expensive	Very Expensive
Portability	Excellent	Good	Poor	Poor

used in the body imaging applications where significant penetration of the tissues is needed. These frequencies have the ability to penetrate the tissues to a depth of 15 to 20 cm and the return signals still have sufficient strength to form an image. As the frequency increases, the ultrasound is more strongly attenuated and the penetration is reduced. Frequencies from 7 to 10 MHz can be used in a small part imaging, such as visualization of an eye. In this case, the penetration of 4 to 5 cm is sufficient. Until now, the majority of the ultrasound medical imaging systems are performed from 1 to 10 MHz, new

applications are emerging in the high-frequency range from 10 to 40 MHz.

Figure 1.1.1 shows a block diagram of general ultrasound imaging system [1.1.2], [1.1.3]. The ultrasound imaging system is capable of generating images of internal organs and structure, mapping blood flow and tissue motion, and providing highly accurate blood velocity information by transmitting acoustic energy into the body, receiving the returning reflections, and processing the received signals. The system consists of transducers, high-voltage multiplexing, high-voltage transmitters, low-voltage receivers, digital beamfor-mers, beamformed digital-signal processing, and display processing.

The transducer transmits focused ultrasound energy that comes from the high-voltage transmitter into the body and receives the reflected energy. The type and size of the transducers are determined according to the applications [1.1.4]. Linear transducers are used for small parts requiring high resolution and typically involve shallow depths, which are widely used in cardio applications. Curved transducers are used for abdominal viewing due to good characteristics of resolution and penetration. Pencil transducers, also called continuous-wave (CW) Doppler probes, are used to measure blood flow and speed of sound in blood [1.1.5]. The utilized frequency of the transmitting signal in pencil transducer depends on the purpose of measuring which blood velocities. In general, the ultrasound energies of 2 MHz and 5 MHz are used to measure the blood velocities of heart and vessel, respectively [1.1.6]. A higher frequency of 20 MHz is used to measure the blood velocities of gingiva [1.1.7]. Various types of transducers are shown in Figure 1.1.2.

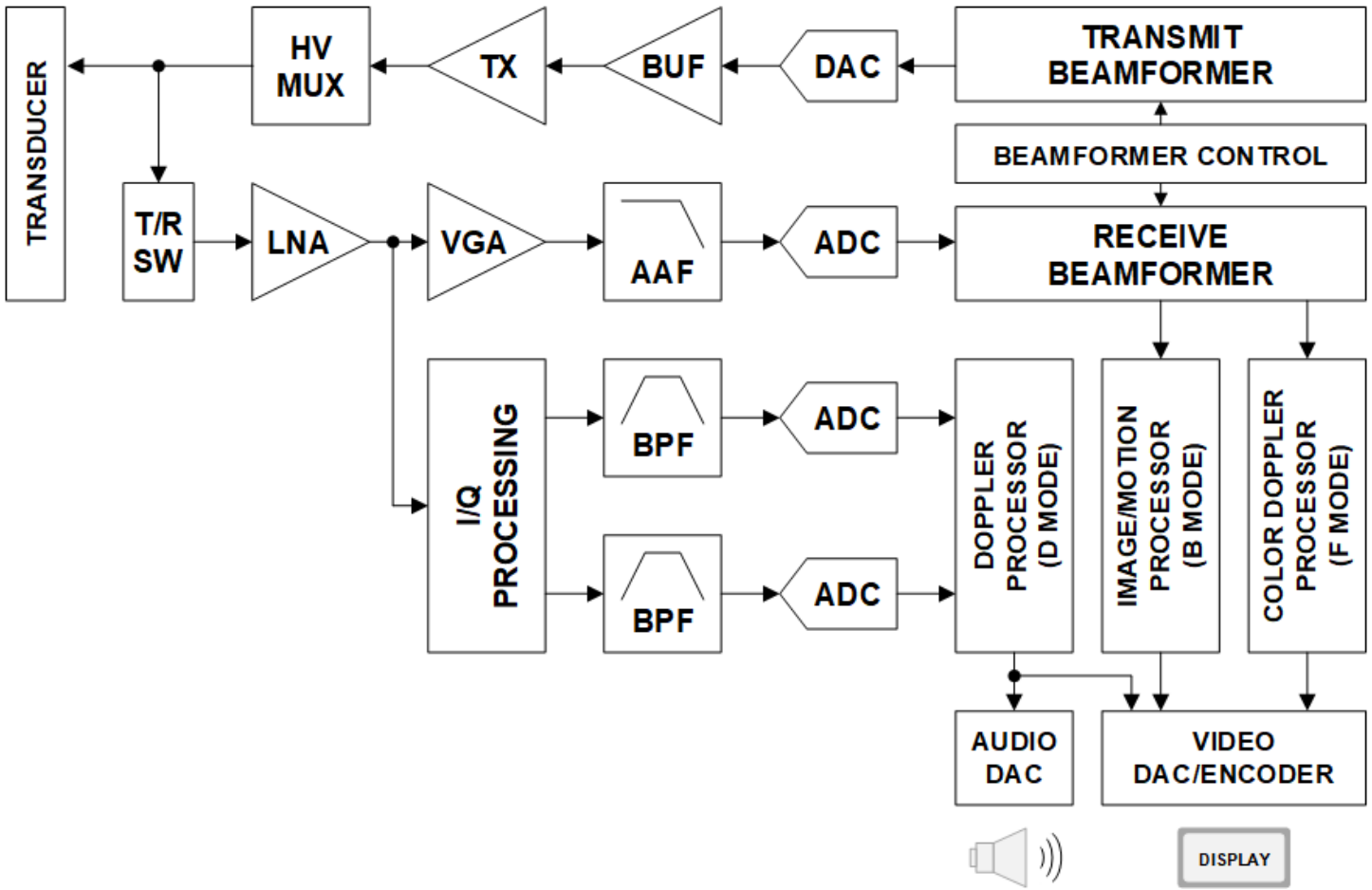

Figure 1.1.1 Block diagram of general ultrasound imaging system.

(a) (b)

(c) (d)

Figure 1.1.2 Various types of transducers; (a) linear transducer, (b) convex transducer, (c) phased array transducer, and (d) pencil type transducer.

www.alpinion.co.kr/kr/diagnostic/prd_transducer.asp

The ultrasound imaging system provides various kinds of transducers, which are optimized for specific diagnostic applications. The high-voltage multiplexer is used to connect a specific transducer and to a specific transmitter/receiver. Once the application to which the ultrasound imaging system is to be applied is determined, the digital

beamformer generates the appropriate digital transmit signals with the proper timing to produce a focused transmit signal. The digital transmit signals are converted to analog signals by using a digital-to-analog converter (DAC). The converted analog signals propagate toward the desired focal point through the high-voltage multiplexer and the transducer.

A reflected sound wave is produced as the sound waves pass through materials with different densities. The reflected energy is transferred to the low-voltage receiver through the transducer. The receiver can be classified to an image-path receiver and CW Doppler receiver. The image-path receiver consists of a low-noise amplifier (LNA), a variable-gain amplifier (VGA), an anti-aliasing filter (AAF), and an analog-to-digital converter (ADC). The CW Doppler receiver consists of a LNA, mixers, band-pass filters (BPFs), and ADCs. Depending on the imaging modes, the digitized output signals from the ADC are beamformed and signal processed for display and audio outputs.

1.2 ULTRASOUND ACQUISITION MODES

1.2.1 BRIGHTNESS MODE

In the past, amplitude mode (A-mode) imaging that displays the amplitude of a sampled voltage signal for a single sound wave as a function of time was used. A-mode imaging was used to measure the distance between two objects, however, the two objects could not be specified and no longer used in these days [1.1.3]. Brightness mode (B-mode) imaging uses the brightness to represent the amplitude of the sampled signal [1.1.3]. A 2D image is produced by sweeping the transmitted sound wave over the plane. It is typical to generate multiple sets of pulses to produce sound waves for each scan line, which are intended for a specific focal point along the scan line. By B-mode imaging, the field of the organs or tissues, which are intersected by the scanning plane, can be visualized. The shape of the visualized field varies depending on the probe; a sector with echo and abdominal probes and rectangular or trapezoid with superficial or vascular probes. Multiple images of the filed or frames appear on the screen every second that seems to move. A frame rate of at least 20 frames per second is required to provide a realistic movement. High reflection (e.g., bone), low reflection (e.g., muscle), and no reflection (e.g., water) are shown as white, grey, and black, respectively. The inner structures are displayed at the bottom of the screen and the structures near the surface are displayed at the top. Figure 1.2.1 shows an example of B-mode imaging.

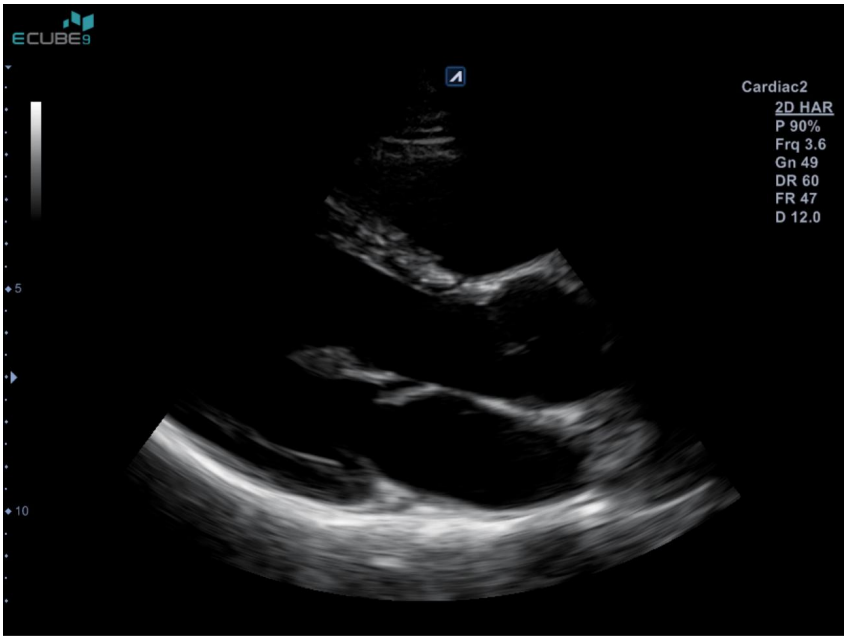

Figure 1.2.1 B-mode imaging.

http://www.alpinion.com/mobile/diagnostic/inc_clinical_image_view.asp?product=0306&gubun=2&sort=A&imgidx=587

1.2.2 DOPPLER MODE

Doppler mode (D-mode), which refers to pulse wave (PW) Doppler, color flow Doppler, and CW Doppler, displays the measured blood flow velocities over time by using Doppler effect, the shift in sound frequency or wavelength as the source moves with respect to the observer [1.1.6], [1.2.1], [1.2.2]. D-mode imaging is based on the change in frequency of the reflected ultrasound f_R, which is caused by the moving blood cells, as shown in Figure 1.2.2. Once the transmitted ultrasound f_T is backscattered off a target, it returns back to the transducer with a shift in frequency f_D, which can be

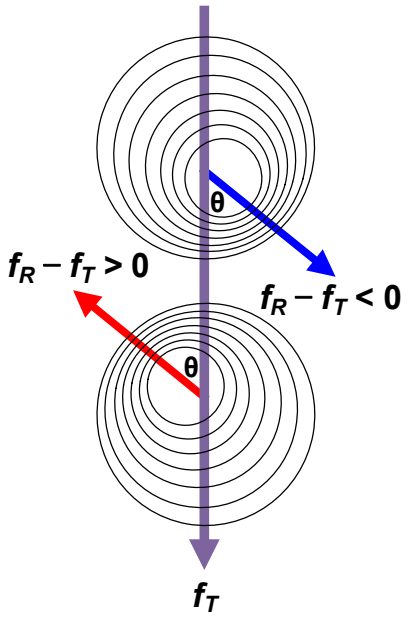

Figure 1.2.2 Doppler effect caused by the moving blood cells.

expressed as follows:

$$f_D = f_R - f_T = \frac{2v\cos\theta}{c_0} \cdot f_T \tag{1.2.1}$$

where c_0 is the speed of the sound in blood, v is the velocity of the blood cell, and θ is the angle of incidence between the ultrasound beam and the vector of v. When the target moves toward the ultrasound transducer, the Doppler shift is positive, and the reflected frequency will be higher. On the contrary, when the target moves away from the ultrasound transducer, the Doppler shift is negative and the reflected frequency will be

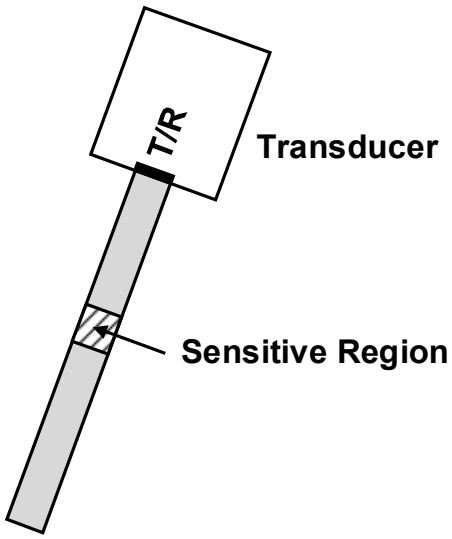

Figure 1.2.3 PW Doppler transducer.

lower. Since f_T, f_D, c_0, and θ are known variables, v can be calculated by rearranging (1.2.1) as follows:

$$v = \frac{c_0 f_D}{2\cos\theta f_T}. \tag{1.2.2}$$

PW Doppler is used for measuring the blood velocity and direction in a single point or a narrow space. The same transducer is used to transmit a pulsed signal to a particular depth D and then listens for the reflected signal from that appropriate depth, as shown in Figure 1.2.3. Due to the listening period, which is relative to the depth from which the velocities are sampled, the maximum velocity that can be measured by PW Doppler

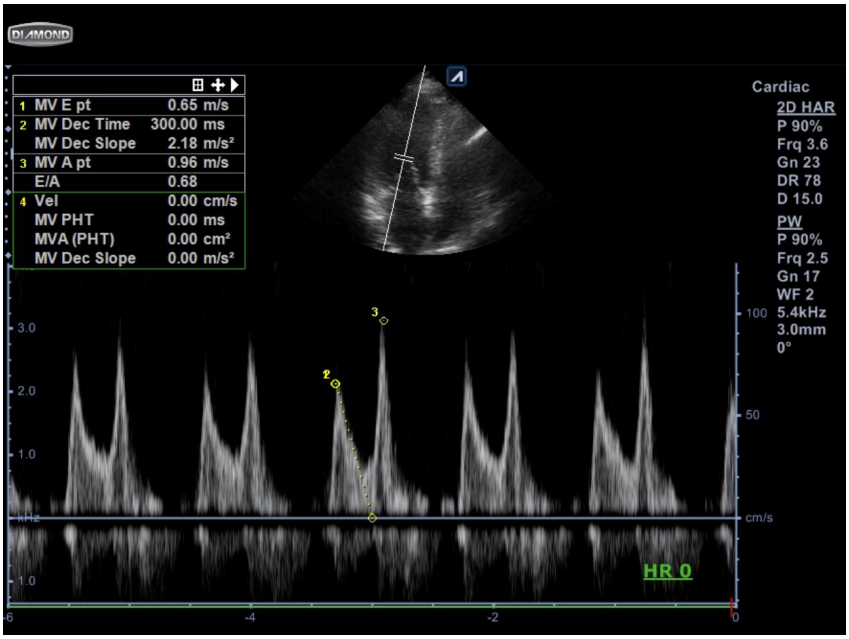

Figure 1.2.4 PW Doppler.

http://www.alpinion.com/mobile/diagnostic/inc_clinical_image_view.asp?product=0306&gubun=2&sort=A&imgidx=587

depends on the depth of the PW Doppler sample volume. The frequency of transmit-wait-receive cycle of the transducer is called pulse repetition frequency (PRF), which is $c/(2D)$. Since aliasing occurs if f_D exceeds PRF/2, the maximum velocity v_{MAX} that can be measured by PW Doppler at the depth can be derived as follows:

$$v_{MAX} = \frac{c^2}{8Df_T}. \tag{1.2.3}$$

Figure 1.2.4 shows an example of PW Doppler.

Color flow Doppler represents the velocity and direction of blood flow in a color

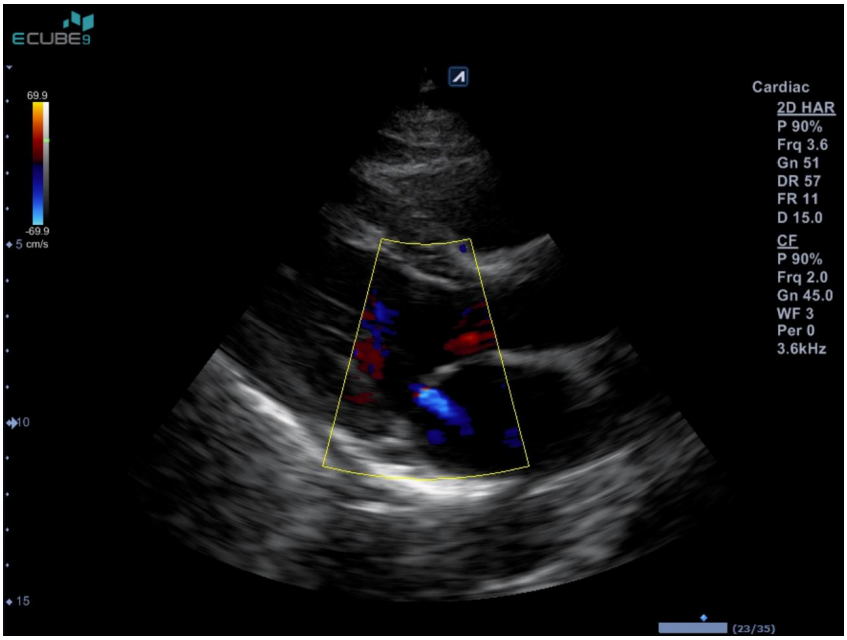

Figure 1.2.5 Color flow Doppler.

http://www.alpinion.com/mobile/diagnostic/inc_clinical_image_view.asp?product=0306&gubun=2&sort=A&imgidx=587

image with pulse wave Doppler signals, which is superimposed on a 2D image from B-mode imaging. In general, red denotes blood flow towards the transducer and blue denotes blood flow far away from the transducer. Green or white represents areas of turbulent flow. As the velocity increases, the displayed color becomes darker. Color flow Doppler reveals the cardiac blood flows from an anatomical point of view. Therefore, it is useful to visualize and semi-quantitatively evaluate regurgitant jets or other abnormal blood flows. Also, it can be used for the guidance of the precise location of the cursor in PW Doppler and CW Doppler. Color flow Doppler is usually utilized to image normal or abnormal blood flow in cardiac chambers, across valves, and inside vessels. Figure 1.2.5

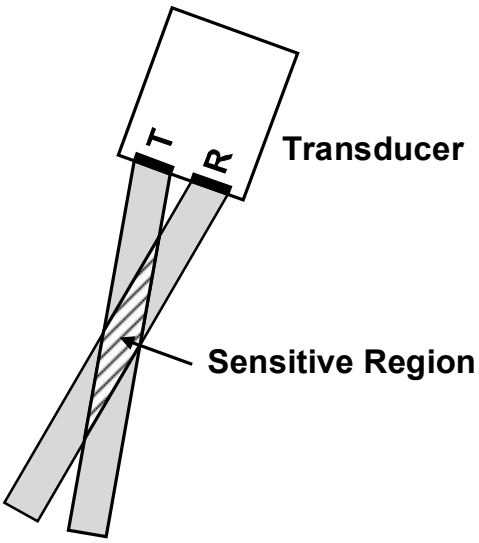

Figure 1.2.6 CW Doppler transducer.

shows an example of color flow Doppler.

CW Doppler measures blood velocities along an entire line of interrogation, which is depicted as an interrupted line on the 2D image sector. In contrast to PW Doppler, a sound wave at a single frequency is continuously transmitted from one piezoelectric element and a second piezoelectric element is used to continuously record the reflected sound wave, as shown in Figure 1.2.6. Since the received signal is recorded continuously, aliasing does not occur, and therefore CW Doppler is appropriate to measure very high blood flow velocity. However, the velocity location cannot be determined because the transducer continuously receives the reflected sound wave from various depths. Figure 1.2.7 shows an example of CW Doppler.

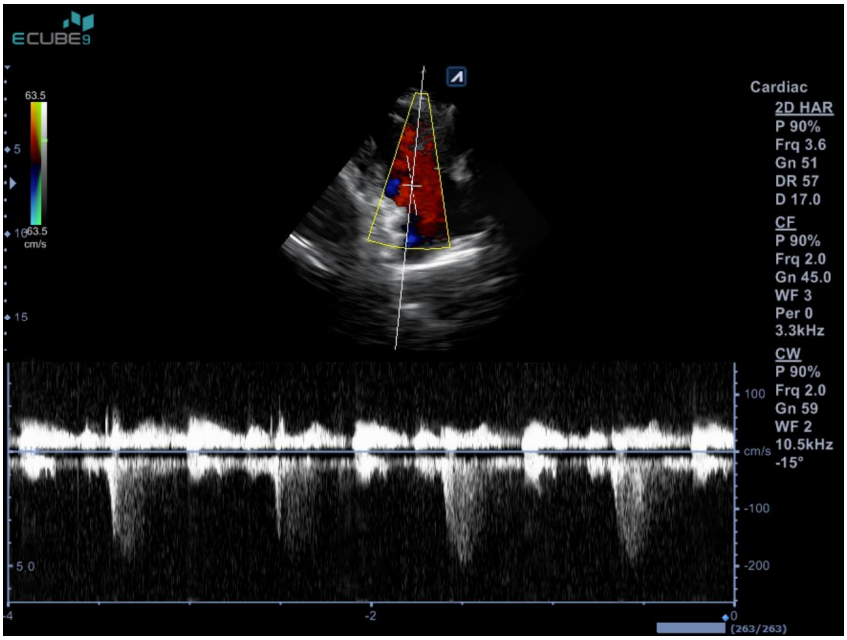

Figure 1.2.7 CW Doppler.

http://www.alpinion.com/mobile/diagnostic/inc_clinical_image_view.asp?product=0306&gubun=2&sort=A&imgidx=587

In either PW Doppler or CW Doppler, the range of velocities are displayed over time in a y-x axis system. The largest Doppler shifts correspond to peak velocities, and the smaller Doppler shifts correspond to lower velocities. From the spectral display, the information of the direction of velocity, maximum velocity, integral of velocity over time, mean velocity, and time intervals can be derived. Table 1.2.1 summarizes the characteristics of Doppler modes.

Table 1.2.1 Comparison of Doppler modes

	PW Doppler	**Color flow Doppler**	**CW Doppler**
Application	Measurement of Low Blood Velocity	Visualization of Blood Flows	Measurement of High Blood Velocity
Velocity Range	< 1.5 m/s	< 1 m/s	Up to 12 m/s
Sample Volume	Single Gate	Multiple Gate	Single Line
Tx/Rx Transducer	Same	Same	Different
Aliasing	Yes	Yes	No
Range Resolution	Yes	Yes	No
Image	Range of Velocities	Color Pixels on a 2D Image	Range of Velocities

1.3 CONTINUOUS-WAVE DOPPLER RECEIVER

As introduced above, CW Doppler is appropriate to accurately measure the high blood velocities, such as in heart, vessel, and gingiva. The transmitting ultrasound waves for CW Doppler are in the range of a few MHz to tens of MHz [1.1.5], [1.1.7]. To enhance the measurement accuracy, the jitter of the transmit signal should be minimized to avoid the phase noise. The received CW Doppler signal consists of a large signal from the stationary tissue (clutter), which is determined to the frequency of the transmit signal, and much smaller Doppler signal, which is in the range of 200 kHz around the clutter signal and 40 to 60 dB below the clutter signal [1.3.1], which results in wide dynamic range (DR) for CW Doppler receiver.

Conventional CW Doppler receiver extracts a received CW Doppler signal at the output of the LNA, as shown in Figure 1.3.1. Complex mixers at an LO frequency, which is equal to the transmit frequency, are then used to mix them to baseband for processing. The output signals of the mixers are band-pass filtered and converted to digital I/Q CW Doppler signals by ADCs. Using low-pass delta-sigma ADCs are adequate to achieve wide DR at low frequency. Although the transmit signal frequency changes, the mixers can convert the received signal into the same baseband frequency and therefore the requirements for the ADC does not change. However, the complex mixers occur phase and amplitude mismatches in I/Q channels, which are the significant issues that limit the performance of the receiver [1.3.2]. To alleviate the effect of mismatches between the I/Q channels, I/Q correction technique is necessary for the conventional CW Doppler receiver,

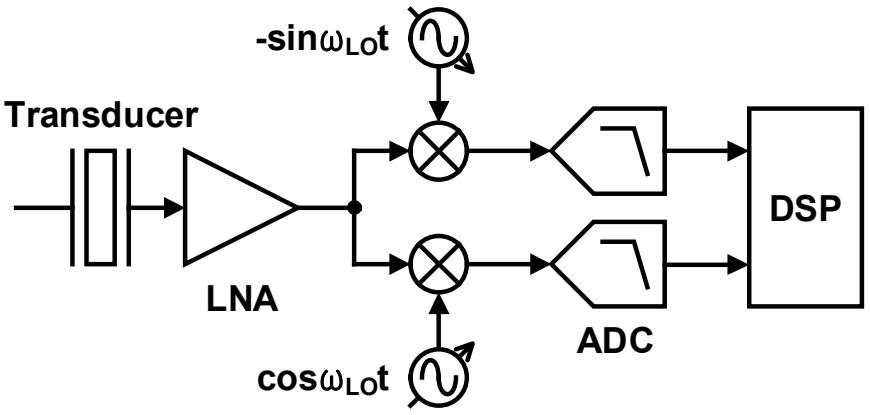

Figure 1.3.1 Block diagram of a conventional CW Doppler receiver.

which increases the complexity of the system. It is required to achieve wide DR for the mixer to transfer the signal from the LNA to the ADC without defect. However, implementing a wide DR mixer consumes too much power and hard to design in CMOS technology [1.3.3].

For the above reasons, a CW Doppler receiver that moves the mixing operation from the analog domain to digital domain can be a solution, as shown in Figure 1.3.2. A delta-sigma modulator (DSM) can be classified with low-pass DSM (LPDSM) and band-pass DSM (BPDSM) depending on the characteristics of the loop filter. By using a BPDSM, which passes the signal and suppresses the noise around a certain bandwidth based on the center frequency, the signal from the LNA can be directly converted to the digital signal without down-conversion [1.3.2]. Since the I/Q demodulation is performed in the digital domain, design complexity of the CW Doppler receiver remarkably decreases. In the

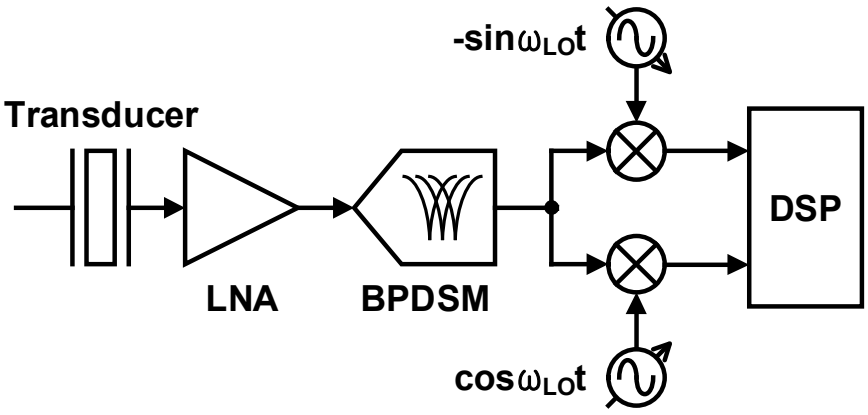

Figure 1.3.2 Block diagram of a CW Doppler receiver utilizing BPDSM.

conventional CW Doppler receiver, the input signal of the ADC is in the same frequency range. Since the received CW Doppler signal is demodulated after the analog-to-digital conversion, the BPDSM is required to be implemented that can adjust the center frequency corresponding to the transmit signal frequency. Figure 1.3.3 shows a block diagram of an ultrasound imaging system in which an analog mixer in the conventional CW Doppler receiver is replaced with an I/Q demodulation of the digital signal. In this thesis, we will introduce a band-pass continuous-time DSM (BPCTDSM) that achieves wide DR to be applied in CW Doppler receiver, which uses pencil transducers. The proposed BPCTDSM supports the center frequencies of 2 MHz, 5 MHz, and 20 MHz for measuring the blood flows of heart, vessel, and gingiva.

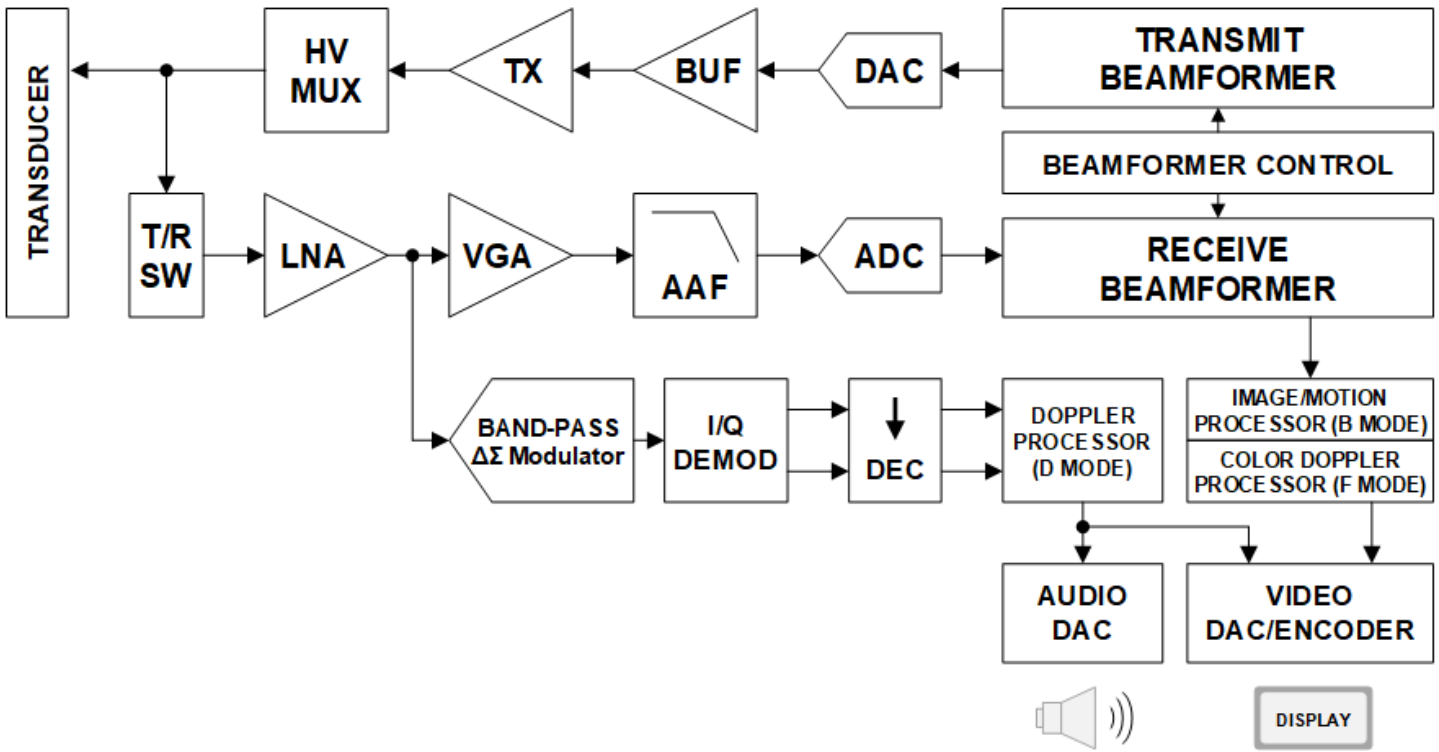

Figure 1.3.3 Block diagram of an ultrasound imaging system utilizing BPCTDSM with digital I/Q demodulation for CW Doppler receiver.

1.4 THESIS ORGANIZATION

This thesis is organized as follows. The fundamentals of DSM and BPCTDSM are introduced in Chapter 2. Chapter 3 introduces the proposed high quality factor (Q) single-opamp resonator, which can be applied to BPCTDSM to achieve wide DR. Chapter 4 describes the design and implementation of a multi-mode wide DR BPCTDSM. The measurement results are presented in Chapter 5, and Chapter 6 concludes the thesis.

CHAPTER 2

FUNDAMENTALS OF BAND-PASS CONTINUOUS-TIME DELTA-SIGMA MODULATOR

2.1 DELTA-SIGMA MODULATOR

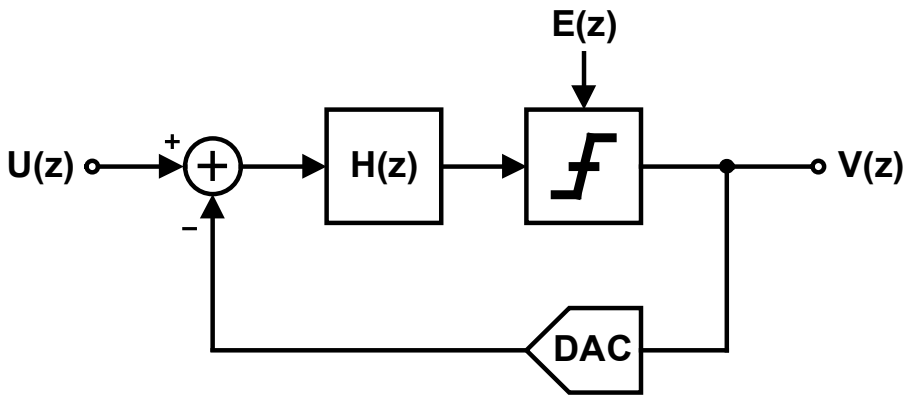

Figure 2.1.1 Block diagram of a DSM in DT domain.

Delta-sigma ADC is a well-known ADC that can easily achieve high resolution due to the noise-shaping and oversampling techniques. Figure 2.1.1 shows a block diagram of a DSM in discrete-time (DT) domain, which is a linear sampled-data system [2.1.1]. A DSM consists of loop filter $H(z)$, quantizer, and DAC. The output of the modulator can be expressed as follows:

$$V(z) = \frac{1}{1+H(z)} \cdot E(z) + \frac{H(z)}{1+H(z)} \cdot U(z). \tag{2.1.1}$$

If the loop filter has sufficient gain in the signal band, the quantization noise *E(z)* is suppressed and while the input signal remains in the signal band, as shown in Figure 2.1.2. The signal transfer function (STF) and the noise transfer function (NTF) can be derived as follow:

$$STF = \frac{H(z)}{1+H(z)} \tag{2.1.2}$$

$$NTF = \frac{1}{1+H(z)}. \tag{2.1.3}$$

The quantization error with white noise of mean-square value can be expressed as follows:

$$e_{rms}{}^2 = \frac{\Delta^2}{12} \tag{2.1.4}$$

where Δ is the step size of the quantizer. The ratio of the sampling frequency F_S over two

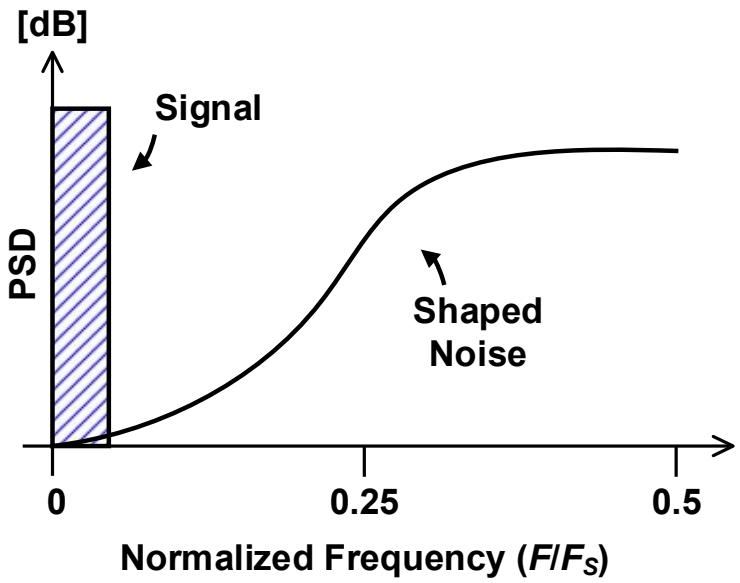

Figure 2.1.2 Power spectral density of a DSM with low-pass characteristic (LPDSM).

times of the signal bandwidth F_B is called the oversampling ratio (OSR), which is not considered in Nyquist-rate ADCs. By integrating the power spectral density of the output noise from 0 to F_B, the in-band noise can be approximated as follows:

$$q_{rms}{}^2 = \frac{\pi^2 e_{rms}{}^2}{3(OSR)^3}. \tag{2.1.5}$$

As shown in (2.1.5), the in-band noise decreases as the OSR increases. However, only about 13-bit can be achieved even for the OSR of 256. Moreover, the OSR cannot be increased too large since the sampling frequency also increases. Increasing the order of

the loop filter further increases the performance of the modulator, where a L^{th}-order loop filter results in the in-band noise as follows:

$$q_{rms}{}^2 = \frac{\pi^{2L} e_{rms}{}^2}{(2L+1)(OSR)^{2L+1}}. \tag{2.1.6}$$

Nonlinearity of the quantizer is combined with the quantization error, which is noise shaped by the NTF. On the contrary, the nonlinearity of the DAC is transferred to the input without shaping, which largely affects the performance of the modulator. Nonlinearity of the DAC can be handled in case of using a single-bit quantizer, since there are only two levels, which is inherently linear. However, the gain of a single-bit quantizer varies in a relatively wide range, which reduces the allowable input signal range. Using a multi-bit quantizer can implement more stable modulator because of the well-defined gain factor. Besides, the quantization noise is reduced by 6 dB when increasing one bit for the quantizer. Therefore, utilizing a multi-bit quantizer in higher-order loop filter is effective for achieving high performance even at low OSR. Nonlinearity of the DAC, which occurs due to the use of a multi-bit quantizer, can be alleviated by utilizing dynamic element matching (DEM) techniques. The concept of DEM is to randomize the usage of the DAC elements and results in the DAC nonlinearity to be pseudo-random noise [2.1.2].

As shown in Figure 2.1.2, a DSM is very capable when the input signal is in a narrow band at low frequencies. It is still efficient in RF communication or ultrasound systems, where the signal is in a narrow band around the center frequency F_C. By using a

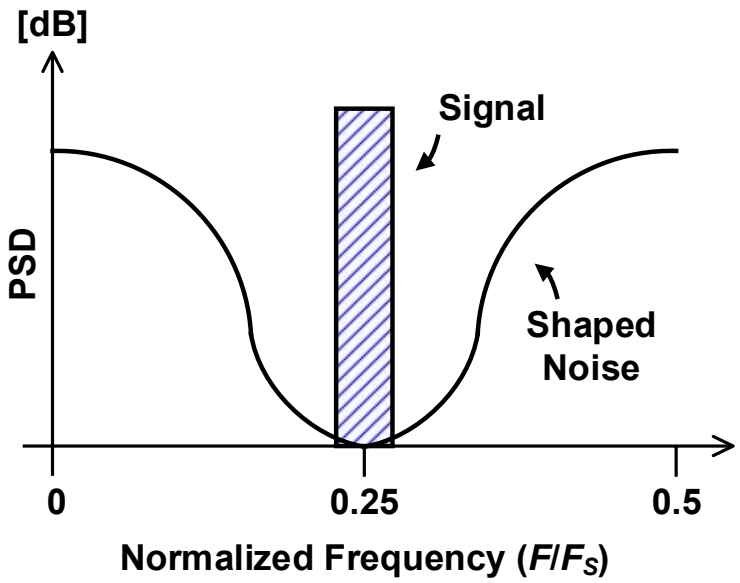

Figure 2.1.3 Power spectral density of a DSM with a band-pass characteristic (BPDSM).

mixer, the signal at a high frequency, a few MHz to tens of MHz or more, is converted to low-frequency range and then a LPDSM can be used. If the NTF has a band-pass characteristic, as shown in Figure 2.1.3, a mixer and a LPDSM can be combined in a single BPDSM [2.1.1]. The zeros are located at F_C or around F_C. The pole-zero plots of low-pass NTF and band-pass NTF are shown in Figure 2.1.4. One of the methods to obtain the NTF of a BPDSM is converting the NTF of a LPDSM by mapping z to $-z^2$, where the zeros in the LPDSM are moved from DC to $F_S/4$. The location of zeros in a BPDSM can be anywhere, from 0 to $F_S/2$. Note that F_B in a BPDSM indicates the two-

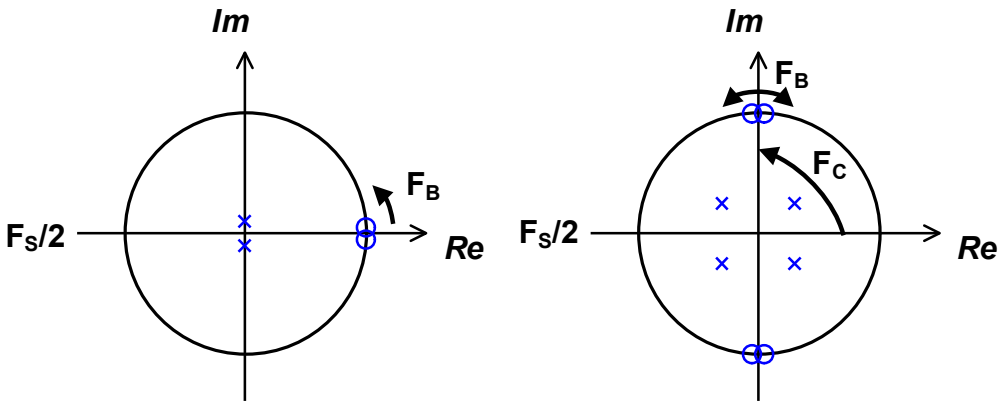

(a) (b)

Figure 2.1.4 Pole-zero plots of (a) a low-pass NTF and (b) a band-pass NTF.

sided bandwidth. The order of a BPDSM is 2*n* to implement *n* zeros in the NTF because the zeros occur in complex conjugate pairs.

The performance degradation caused by finite Q of the resonator in a BPDSM is similar to the performance degradation caused by finite DC gain of the integrator in a LPDSM, which reduces signal-to-noise and quantization ratio (SQNR) and increased nonlinearity that occurs to the harmonic tones. The SQNR degradation is significant when Q falls below F_C/F_B. Therefore, a resonator that achieves high Q is necessary to take full advantage of high OSR [2.1.3].

2.2 CONTINUOUS-TIME DELTA-SIGMA MODULATOR

The traditional discrete-time DSM (DTDSM), as shown in Figure 2.1.1, is implemented in switched-capacitor circuits. DTDSMs are generally used in audio or DC measurement applications, which have relatively low-frequency ranges and require high resolutions. Due to the switched-capacitor circuits in DTDSM, there is a limitation of increasing the sampling frequency. Recently, there is a demand for low-power, wide-bandwidth, and high-resolution ADCs, which can be satisfied by continuous-time DSM (CTDSM). The sample-and-hold operation only occurs at the quantizer in CTDSM, which is noise-shaped, and therefore suitable for wide-bandwidth systems. Figure 2.2.1 shows a block diagram of a CTDSM [2.2.1]. Compared to DTDSM, CTDSM has advantages of inherent AAF, relaxed bandwidth requirements for an opamp, and lower

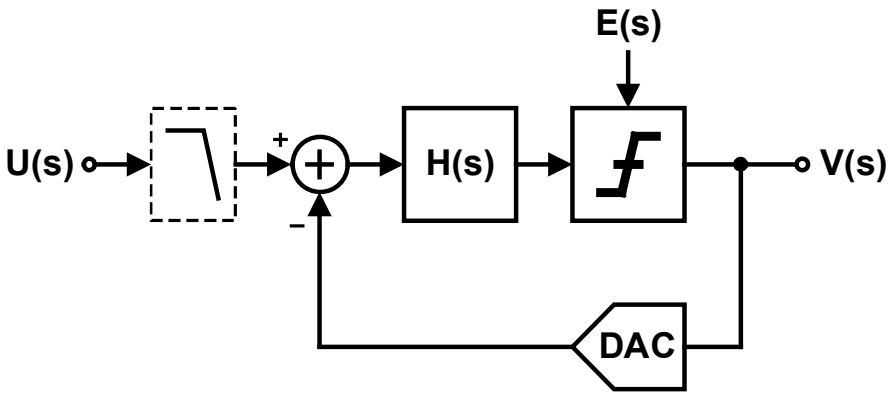

Figure 2.2.1 Block diagram of a DSM in CT domain.

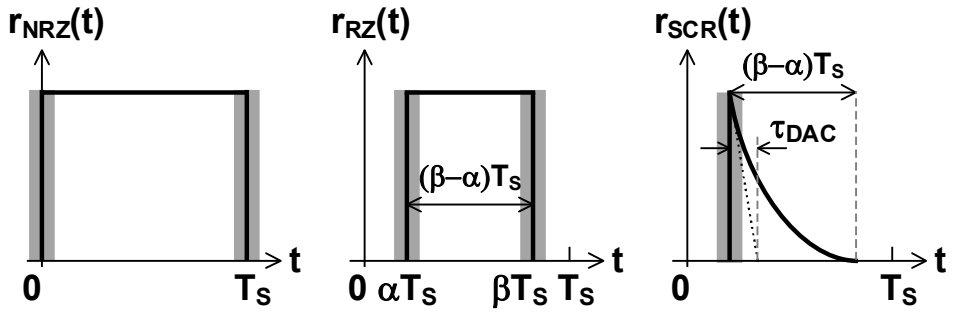

(a) (b) (c)

Figure 2.2.2 DAC waveforms of (a) NRZ DAC, (b) RZ DAC, and (c) SCR DAC.

switching noise.

There are several disadvantages of CTDSM, such as high sensitivity to process variations, high sensitivity to clock jitter, the nonlinearity of the DAC, and excess loop delay (ELD) [2.2.2]. The coefficients of DTDSM are realized as the ratios of capacitances, whereas the coefficients of CTDSM are realized as the combination of capacitances and resistances, which are sensitive to process variations. A circuit for tuning the coefficients is necessary for CTDSM [2.2.3]. The clock jitter results in sampling errors at quantizer and DAC, where the errors in the quantizer are suppressed by the NTF. However, the errors in DAC directly transferred to the input of the loop filter and severely affect the performance of the modulator. The effect of clock jitter is related to the shape of DAC waveforms. Figure 2.2.2 show various DAC waveforms; non-return-to-zero (NRZ), return-to-zero (RZ), and switched-capacitor resistor (SCR) DACs. Since the amplitude of RZ DAC is twice that of NRZ DAC, the sensitivity to clock jitter in RZ DAC is larger

than NRZ DAC. The effect of clock jitter decreases when using a multi-bit quantizer, which reduces the amplitude of 1-LSB. Adapting shaped waveform DACs, such as SCR DAC, can be a solution to lower the effect of clock jitter. As shown in Figure 2.2.2(c), the clock jitter affects only one edge in SCR DAC, while both edges are affected in NRZ and RZ DACs. Although an SCR DAC is good for the sensitivity to clock jitter, the scaling coefficients are larger compared to rectangular shaped waveform DACs, which result in the large feedback signal. Moreover, the discharging operation in SCR DAC fluctuates the virtual ground node. Therefore, it would be a better choice to use NRZ DAC with multi-bit quantizer. Nonlinearity of the multi-bit DAC can be addressed by DEM techniques [2.1.2]. ELD is the delay that arises from the quantizer to feedback DAC, which is unavoidable in CTDSM. The delayed signal to DAC generates sampling error and degrades both the performance and stability of the modulator. It is necessary to include ELD compensation in CTDSM, except when the ELD coefficient is small, and OSR is high [2.2.4]. NTF in DT domain by utilizing the Delta-Sigma Toolbox or other open sources. Next, the NTF in DT domain is converted to continuous-time (CT) domain through transformation procedure.

To design a CTDSM efficiently, we first obtain the desired NTF in DT domain and then converts to CT domain by using the impulse-invariant transformation. Figure 2.2.3 shows the concept of impulse-invariant transformation [2.2.1]. The outputs of DTDSM and CTDSM are identical at the moment of sampling when the inputs of the DTDSM and CTDSM quantizers are the same. According to the shape of DAC waveform, the impulse responses of the open-loop can be derived as follow:

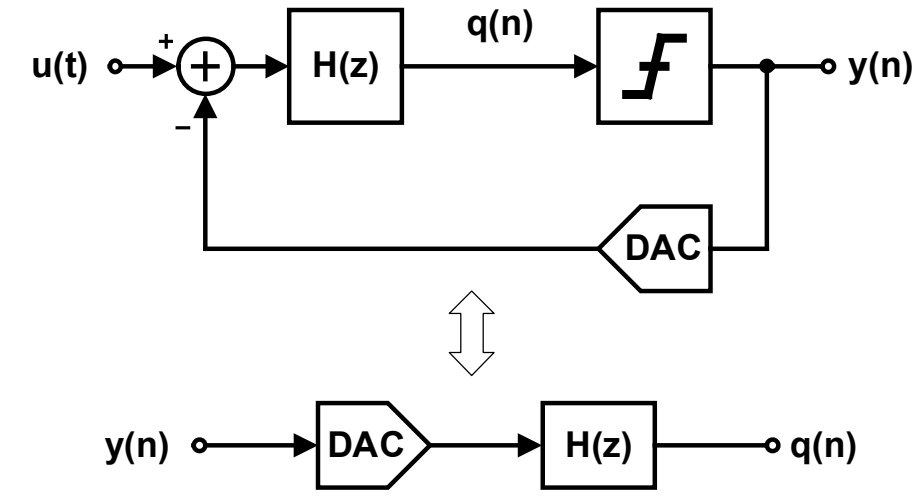

(a)

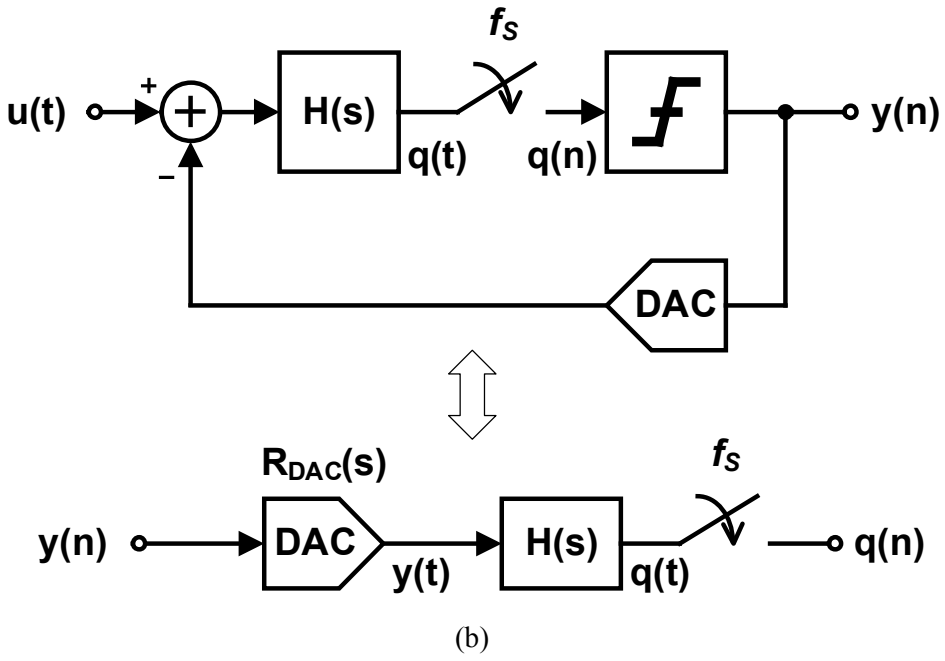

(b)

Figure 2.2.3 Block diagram of modulators and open-loop representation in (a) DTDSM and (b) CTDSM.

Table 2.2.1 Impulse response and Laplace transform of various DAC waveforms

DAC	Impulse Response $r_{DAC}(t)$	Laplace Transform $R_{DAC}(s)$
NRZ	$1, \quad 0 \le t \le T_S$ $0, \quad otherwise$	$\frac{1-e^{-sT_S}}{s}$
RZ	$1, \quad \alpha T_S \le t \le \beta T_S$ $0, \quad otherwise$	$\frac{e^{-s\alpha T_S}\left(1-e^{-s(\beta-\alpha)T_S}\right)}{s}$
SCR	$e^{-(t-\alpha T_S)/\tau_{DAC}}, \quad \alpha T_S \le t \le \beta T_S$ $0, \quad otherwise$	$\frac{e^{-s\alpha T_S}\left(1-e^{-(\beta-\alpha)T_S(s+1/\tau_{DAC})}\right)}{s+\frac{1}{\tau_{DAC}}}$

$$q(n) = q(t)\big|_{t=nT_S} \tag{2.2.1}$$

$$Z^{-1}\{H(z)\} = L^{-1}\{R_{DAC}(s)H(s)\}\big|_{t=nT_S} \tag{2.2.2}$$

$$h(n) = \left[r_{DAC}(t) * h(t)\right]\big|_{t=nT_S} = \int_{-\infty}^{\infty} r_{DAC}(\tau)h(t-\tau)d\tau\big|_{t=nT_S} \tag{2.2.3}$$

where $r_{DAC}(t)$ is the impulse response and $R_{DAC}(s)$ is the Laplace transform of the specific DAC. Table 2.2.1 shows impulse responses and Laplace transforms of NRZ DAC, RZ DAC, and SCR DAC. For example, a second-order loop filter, $1/(z\text{-}1)^2$, with RZ DAC can

be converted to CT domain through following steps.

$$h(n) = \left[r_{DAC}(t) * h(t) \right]\Big|_{t=nT_S} = \int_{\alpha T_S}^{\beta T_S} h(t-\tau) d\tau \Big|_{t=nT_S} \tag{2.2.4}$$

$$h(t-\tau) = L^{-1}\left\{ \frac{\omega_1 s + \omega_0}{s^2} \right\} = \omega_1 u(t-\tau) + \omega_0 (t-\tau) u(t-\tau) \tag{2.2.5}$$

$$\begin{aligned} h(n) &= \int_{\alpha T_S}^{\beta T_S} \omega_1 u(t-\tau) + \omega_0 (t-\tau) u(t-\tau) \Big|_{t=nT_S} \\ &= \left[\omega_1 \tau + \omega_0 \left(nT_S \tau - \frac{\tau^2}{2} \right) \right]_{\alpha T_S}^{\beta T_S} \\ &= \omega_1 (\beta - \alpha) T_S + \omega_0 \left(\alpha^2 - \beta^2 + 2(\beta - \alpha) \right) \frac{{T_S}^2}{2} \\ &\quad + \omega_0 (n-1)(\beta - \alpha) {T_S}^2 \end{aligned} \tag{2.2.6}$$

$$\begin{aligned} h(n) &= Z^{-1}\{ H(z) \} = Z^{-1}\left\{ \frac{1}{(z-1)^2} \right\} \\ &= (n-1) u(n-1) \end{aligned} \tag{2.2.7}$$

Since (2.2.6) and (2.2.7) are the impulse responses of the loop filter in CTDSM and DTDSM, respectively, the two equations should be equal. Therefore, the unknown variables ω_1 and ω_0 can be expressed as follows:

$$\omega_1 = \frac{{f_S}^2}{\beta - \alpha}, \quad \omega_0 = \frac{(\beta - \alpha - 2) f_S}{2(\beta - \alpha)}. \tag{2.2.8}$$

Table 2.2.2 Equivalent low-pass loop filter in DT domain and CT domain

Z Domain	**S Domain**	
$\frac{1}{(z-1)}$	$\frac{\omega_0}{s}$	$\omega_0 = \frac{f_S}{\beta-\alpha}$
$\frac{1}{(z-1)^2}$	$\frac{\omega_1 s+\omega_0}{s^2}$	$\omega_0 = \frac{{f_S}^2}{\beta-\alpha},\ \ \omega_1 = \frac{f_S(\alpha+\beta-2)}{2(\beta-\alpha)}$
$\frac{1}{(z-1)^3}$	$\frac{\omega_2 s^2+\omega_1 s+\omega_0}{s^3}$	$\omega_0 = \frac{{f_S}^3}{\beta-\alpha},\ \ \omega_1 = \frac{{f_S}^2(\alpha+\beta-3)}{2(\beta-\alpha)},$ $\omega_2 = \frac{f_S\left[\beta(\beta-9)+\alpha(\alpha-9)+4\alpha\beta+12\right]}{12(\beta-\alpha)}$

Loop filters in the CT domain can be obtained by using the above method even when another order of loop filter and another type of DAC are used. Table 2.2.2 shows the equivalent low-pass loop filter in DT domain and CT domain when the rectangular shaped DAC, as shown in Figure 2.2.2(b), is used. If α is 0 and β is 1, Table 2.2.2 can be applied for converting the loop filter from DT domain to CT domain when NRZ DAC is used.

2.3 BAND-PASS CONTINUOUS-TIME DELTA-SIGMA MODULATOR

The NTF of BPCTDSM is obtained as the same method in CTDSM. Choose an appropriate band-pass NTF in DT domain and then converts to CT domain through impulse-invariant transformation. The difference between low-pass and band-pass is the location of poles in the loop filters. The loop filter of BPDTDSM, which contains multiple poles, can be expressed with a combination of rational functions by utilizing partial fraction. For example, a rational function in DT domain, which has a pole at p_Z, can be converted to CT domain through following steps. For simplicity, the equations are derived assuming that a NRZ DAC is used in the modulator.

$$H(z) = \sum_{k=1}^{N} \frac{a_Z}{z - p_Z} \tag{2.3.1}$$

$$H(s) = \sum_{k=1}^{N} \frac{a_S}{s - p_S} \tag{2.3.2}$$

$$\begin{aligned} h(t) &= \int_{-\infty}^{\infty} \left(u(t) - u(t-\tau)\right) \sum_{k=1}^{N} a_S e^{p_S(t-\tau)} \cdot u(t-\tau) d\tau \Big|_{t=kT_S} \\ &= \sum_{k=1}^{N} a_S \int_0^{T_S} e^{p_S(t-\tau)} u(t-\tau) d\tau \Big|_{t=kT_S} \\ &= \sum_{k=1}^{N} a_S \int_0^{T_S} e^{p_S(kT_S-\tau)} d\tau \\ &= \sum_{k=1}^{N} -\frac{a_S}{p_s} \cdot e^{p_S kT_S} \left(e^{-p_S T_S} - 1\right) \end{aligned} \tag{2.3.3}$$

Table 2.3.1 Equivalent band-pass loop filter in DT domain and CT domain

Z Domain	**S Domain**		
$\frac{a_Z}{(z-p_Z)}$	$\frac{a_S}{(s-p_S)}$	$a_S = \frac{-p_S a_Z}{1-e^{p_S T_S}}$	$p_S = \frac{\ln p_Z}{T_S}$
$\frac{a_Z}{(z-p_Z)^2}$	$\frac{a_S}{(s-p_S)^2}$	$a_S = \frac{a_Z}{\left(1-e^{p_S T_S}\right)^2}\left(\frac{1-e^{-p_S T_S}-s_0 T_S}{T_S}s + {s_0}^2\right)$	
$\frac{a_Z}{(z-p_Z)^3}$	$\frac{a_S}{(s-p_S)^3}$	$a_S = \frac{-a_Z}{\left(1-e^{p_S T_S}\right)^3}\left(k_2 s^2 + k_1 s + k_0\right)$ $k_2 = \frac{2p_S T_S - 3 + 4e^{-p_S T_S} - e^{-2p_S T_S}}{2T_S}$ $k_1 = \frac{-4{T_S}^2 {p_S}^2 + \left(3 - 4e^{-p_S T_S} + e^{-2p_S T_S}\right) p_S T_S + 2\left(1-e^{-p_S T_S}\right)^2}{2{T_S}^2}$ $k_0 = {p_S}^3$	

$$
\begin{aligned}
H(z) &= \sum_{-\infty}^{\infty} h(n) z^{-n} \\
&= \sum_{n=1}^{\infty}\left(\sum_{k=1}^{N} -\frac{a_S}{p_s}\cdot e^{p_s k T_S}\left(e^{-p_s T_S}-1\right)\right) z^{-n} \\
&= \sum_{k=1}^{N} -\frac{a_S}{p_s}\left(e^{-p_s T_S}-1\right)\sum_{n=1}^{\infty}\left(e^{p_s k T_S} z^{-1}\right)^n \\
&= \sum_{k=1}^{N} -\frac{a_S}{p_s}\left(e^{-p_s T_S}-1\right)\left(\frac{\left(1-e^{p_s T_S}\right) z^{-1}}{1-e^{p_s T_S} z^{-1}}\right)
\end{aligned}
\tag{2.3.4}
$$

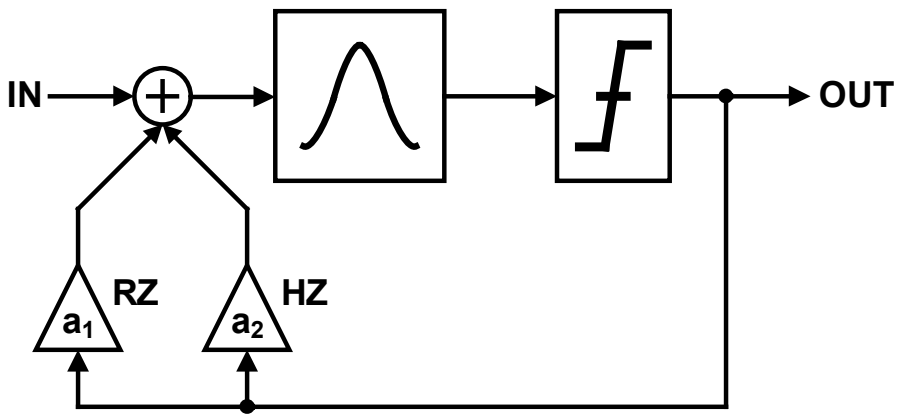

Figure 2.3.1 Block diagram of a BPDSM with a passive resonator.

Since (2.3.1) and (2.3.4) should be identical, where the coefficients a_Z and p_Z are the known variables, the unknown coefficients a_S and p_S can be expressed as follows:

$$a_S = \frac{-a_Z p_S}{1-e^{p_S T_S}}, \quad p_S = \frac{\ln p_Z}{T_S}. \tag{2.3.5}$$

Table 2.3.1 shows the equivalent rational functions in DT domain, which are presented through partial fraction, and CT domain when a NRZ DAC is used.

The most critical block of implementing a BPDSM is a resonator. The resonator can be implemented as a passive or active topology, as shown in Figure 2.3.1 and Figure 2.3.2, respectively [2.1.3]. A passive resonator utilizes inductor and requires two DACs in each resonator. The advantages of a passive resonator are low-noise, low-power, and high Q.

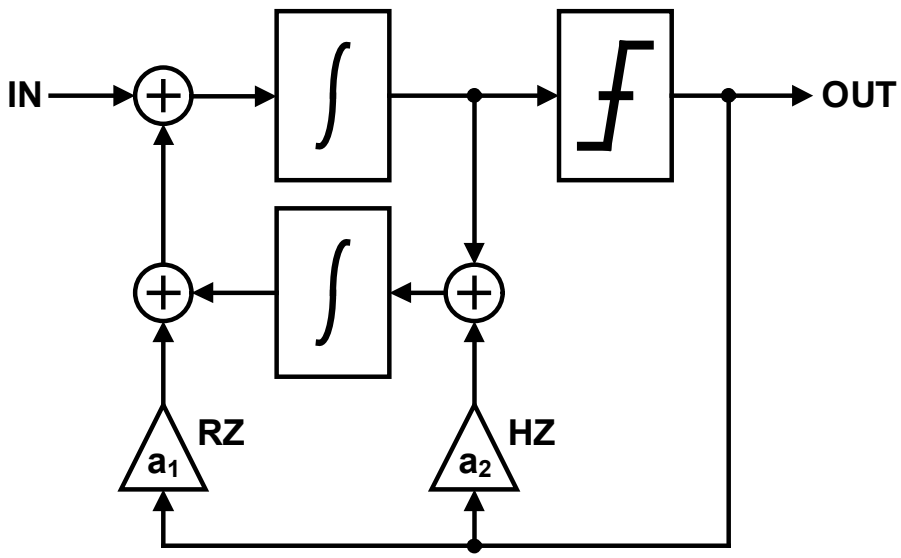

Figure 2.3.2 Block diagram of a BPDSM with an active resonator.

Due to the usage of inductors and multiple DACs, both silicon area and power consumption increases. An active resonator utilizes opamps instead of inductors, which contributes to small silicon area. Although an active resonator is area efficient, the power consumption is still significant because of using two opamps in each resonator.

2.4 PERFORMANCE METRICS

Performance metrics that commonly used in ADCs are described below and are shown in Figure 2.4.1 for clarity.

- Signal-to-noise ratio (SNR) is the ratio of the signal power to the noise power, which is measured for a certain input frequency and amplitude.
- Signal-to-noise and distortion ratio (SNDR) is the ratio of the signal power to the noise and distortion power, which is measured for a certain input frequency and amplitude.
- Dynamic range (DR) is the ratio between the largest and smallest input signal, where the smallest detectable input signal is determined by the noise floor.
- Total harmonic distortion (THD) is the ratio of the signal power to the sum of the signal power of all harmonic frequencies above the noise floor.
- Spurious-free dynamic range (SFDR) is the ratio of the signal power to the power of the strongest spectral tone.
- Effective number of bits (ENOB) specifies the resolution of an ideal ADC circuit that would have the same resolution as the circuit under consideration. An often used definition for ENOB can be expressed as follows:

$$ENOB = \frac{SNDR_{PEAK} - 1.76}{6.02} \tag{2.4.1}$$

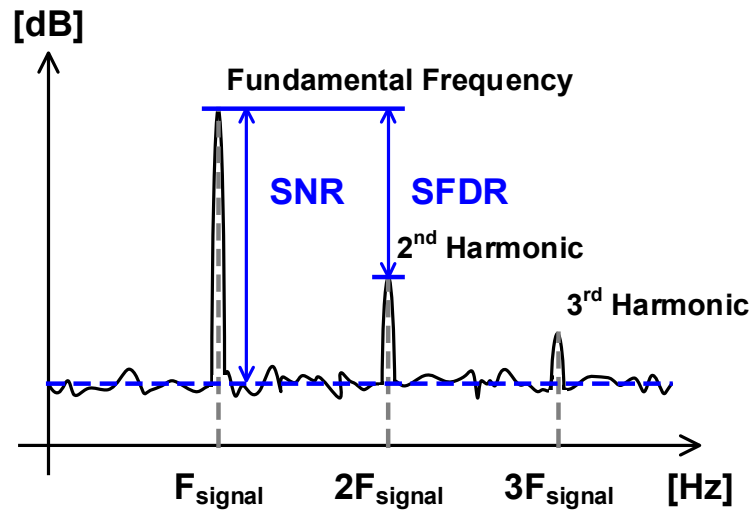

(a)

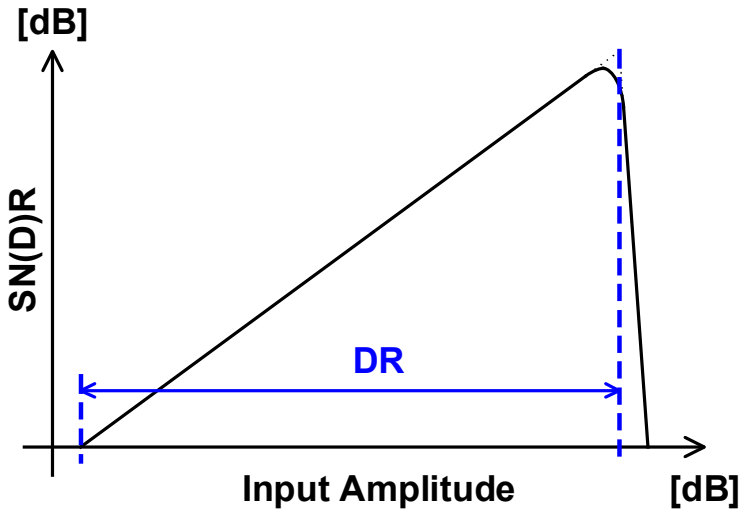

(b)

Figure 2.4.1 (a) Power spectral density of an ADC output and (b) SN(D)R against input amplitude.

CHAPTER 3

WIDE DYNAMIC RANGE BAND-PASS CONTINUOUS-TIME DELTA-SIGMA MODULATOR WITH HIGH QUALITY FACTOR SINGLE-OPAMP RESONATOR

As mentioned before, the key factor that decides the performance in BPDSM is Q of the resonator, especially when F_C/F_B is large [2.1.3]. To achieve wide DR in CW Doppler receiver, a high Q resonator is necessary. Single-opamp resonators [3.1.1]–[3.1.5], which are commonly used to decrease the power consumption by reducing the number of opamps used compared to the conventional active resonator, are largely affected by the finite GBW of opamps and therefore occur degradation of Q [3.1.6], [3.1.7]. Using a multi-stage opamp is appropriate to achieve high GBW [3.1.2], but the requirements for the multi-stage opamp become more severe as F_C/F_B increases, which results in more power consumption. The coefficients of the loop filter can be compensated by considering the finite GBW as an effect of gain error and additional loop delay, or using an additional feedback path can also compensate the loop delay caused by the finite GBW [3.1.8]. Compensating the coefficients can be applied even when F_C/F_B increases,

however, the compensated coefficients are not guaranteed to be implemented using unit resistance and unit capacitance, which is important to reduce the mismatch between the passive components. The other compensation method, which uses an additional feedback path, requires an additional feedback DAC. Therefore, we propose a high Q single-opamp resonator, which compensates the degradation of Q by using positive feedback resistor without burdening to the design of an opamp and implementing the passive components in the single-opamp resonator with unit resistance and unit capacitance. From now on, analysis for the effect of finite GBW to the prior single-opamp resonators and the proposed single-opamp resonator will be discussed. The simulation results that show the effectiveness of the proposed high Q single-opamp resonator will be shown.

3.1 PRIOR SINGLE-OPAMP RESONATORS

Previous works have introduced several single-opamp resonators. Among the prior works, two single-opamp resonators, which have simple structures, are chosen for further analysis. The transfer functions of the single-opamp resonators in [3.1.1] (REF_1) and [3.1.2] (REF_2), which are shown in Figure 3.1.1(a) and Figure 3.1.1(b), can be expressed as follow:

$$H_{REF1} = -\frac{(C_1+C_2)}{C_1C_2}\cdot\frac{1}{R_{in}}\cdot\frac{\dfrac{1}{(C_1+C_2)}\cdot\left(\dfrac{1}{R_2}+\dfrac{1}{R_3}\right)+s}{\dfrac{1}{C_1C_2R_1R_2}\cdot\left(1+\dfrac{R_2}{R_3}\right)+s\left(\dfrac{1}{C_2R_1}-\dfrac{1}{C_2R_3}+\dfrac{1}{C_1R_1}\right)+s^2} \quad (3.1.1)$$

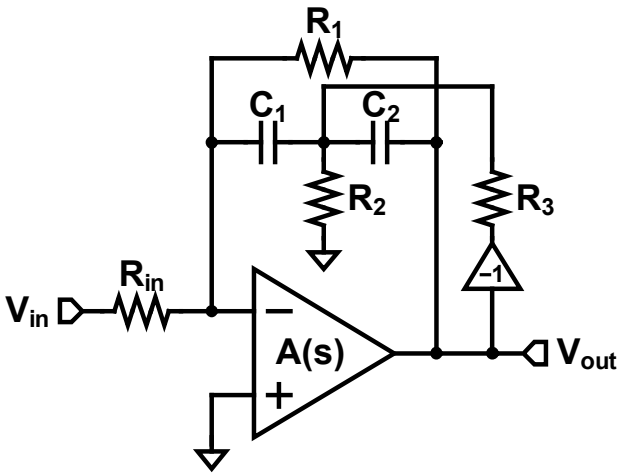

(a)

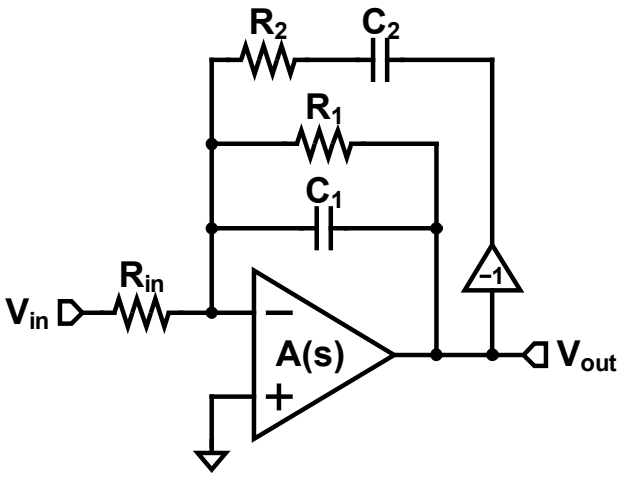

(b)

Figure 3.1.1 Block diagram of single-opamp resonators in (a) REF_1 and (b) REF_2.

$$H_{REF2} = -\frac{1}{C_1 R_{in}} \cdot \frac{\frac{1}{C_2 R_2} + s}{\frac{1}{C_1 C_2 R_1 R_2} + s\left(\frac{1}{C_1 R_1} - \frac{1}{C_1 R_2} + \frac{1}{C_2 R_2}\right) + s^2}. \quad (3.1.2)$$

Since the transfer function of an ideal resonator is defined by

$$H_{IDEAL} = \frac{\omega_C s}{\omega_C{}^2 + s^2} \quad (3.1.3)$$

where $\omega_C = 2\pi F_C$. The conditions to make *REF1* and *REF2* similar to the ideal resonator in (3.1.3) are to make the first order terms of the denominators in (3.1.1) and (3.1.2) zero, which can be expressed as follow:

$$\left(C_1 + C_2\right) R_3 = C_1 R_1 \quad (3.1.4)$$

$$C_1 R_1 + C_2 R_2 = C_2 R_1 . \quad (3.1.5)$$

where (3.1.4) for *REF1* and (3.1.5) for *REF2*. If the conditions (3.1.4) and (3.1.5) are not satisfied, Q of the single-opamp resonator decreases and therefore affects the performance of the BPCTDSM. Thus, the capacitors and resistors should be determined by the combination of the unit capacitor and unit resistor to minimize the effect of process variations in passive components.

However, there is another factor that causes the degradation of Q, which is nonlinearity of an opamp. The transfer functions (3.1.1) and (3.1.2) are derived by

assuming that opamps of the single-opamp resonators are ideal. For simplicity, let us assume that an opamp has a finite gain and infinite bandwidth:

$$A(s) = A_{DC}\,. \tag{3.1.6}$$

By substituting (3.1.6) to (3.1.1) and (3.1.2), we can obtain the transfer functions of single-opamp resonators that the nonlinearity of an opamp is applied:

$$H_{REF1}' = -\frac{A_{DC}}{\left(1+A_{DC}\right)}\cdot\frac{\left(C_1+C_2\right)}{C_1C_2}\cdot\frac{1}{R_{in}} \cdot\frac{\dfrac{1}{\left(C_1+C_2\right)}\cdot\left(\dfrac{1}{R_2}+\dfrac{1}{R_3}\right)+s}{\dfrac{Z_1\left(1+\dfrac{R_2}{R_3}\right)}{C_1C_2R_1R_2}+s\left(\dfrac{1}{C_2R_1}-\dfrac{\left(-1+A_{DC}\right)}{\left(1+A_{DC}\right)C_2R_3}+\dfrac{Z_1}{C_1R_1}+\dfrac{\left(1+\dfrac{R_2}{R_{in}}\right)}{\left(1+A_{DC}\right)C_2R_2}\right)+s^2} \tag{3.1.7}$$

$$\left(where\quad Z_1 = 1+\frac{R_1}{\left(1+A_{DC}\right)R_{in}}\right)$$

$$H_{REF2}' = -\frac{A_{DC}}{\left(1+A_{DC}\right)}\cdot\frac{1}{C_1R_{in}} \cdot\frac{\dfrac{1}{C_2R_2}+s}{\dfrac{\left(1+\dfrac{R_1}{\left(1+A_{DC}\right)R_{in}}\right)}{C_1C_2R_1R_2}+s\left(\dfrac{1}{C_2R_2}-\dfrac{\left(-1+A_{DC}\right)}{\left(1+A_{DC}\right)C_1R_2}+\dfrac{\left(1+\dfrac{R_1}{\left(1+A_{DC}\right)R_{in}}\right)}{C_1R_1}\right)+s^2}\,. \tag{3.1.8}$$

Because of the finite gain of an opamp, the degree one of the denominators in (3.1.7) and (3.1.8) are not eliminated when maintaining the conditions (3.1.4) and (3.1.5), respectively. As the finite gain of an opamp gets smaller, the effect of the finite gain of an opamp to Q of the resonator becomes larger. Figure 3.1.2(a) shows the bode plot of H_{REF2}' against the finite gain of an opamp.

There might be a possibility of achieving Q over 100 in (3.1.7) and (3.1.8) when A_{DC} is 52 dB while maintaining (3.1.4) and (3.1.5). By using MATHEMATICA, it is confirmed that (3.1.7) and (3.1.8) have no solutions that satisfy the target Q of 100 on conditions of (3.1.4) and (3.1.5), respectively. If the equations are solved without considering (3.1.4) and (3.1.5), still there is no solution for REF_1, while REF_2 has a solution if R_2 can be finely tuned. Figure 3.1.2(b) shows the transfer function of REF_2 against the variation of R_2 in 1% intervals. Although it can achieve high Q in REF_2 by adjusting R_2 with high resolution, the feasibility of implementing R_2 is almost impossible. Therefore, we propose an advanced single-opamp resonator that achieves high Q of over 100, with considering the nonlinearity of an opamp.

Additional analysis of considering an opamp as a single pole system, finite gain of A_{DC} and finite bandwidth of ω_p, as follows:

$$A(s) = \frac{A_{DC}}{1 + \frac{s}{\omega_p}}. \tag{3.1.9}$$

When substituting (3.1.9) to (3.1.2),

$$H_{REF2}'' = -\frac{N_0 + N_1 s}{D_0 + D_1 s + D_2 s^2 + D_3 s^3} \tag{3.1.10}$$

$$N_0 = -A_{DC}\omega_p R_1$$

$$N_1 = -A_{DC}\omega_p C_1 R_1 R_2$$

$$D_0 = \left(R_1 + A_{DC} R_{in}\right)\omega_p$$

$$D_1 = R_{in} + R_1 + C_2 R_1 R_2 \omega_p$$

$$D_2 = C_2 R_1 R_{in}\left(1 + A_{DC}\omega_p C_1 R_2\right)$$

where $(1+A_{DC})$ is assumed to A_{DC} and the condition (3.1.5) is maintained. Figure 3.1.3(a) and Figure 3.1.3(b) show the bode plots of H_{REF2}'' against the finite DC gain of an opamp when the bandwidth is fixed to 20 MHz, and against the finite bandwidth of an opamp when the DC gain is fixed to 60 dB. As shown in Figure 3.1.3(a) and Figure 3.1.3(b), the effect of decreasing the DC gain and the bandwidth results in the degradation of Q. The variations in the center frequency can be adjusted by tuning the values of capacitors.

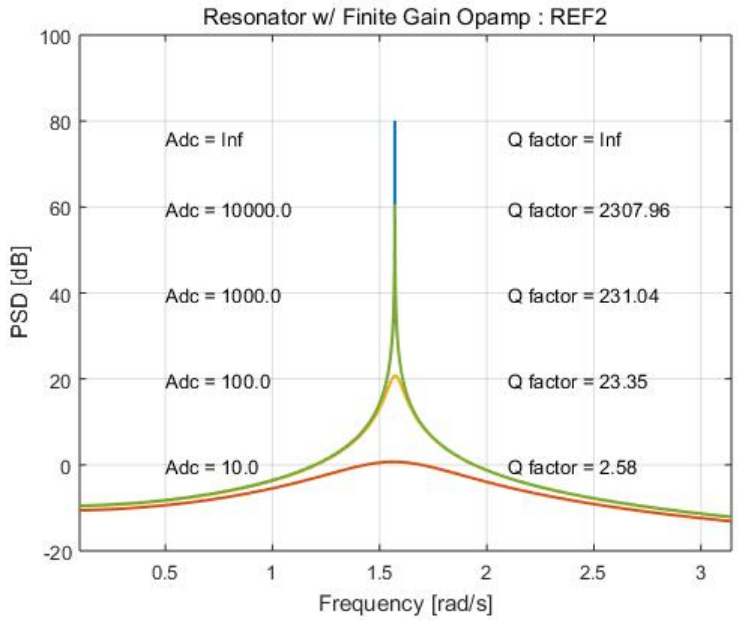

(a)

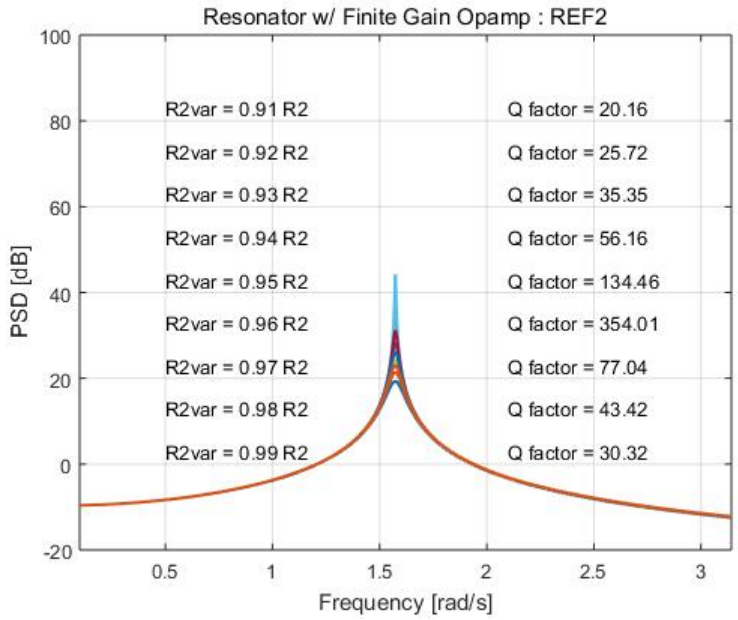

(b)

Figure 3.1.2 Bode plots of H_{REF2}' against the finite gain of an opamp (a) on condition (3.1.4) and (b) adjusting R_2 in 1% intervals.

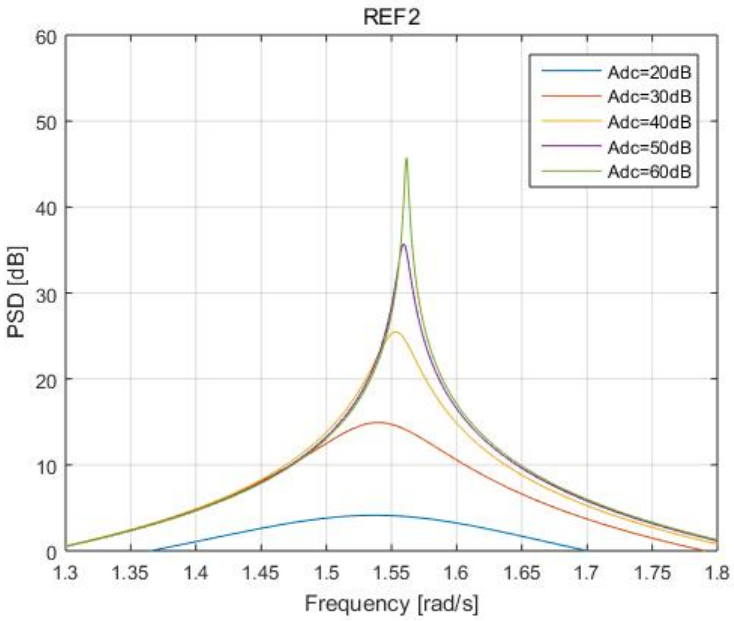

(a)

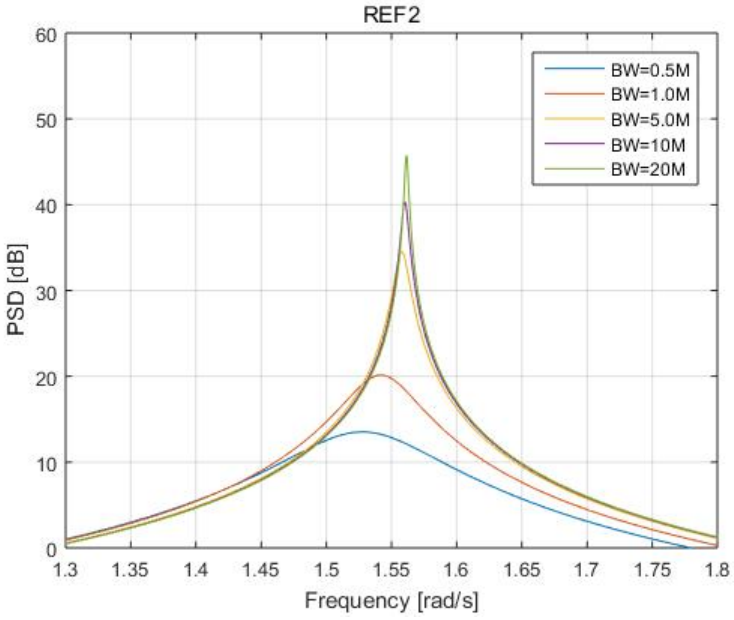

(b)

Figure 3.1.3 Bode plots of H_{REF2}' (a) against the finite DC gain at bandwidth of 20 MHz and (b) against the bandwidth at DC gain of 60 dB.

3.2 HIGH QUALITY FACTOR SINGLE-OPAMP RESONATOR

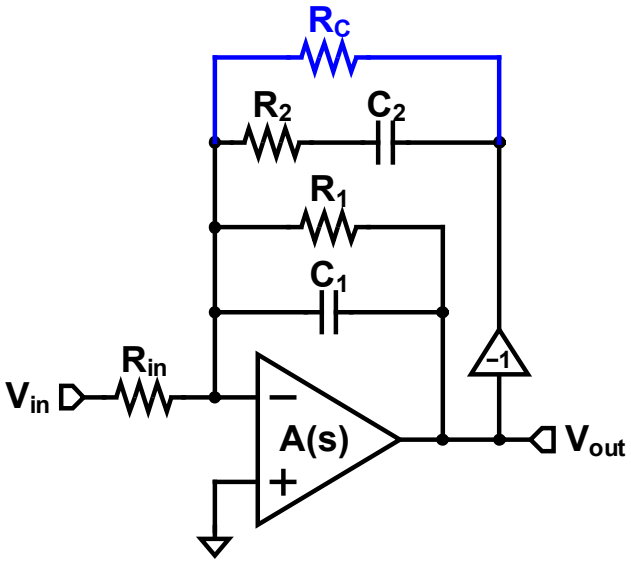

Figure 3.2.1 Block diagram of the proposed high Q single-opamp resonator.

Figure 3.2.1 shows the block diagram of the proposed high Q single-opamp resonator, which includes positive feedback resistor path. The transfer function of the proposed resonator can be expressed as follows:

$$H_{PROP} = -\frac{1}{C_1 R_{in}} \cdot \frac{\frac{1}{C_2 R_2} + s}{\frac{1}{C_1 C_2 R_1 R_2} \cdot \left(1 - \frac{R_1}{R_C}\right) + s\left(\frac{1}{C_2 R_2} - \frac{1}{C_1 R_2} + \frac{1}{C_1 R_1} \cdot \left(1 - \frac{R_1}{R_C}\right)\right) + s^2} \tag{3.2.1}$$

$$H_{PROP}' = -\frac{A_{DC}}{(1+A_{DC})} \cdot \frac{1}{C_1 R_{in}} \cdot \frac{\frac{1}{C_2 R_2} + s}{\frac{1}{C_1 C_2 R_1 R_2} \cdot (1+Z_C) + s\left(\frac{1}{C_2 R_2} - \frac{(-1+A_{DC})}{(1+A_{DC}) C_1 R_2} + \frac{1}{C_1 R_1} \cdot (1+Z_C)\right) + s^2} \tag{3.2.2}$$

$$\left(where \quad Z_C = \frac{R_1}{(1+A_{DC}) R_{in}} - \frac{(-1+A_{DC}) R_1}{(1+A_{DC}) R_C} \right)$$

where (3.2.1) is derived assuming an ideal opamp, and (3.2.2) is derived assuming an opamp with finite gain as in (3.1.6). Although the degree one of the denominators in (3.2.1) is not zero in the condition (3.1.4), Q of (3.2.2) can achieve more than 100 by adjusting R_C at unit resistance intervals while maintaining the condition (3.1.4). Figure 3.2.2 shows H_{PROP}' against the finite gain of an opamp, which results in the existence of R_C compensates the degradation of Q due to the finite gain of an opamp.

We just considered the finite gain of an opamp for the ease of presenting the effect of R_C to Q. Same results will be shown when an opamp achieves the finite bandwidth with constant DC gain. The analysis of considering both finite gain and finite bandwidth of an opamp is shown below.

$$H_{PROP}'' = -\frac{N_0 + N_1 s}{D_0 + D_1 s + D_2 s^2} \tag{3.2.3}$$

$$N_0 = -A_{DC} \omega_p R_1 R_C$$

$$N_1 = -A_{DC} \omega_p C_2 R_1 R_2 R_C$$

$$D_0 = \left(R_1 R_C + A_{DC} R_{in}\left(-R_1 + R_C\right)\right)\omega_p$$

$$D_1 = R_C\left(R_1 + R_{in}\right) + R_1 R_{in} + R_1 R_C\left(C_2 R_2 - C_1 R_{in} A_{DC}\right)\omega_p$$

$$D_2 = C_2 R_1 R_2\left(R_{in} + R_C + C_1 R_{in} R_C A_{DC}\omega_p\right)$$

where $(1+A_{DC})$ is assumed to A_{DC} and the condition (3.1.5) is maintained. To make high Q resonator, D_1 in (3.1.10) and (3.2.3) should be small or even zero. We derived (3.1.10) and (3.2.3) from the same condition of (3.1.4), where (3.1.10) cannot be removed at all while (3.2.3) can be removed to some extent by adjusting R_C.

As shown in Figure 3.2.3, as the bandwidth of an opamp decreases, the gain of at the center frequency also decreases, which results in the degradation of Q in the resonator. From the above analysis, the effect of finite GBW of an opamp to Q of the resonator can be compensated by utilizing the proposed single-opamp resonator topology without consuming additional power. Although an additional resistor is used compared to the single-opamp resonator that shown in Figure 3.1.1(b), it occupies a very small part of the total silicon area. The proposed high Q single-opamp resonator would be more effective when the center frequency of the resonator gets higher.

To evaluate the effectiveness of the proposed high Q single-opamp resonator, an ideal 4th-order BPCTDSM with proposed resonators are simulated. Verilog-A is used to model an ideal opamp, and the passive components are used within "analogLib," which is a built-in library in Cadence. The following simulation results are from the ideal 4th-order BPCTDSM in gingival-mode including the noise. Figure 3.2.4(a) shows the output power

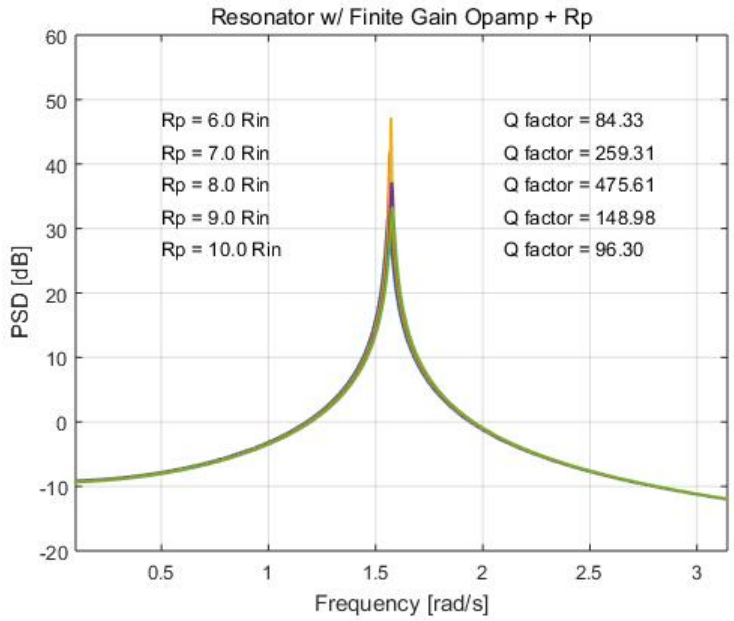

Figure 3.2.2 Bode plots of H_{PROP}' against the finite gain of an opamp.

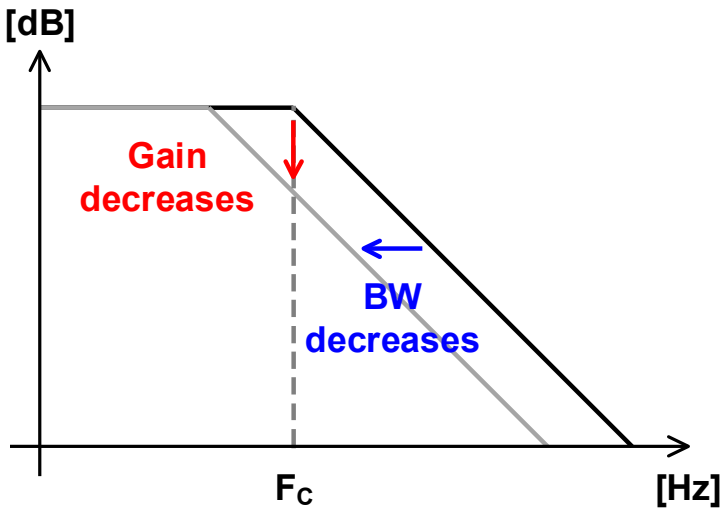

Figure 3.2.3 Bode plots of an opamp with finite GBW.

spectral density of the ideal BPCTDSM using prior single-opamp resonators. The DC gain and bandwidth of an opamp are set to 60 dB and 20 MHz, respectively. Since the gain of an opamp at 20 MHz is 60 dB, which is large enough, the modulator is possible to detect a tiny input signal of –90 dB. When the bandwidth of an opamp is decreased to 2 MHz, maintaining the DC gain, input signal of –90 dB. As shown in Figure 3.2.4(b), the SNDR obtained when the bandwidth of an opamp is 20 MHz is achieved at an input signal of –75 dB instead of –90 dB due to the decreased gain of an opamp at the center frequency. However, the degradation of the performance can be recovered by using the proposed single-opamp resonator, which compensates for the degradation of Q with an additional positive feedback resistor. Figure 3.2.5(a) shows the output power spectral density of the ideal 4^{th}-order BPCTDSM using proposed single-opamp resonators. The DC gain and bandwidth of an opamp are set to 60 dB and 2 MHz, respectively. Despite the decreased bandwidth that results in the decreased gain at the center freuqency, the modulator is capable of detecting an input signal of –90 dB. Similar SNDR is achieved at the bandwidth of an opamp of 1 MHz, as shown in Figure 3.2.5(b). As a result, when using the proposed high Q single-opamp resonator, small inputs can be detected despite the use of an opamp with relaxed specifications, and therefore the power consumption can be decreased.

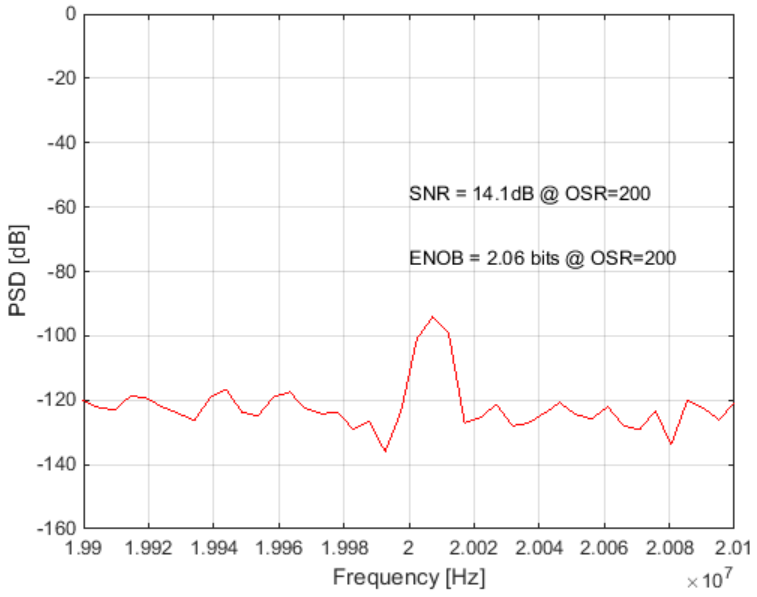

(a)

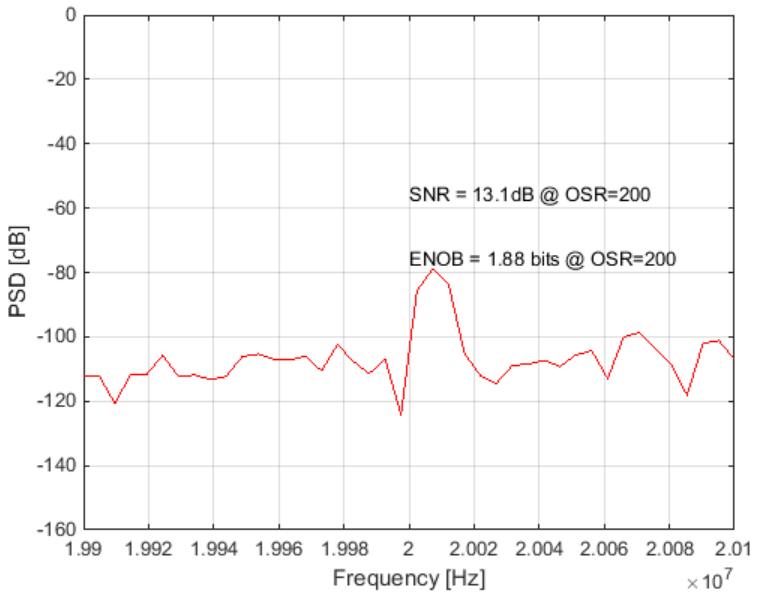

(b)

Figure 3.2.4 Power spectral density of an ideal BPCTDSM with prior single-opamp resonator at (a) –90 dBFS input, BW_{opamp} = 20 MHz and (b) –75 dBFS input, BW_{opamp} = 2 MHz.

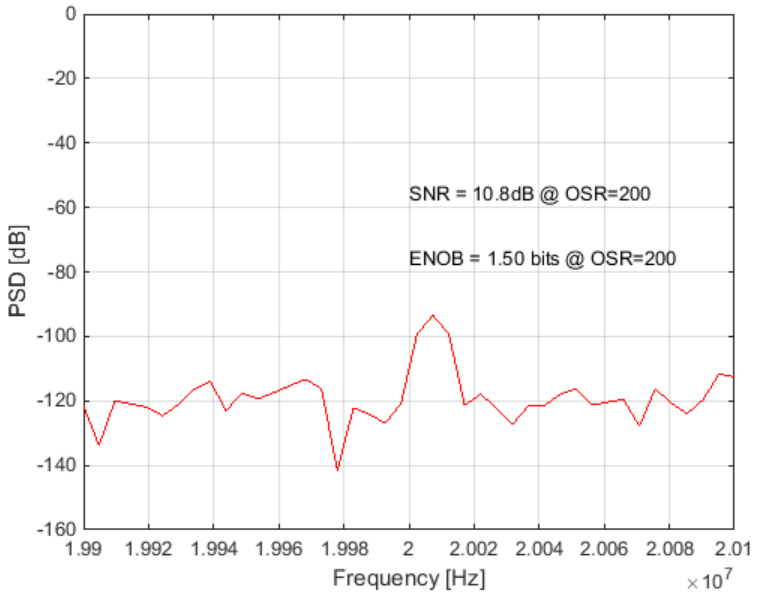

(a)

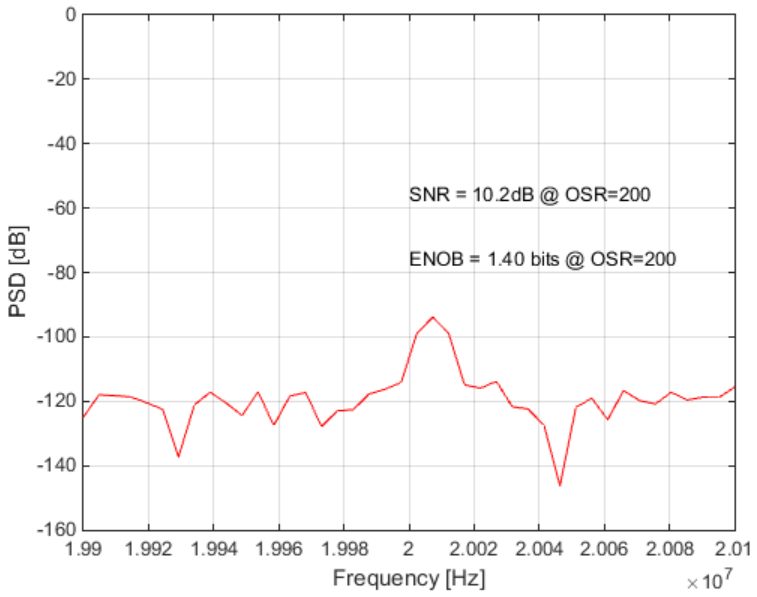

(b)

Figure 3.2.5 Power spectral density of an ideal BPCTDSM with proposed single-opamp resonator at (a) –90 dBFS input, BW_{opamp} = 2 MHz and (b) –90 dBFS input, BW_{opamp} = 1 MHz.

CHAPTER 4

DESIGN AND IMPLEMENTATION

4.1 BEHAVIORAL-LEVEL DESIGN

The Delta-Sigma Toolbox is a well-established open-source library for high-level design and simulation of DSMs. However, when it is used to design a CTDSM, there is an issue in scaling the coefficients. The "realizeNTF_ct" function, which is provided from the Toolbox, converts an NTF from the DT domain to the CT domain using an impulse-invariant transformation. However, coefficient scaling in the DT domain is performed by "mapCtoD" function, which uses a state-space transformation to convert the state-space matrix from the CT domain to the DT domain. Since different methods are used for the conversion between DT and CT domains, and back again, unexpected coefficients may appear in the state-space matrix and modify the chosen NTF.

Figure 4.1.1 shows a proposed behavioral-level design procedure [4.1.1]. First, an NTF generated in DT domain (NTFZ) is converted to CT domain (NTFS) using impulse-invariant transformation. Second, an ELD compensated NTF in CT domain (NTFS_ELD) is verified by impulse response to be identical to NTFZ. Third, the coefficient scaling is

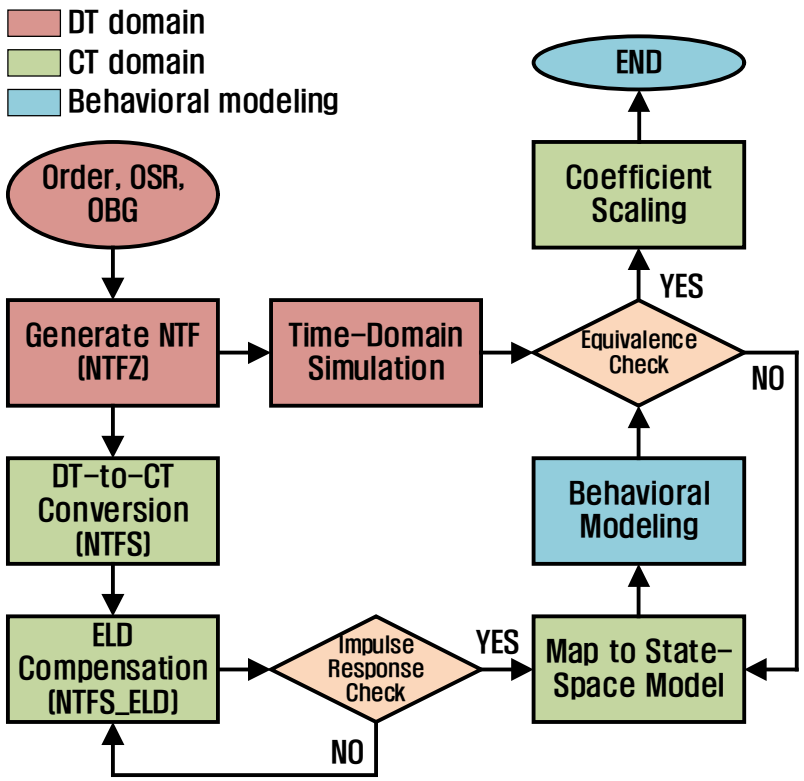

Figure 4.1.1 Behavioral-level design procedure.

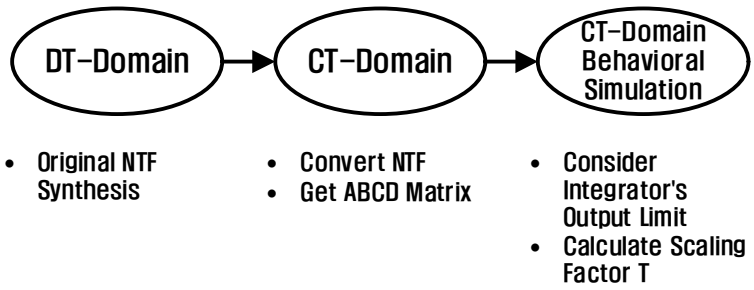

Figure 4.1.2 Coefficient scaling procedure.

performed in the CT domain. Unlike the Delta-Sigma Toolbox, which uses two different transformation methods for converting an NTF from DT domain to CT domain and vice versa, the proposed procedure uses impulse-invariant transformation to an NTF from DT domain to CT domain, as shown in Figure 4.1.2. Therefore, unexpected coefficients do not appear, and the stability of the modulator in CT domain is preserved. The scaling factor T is determined by the maximum level of the integrator output, which is user-defined value, and the maximum level of the integrator outputs, which are obtained from the behavioral simulation. A n^{th}-order modulator has n integrators, and therefore the size of T is n-by-n. This approach to coefficient scaling can be applied to any structure. The ABCD matrix in DT domain can be converted to CT domain as follows:

$$A_S = TAT^{-1}, \quad B_S = TB, \quad C_S = CT^{-1}, \quad D_S = D \tag{4.1.1}$$

$$T = \begin{pmatrix} \frac{A_{MAX}}{y_1} & 0 & \cdots & 0 \\ 0 & \frac{A_{MAX}}{y_2} & \cdots & 0 \\ \vdots & \vdots & \ddots & \vdots \\ 0 & 0 & \cdots & \frac{A_{MAX}}{y_n} \end{pmatrix} \tag{4.1.2}$$

where A_S, B_S, C_S, D_S are the ABCD matrix in CT domain, A_{MAX} is the user-defined maximum level of the integrator output, and y_n is the maximum level of the nth integrator output. The NTFs of a 4^{th}-order and 6^{th}-order feedforward topology BPDTDSMs are generated by using the Delta-Sigma Toolbox as follow:

$$NTF_{Z1} = \frac{z\left(0.9708 + 1.8864z^2\right)}{\left(1+z^2\right)^2} \tag{4.1.3}$$

$$NTF_{Z2} = \frac{z\left(0.9226 + 2.5978z^2 + 2.1939z^4\right)}{\left(1+z^2\right)^3} \tag{4.1.4}$$

$$NTF_{Z3} = \frac{z\left(0.9232 + 2.5860z^2 + 2.1840z^4\right)}{\left(1+z^2\right)^3} \tag{4.1.5}$$

where NTF_{Z1}, NTF_{Z2}, and NTF_{Z3} are for gingival, vascular, and cardiac modes, respectively. The target specifications are summarized in Table 4.1.1. The NTFs in DT domain are converted to CT domain by utilizing impulse-invariant transformation and derived as follow:

$$NTF_{S1} = \frac{4.3487F_S^{\,4} + 4.2204F_S^{\,3}s + 2.4816F_S^{\,2}s^2 + 1.2527F_S s^3}{\left(\left(\frac{\pi F_S}{2}\right)^2 + s^2\right)^2} \tag{4.1.6}$$

$$NTF_{S2} = \frac{\begin{pmatrix} 10.7298F_S^{\,6} + 11.8639F_S^{\,5}s + 12.1434F_S^{\,4}s^2 \\ + 8.5573F_S^{\,3}s^3 + 2.8998F_S^{\,2}s^4 + 1.3543F_S s^5 \end{pmatrix}}{\left(\left(\frac{\pi F_S}{2}\right)^2 + s^2\right)^3} \tag{4.1.7}$$

Table 4.1.1 Target specifications of the multi-mode BPCTDSM.

	Gingival-Mode	**Vascular-Mode**	**Cardiac-Mode**
Order	4	6	6
Center Frequency F_C	20 MHz	5 MHz	2 MHz
Sampling Frequency F_S	80 MHz	20 MHz	8 MHz
Bandwidth F_B		200 kHz	
Target DR		> 85 dB	

$$NTF_{S3} = \frac{\left(\begin{array}{l} 10.6902F_S{}^6 + 11.7979F_S{}^5 s + 12.0957F_S{}^4 s^2 \\ \qquad + 8.5192F_S{}^3 s^3 + 2.8857F_S{}^2 s^4 + 1.3489F_S s^5 \end{array}\right)}{\left(\left(\frac{\pi F_S}{2}\right)^2 + s^2\right)^3} \tag{4.1.8}$$

where NTF_{S1}, NTF_{S2}, and NTF_{S3} are the converted NTF for gingival, vascular, and cardiac modes, respectively.

Figure 4.1.3(a) and Figure 4.1.3(b) show the behavioral-level models of 4th-order BPCTDSM for gingival-mode and 6th-order BPCTDSM for cardiac and vascular modes. The NTFs from Figure 4.1.3(a) and 4.1.3(b) can be expressed as follow:

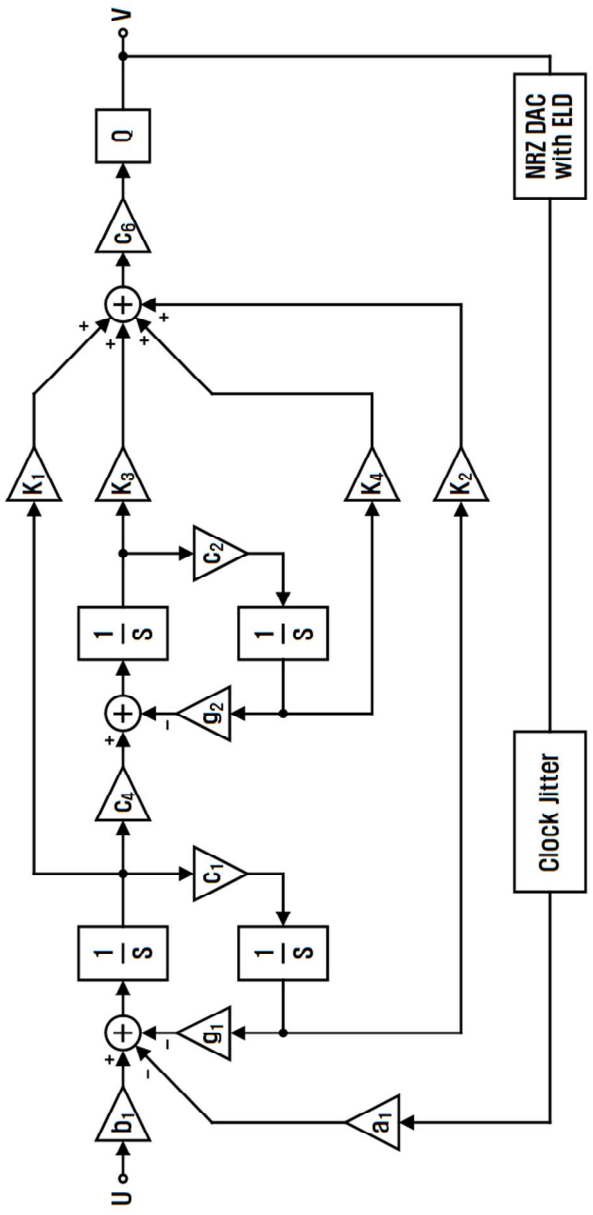
U
V
Q
NRZ DAC
with ELD
Clock Jitter
$a_1=b_1=0.3927$, $g_1=c_1=g_2=c_2=1.5708$, $c_4=0.3927$, $c_6=0.4444$, $K_1=3.1899$, $K_2=2.8572$, $K_3=4.6631$, $K_4=4.6631$

(a)

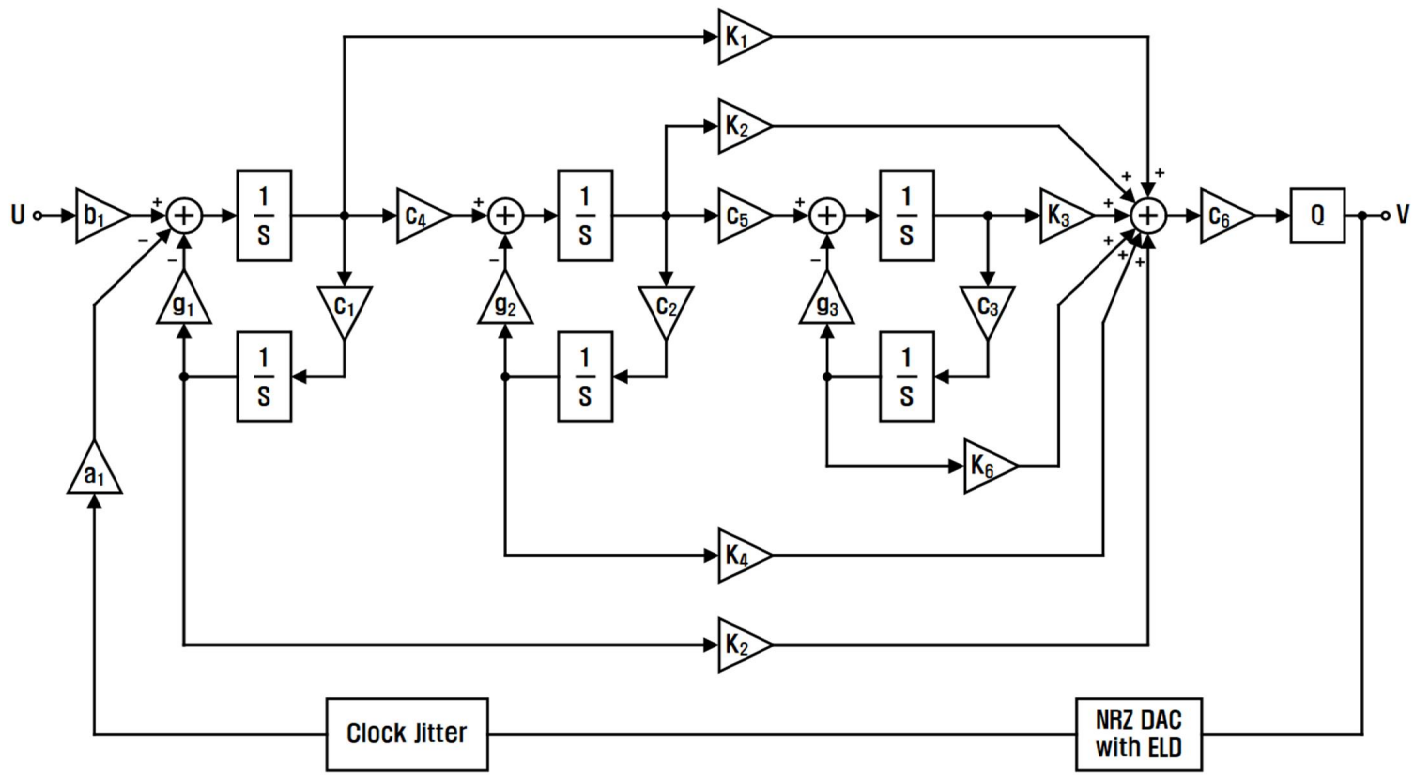

$a_1=b_1=0.7854$, $g_1=c_1=g_2=c_2=g_3=c_3=1.5708$, $c_4=c_5=0.3927$, $c_6=0.4444$, $K_1=1.7244$, $K_2=1.4286$, $K_3=3.6874$, $K_4=3.0272$, $K_5=3.3637$, $K_6=3.3634$

(b)

Figure 4.1.3 Behavioral-level models of (a) a 4th-order BPCTDSM for gingival-mode and (b) a 6th-order BPCTDSM for vascular and cardiac modes.

$$NTF_{S1}' = \frac{-a_1 c_6 \left(c_1 c_2 g_2 k_2 F_S^{\,4} + c_2 \left(g_2 k_1 + c_4 k_4 \right) F_S^{\,3} s + \left(c_1 k_2 + c_4 k_3 \right) F_S^{\,2} s^2 + k_1 F_S s^3 \right)}{\left(c_1 g_1 F_S^{\,2} + s^2 \right) \left(c_2 g_2 F_S^{\,2} + s^2 \right)} \tag{4.1.9}$$

$$NTF_{S2,3}' = \frac{-a_1 c_6 \left(\begin{array}{l} c_1 c_2 c_3 g_2 g_3 k_2 F_S^{\,6} + c_2 c_3 g_3 \left(g_2 k_1 + c_4 k_4 \right) F_S^{\,5} s \\ + \left(c_1 k_2 \left(c_2 g_2 + c_3 g_3 \right) + c_3 c_4 k_3 \left(g_3 k_3 + c_5 k_6 \right) \right) F_S^{\,4} s^2 \\ + \left(c_3 g_3 k_1 + c_2 \left(g_2 k_1 + c_4 k_4 \right) + c_4 c_5 k_5 \right) F_S^{\,3} s^3 \\ + \left(c_1 k_2 + c_4 k_3 \right) F_S^{\,2} s^4 + k_1 F_S s^5 \end{array} \right)}{\left(c_1 g_1 F_S^{\,2} + s^2 \right) \left(c_2 g_2 F_S^{\,2} + s^2 \right) \left(c_3 g_3 F_S^{\,2} + s^2 \right)} \tag{4.1.10}$$

The coefficients are obtained by solving (4.1.9) to be identical to (4.1.6) for gingival-mode and (4.1.10) to be equal to (4.1.7) for vascular-mode, and (4.1.10) to be identical to (4.1.8) for cardiac-mode. The resonators are modeled as conventional topology, which consists of two opamps, to obtain the feedforward coefficients. The behavioral-level models of the NRZ DAC with ELD and clock jitter are shown in Figure 4.1.4(a) and 4.1.4(b), respectively. Clock jitter is modeled as an amplitude error of the DAC, rather than as a timing error of the clock. This approach does not require a smaller time-step than the clock period, which helps to avoid excessive simulation time. Figure 4.1.5(a) and Figure 4.1.5(b) show behavioral-level simulation results of SNR against normalized ELD and clock jitter, respectively. ELD of 100% is used, and additional path for ELD compensation is not needed.

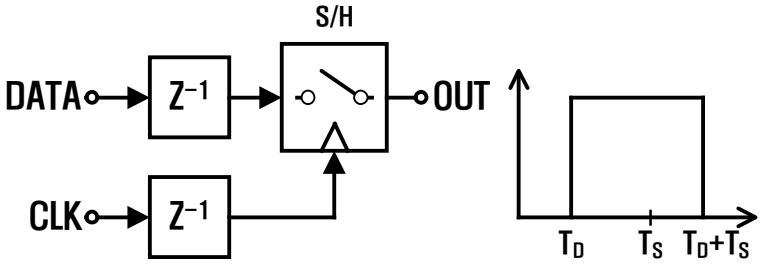

(a)

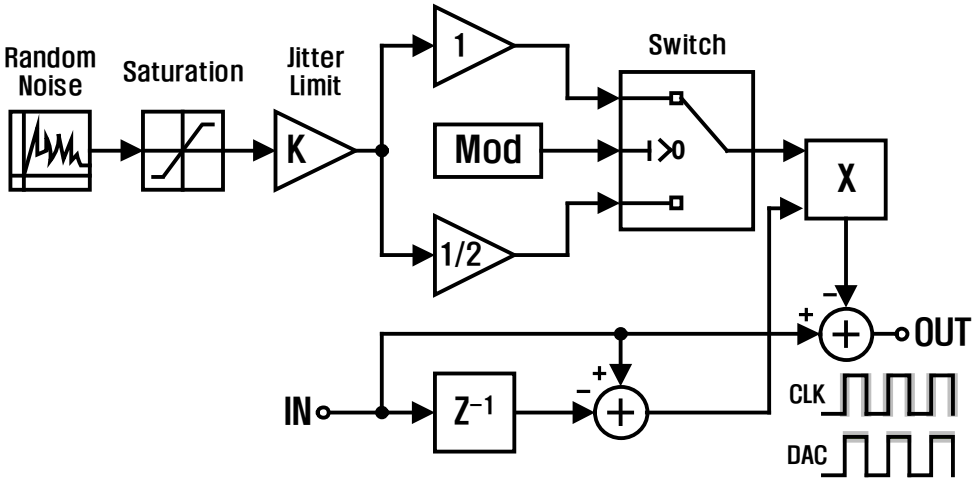

(b)

Figure 4.1.4 Behavioral-level models of (a) a NRZ DAC with ELD and (b) clock jitter.

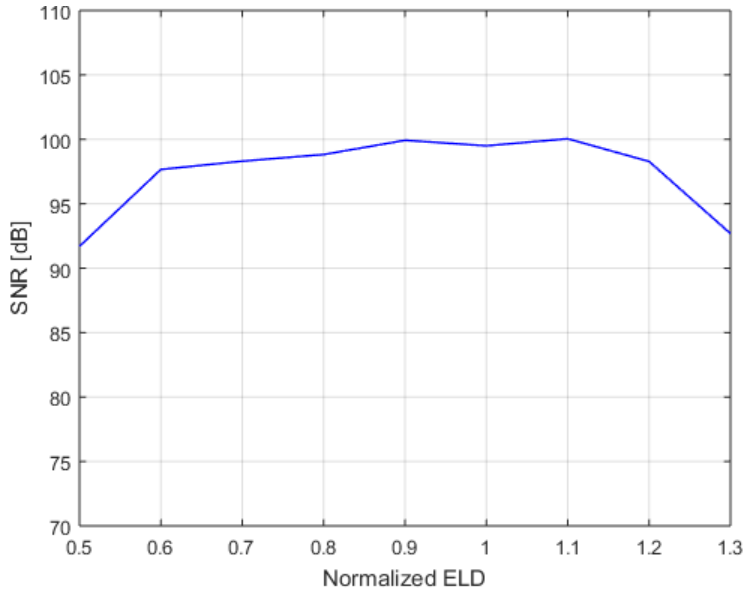

(a)

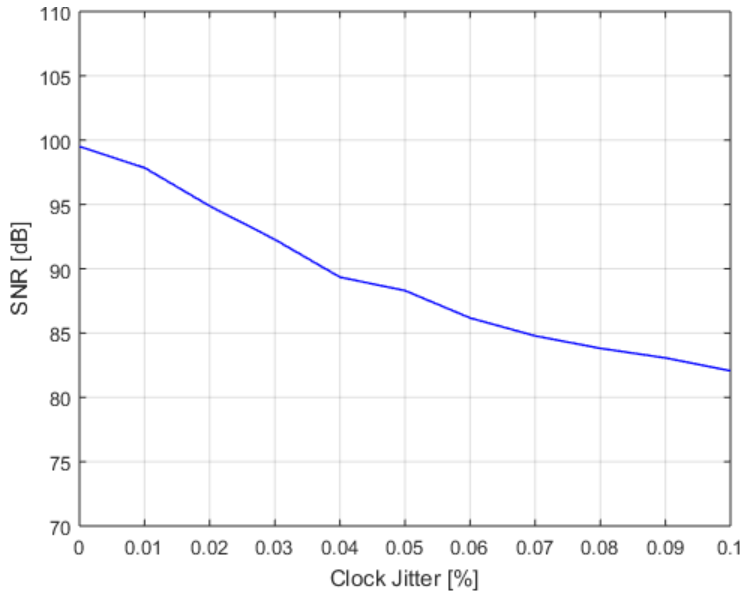

(b)

Figure 4.1.5 Behavioral-level simulation results of SNR against (a) normalized ELD and (b) clock jitter.

4.2 CIRCUIT-LEVEL DESIGN

Figure 4.2.1 shows the block diagram of the proposed multi-mode BPCTDSM. The modulator consists of resonators, 4-bit quantizer, 4-bit current DAC, and peripheral blocks. In gingival-mode, 4^{th}-order BPCTDSM is realized by disconnecting the third resonator and few feedforward paths, which are grey colored in Figure 4.2.1. In vascular-mode and cardiac-mode, 6^{th}-order BPCTDSM is realized by connecting all blocks shown in Figure 4.2.1. The capacitors in the loop filter are controlled by 9-bit control signals, coarse tuning with 4-bit and fine tuning with 5-bit. The unit capacitances of coarse and fine tuning are 775.38 fF and 24.66 fF, respectively. The positive feedback resistors for compensating Q of the resonator are controlled by 6-bit signals. The values of the coefficients are given in Table 4.2.1, which are calculated not considering $R_{C1\text{-}3}$.

A BPDSM in feedforward topology requires feedforward paths, which are k_n as shown in Figure 4.1.3(a) and Figure 4.1.3(b), from the output of each integrator. These paths can be easily implemented when using a conventional active resonator that consists of two opamps, as shown in Figure 4.2.2(a). However, due to the usage of a single opamp, one of the feedforward paths needs to be connected between the passive components V_X, which is shown in Figure 4.2.2(b). The feedforward path from V_X will affect to the transfer function of the single-opamp resonator, and since V_X is no longer the input or output of the opamp, the fluctuation in V_X can affect the stability of the modulator. The transfer function of the conventional active resonator and the prior single-opamp resonator can be derived as follows:

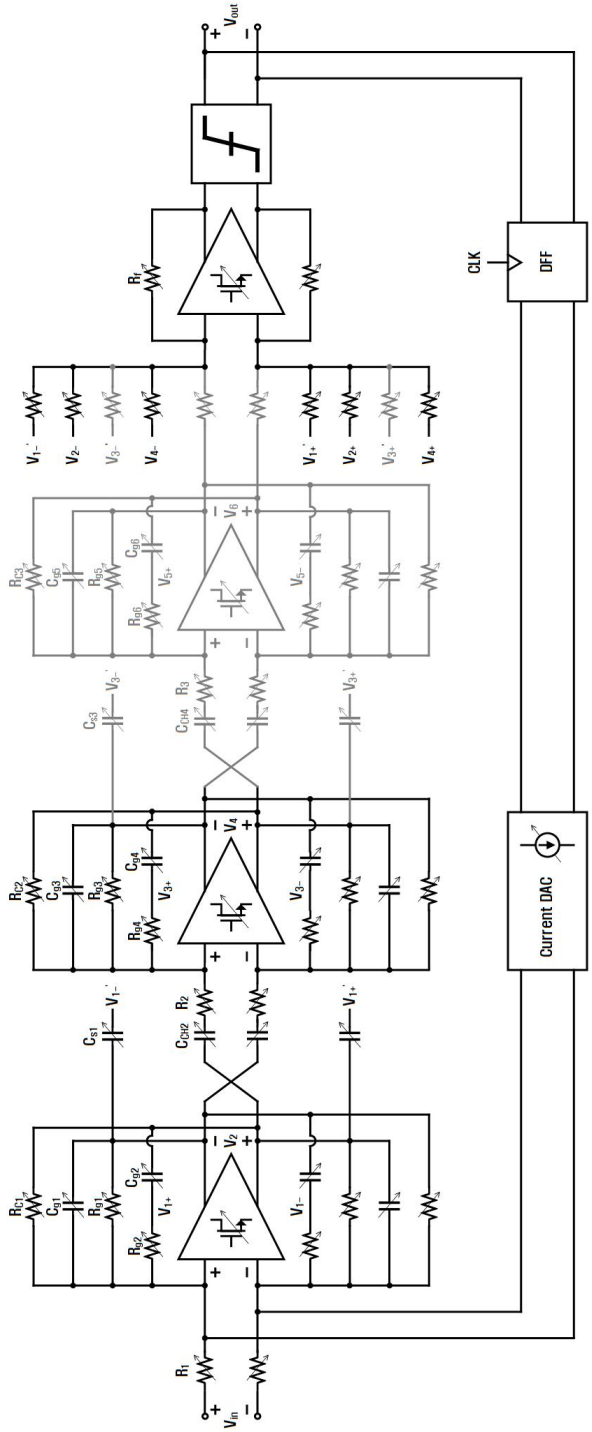

Figure 4.2.1 Block diagram of the proposed multi-mode BPCTDSM.

Table 4.2.1 Coefficients of multi-mode BPCTDSM

Coefficients	Gingival-Mode	Vascular-Mode	Cardiac-Mode
$C_{1,3}$	3.98 pF	3.98 pF	9.95 pF
C_5	N/A	3.98 pF	9.95 pF
$C_{2,4}$	7.96 pF	7.96 pF	19.89 pF
C_6	N/A	7.96 pF	19.89 pF
$R_{g1,3}$	2 kΩ	8 kΩ	8 kΩ
R_{g5}	N/A	8 kΩ	8 kΩ
$R_{g2,4}$	1 kΩ	4 kΩ	4 kΩ
R_{g6}	N/A	4 kΩ	4 kΩ
R_1	8 kΩ	16 kΩ	16 kΩ
R_2	8 kΩ	32 kΩ	32 kΩ
R_3	N/A	32 kΩ	32 kΩ
R_f	2 kΩ	8 kΩ	8 kΩ
R_{s1}	13.53 kΩ	60.85 kΩ	60.85 kΩ
R_{s2}	1.58 kΩ	12.60 kΩ	12.60 kΩ
R_{s3}	N/A	27.26 kΩ	27.26 kΩ
R_{s4}	0.97 kΩ	5.95 kΩ	5.95 kΩ
R_{s6}	N/A	5.35 kΩ	5.35 kΩ
C_{CH2}	0.99 pF	0.99 pF	2.49 pF
C_{CH4}	N/A	0.99 pF	2.49 pF
C_{s1}	0.59 pF	0.52 pF	1.31 pF
C_{s3}	N/A	1.17 pF	2.92 pF
I_{DAC}	7.5 μA	3.75 μA	3.75 μA

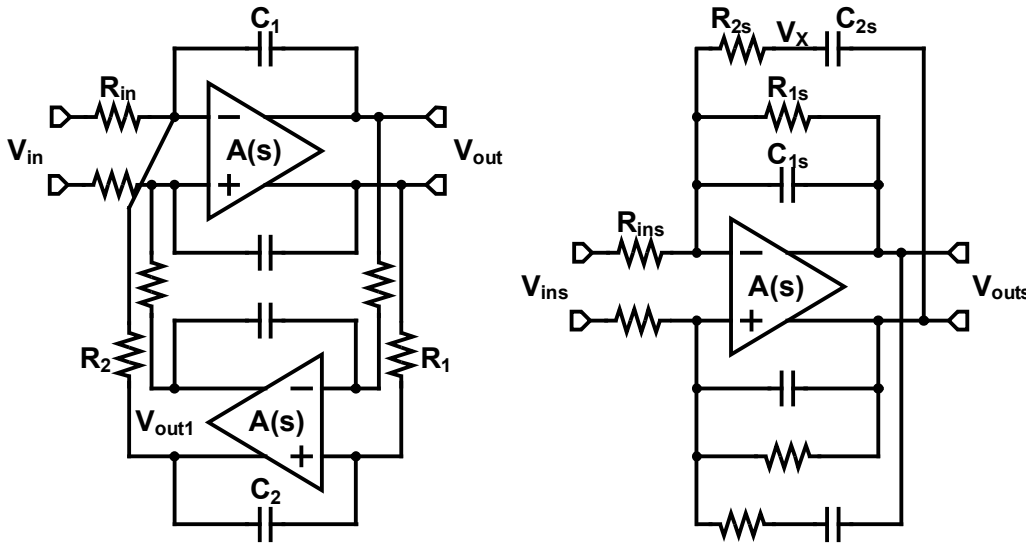

(a) (b)

Figure 4.2.2 Block diagram of (a) the conventional active resonator and (b) the prior single-opamp resonator.

$$V_{out} = -\frac{\dfrac{s}{C_1 R_{in}}}{s^2 + \dfrac{1}{C_1 C_2 R_1 R_2}} \qquad V_{out1} = -\frac{\dfrac{1}{C_1 C_2 R_1 R_2}}{s^2 + \dfrac{1}{C_1 C_2 R_1 R_2}} \tag{4.1.11}$$

$$V_{outs} = -\frac{\dfrac{1}{C_{1s} R_{ins}}\left(s + \dfrac{1}{C_{2s} R_{2s}}\right)}{s^2 + \dfrac{1}{C_{1s} C_{2s} R_{1s} R_{2s}}} \qquad V_X = -\frac{\dfrac{s}{C_{1s} R_{1s}}}{s^2 + \dfrac{1}{C_{1s} C_{2s} R_{1s} R_{2s}}} \tag{4.1.12}$$

As shown in (4.1.11) and (4.1.12), the outputs in the conventional active resonator, V_{out}, and V_{out1}, are shown at the output of the single-opamp resonator, V_{outs}. Therefore, if the feed-forward coefficients from the first integrator and the second integrator in the conventional active resonator are the same, these two paths can be combined with a single feedforward path. The feedforward coefficients from each resonator can be the same through the coefficient scaling. By adjusting the maximum output range of the integrators individually, the feedforward coefficients from each resonator become identical and therefore the feedforward path from V_X is no longer needed. Although the feedforward path issue is solved, there is one more problem. Among the two outputs of the resonator in (4.1.11), the signal of V_{out} is transferred to the next input of the resonator. The corresponding output in the single-opamp resonator is V_X, and the same issue that occurred above arises again. By configuring a high-pass filter after V_{outs}, the same transfer function to V_{out} can be implemented without touching the inner voltage node [3.1.2].

4.2.1 OPAMP

Figure 4.2.3 shows a schematic of the opamp in the proposed resonator. Using a feedforward topology is appropriate to achieve both high gain and wide bandwidth [4.2.1], [4.2.2]. Same opamps are used in the second and third integrators and also in the adder. Since the center frequency of the resonator in each mode is different, required specifications to the opamp also vary according to the system mode. It is designed to achieve 40 dB of gain at the center frequency in each mode by adjusting the number of

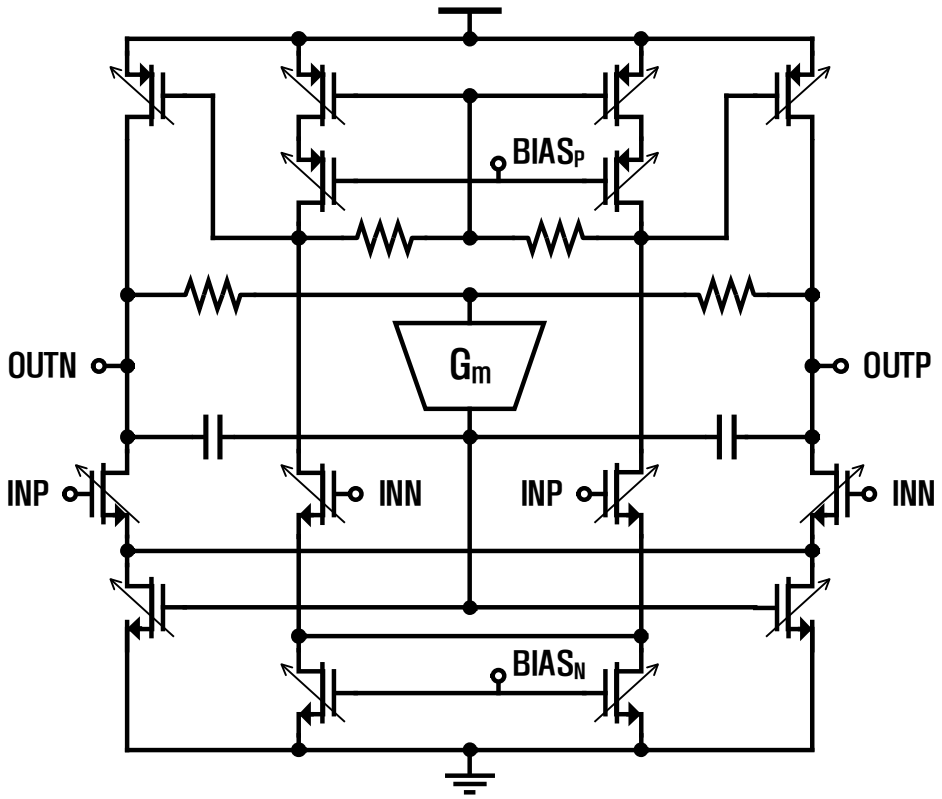

Figure 4.2.3 Schematic of the opamp.

transistors for power efficiency. The DC gain of opamps achieve more than 40 dB, and the phase margins are around 90 degrees. Table 4.2.2 shows the designed specifications of the opamps for gingival, vascular, and cardiac modes. Figure 4.2.4 show the bode plots of the opamp in multi-modes. The bode plots of the prior single-opamp resonator and the proposed single-opamp resonator in gingival mode are shown in Figure 4.2.5(a) and Figure 4.2.5(b). The same opamp is used for the prior and the proposed resonators, where

Table 4.2.2 Specifications of the opamp in tri-mode

	Gingival-Mode	**Vascular-Mode**	**Cardiac-Mode**
Gain @ DC	57.62 dB	48.39 dB	43.94 dB
Gain @ F_C	40.04 dB	40.62 dB	39.84 dB
Phase Margin	96.27 °	93.04 °	88.07 °
Unit GBW	2.61 GHz	1.33 GHz	1.22 GHz
Current Consumption	7.07 mA	3.54 mA	2.52 mA

the gain of an opamp at the center frequency of 20 MHz is designed to 40 dB. The proposed single-opamp resonator achieves higher peak amplitude at the center frequency and narrower bandwidth than the prior single-opamp resonator. As a result, Q of the proposed single-opamp resonator is higher than the prior single-opamp resonator and therefore enhances the performance of the modulator.

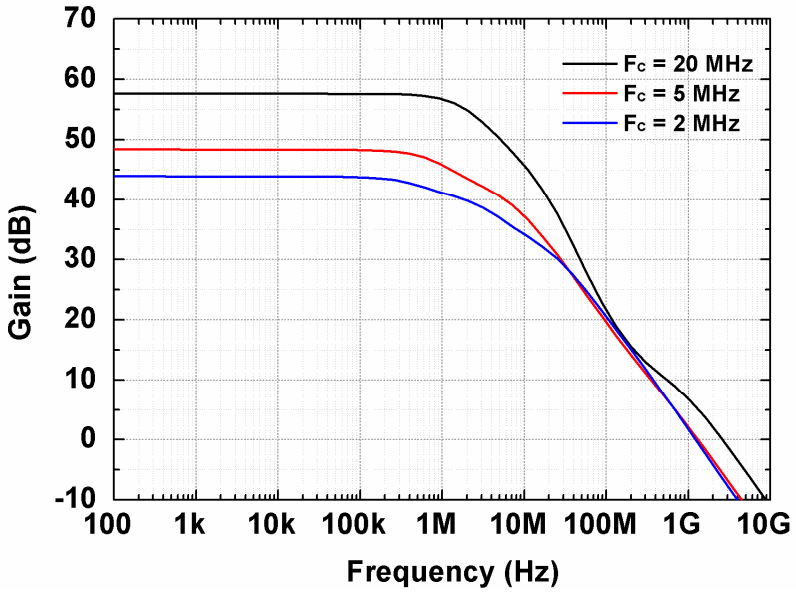

(a)

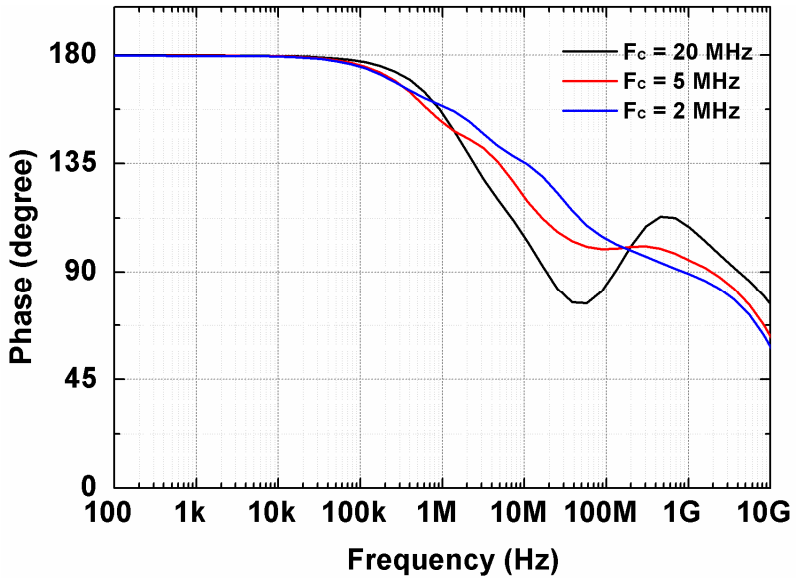

(b)

Figure 4.2.4 Bode plot of the opamp in multi-modes.

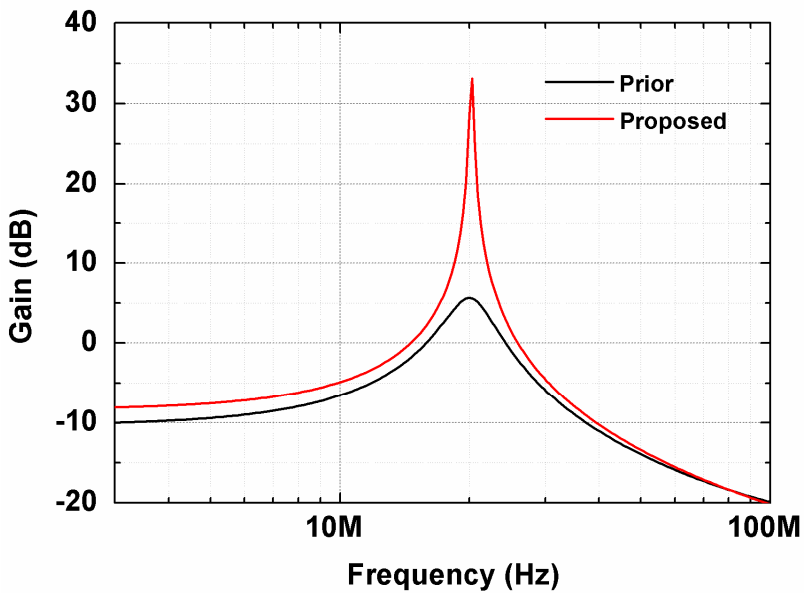

(a)

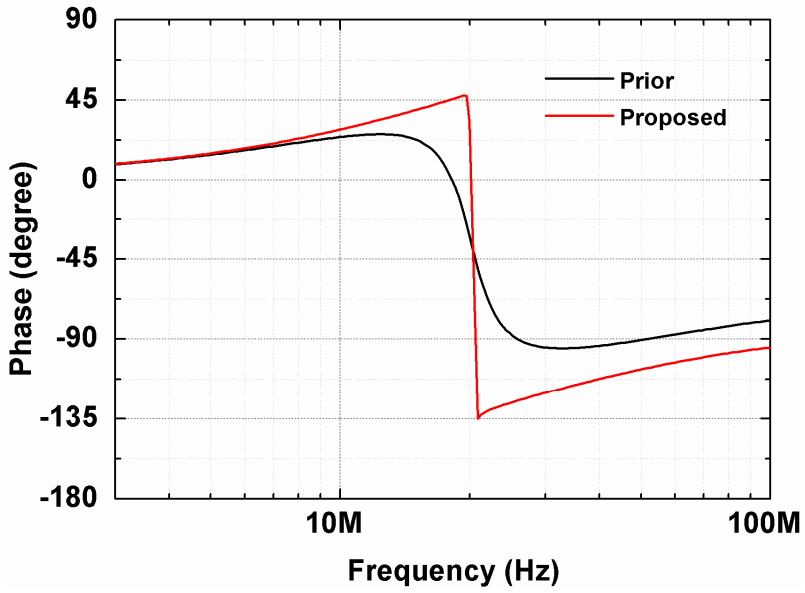

(b)

Figure 4.2.5 Bode plots of the prior single-opamp resonator and the proposed single-opamp resonator in gingival-mode.

4.2.2 QUANTIZER

Figure 4.2.6 shows a schematic of the 4-bit flash ADC, which is used as a quantizer. Using a multi-bit quantizer has an advantage of increasing the performance of the modulator effectively. However, the number of quantizer bits cannot be increased too high due to the increase of area and power consumption and therefore 4-bit quantizer is chosen. The outputs of the comparators are presented as a thermometer code, which can contain bubbles of those are static or dynamic errors in the comparator. Therefore, bubble error correction logic is used to prevent incorrect decisions. Switching errors in the resistive ladder are prevented by using the 4-input comparator, which is shown in Figure 4.2.7. The comparator consists of preamplifier, latch, and SR-latch. It is firmly designed to achieve the offset of the comparator less than 1/3 LSB, where 1 LSB is 50 mV. Monte-Carlo simulation is used to confirm 99.7 % (3-σ) of the comparator offsets are within 1/3 LSB, which results in an offset calibration is unnecessary.

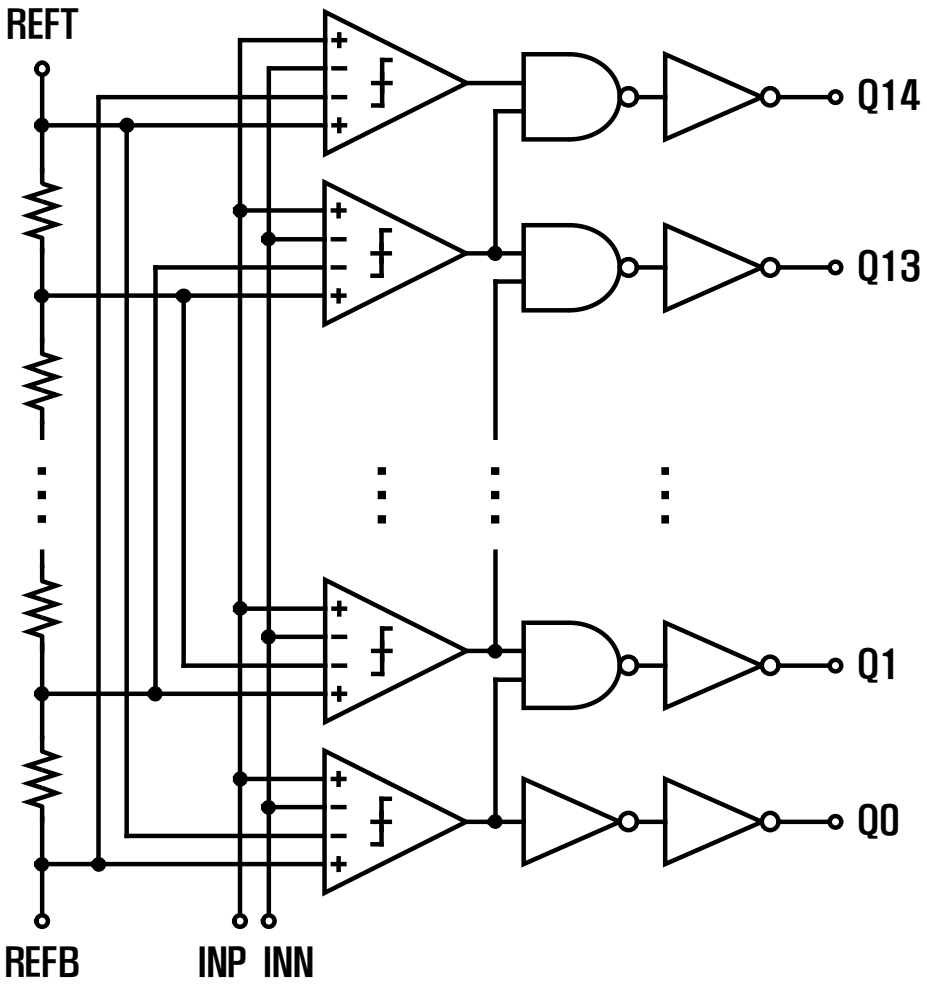

Figure 4.2.6 Schematic of the 4-bit flash ADC.

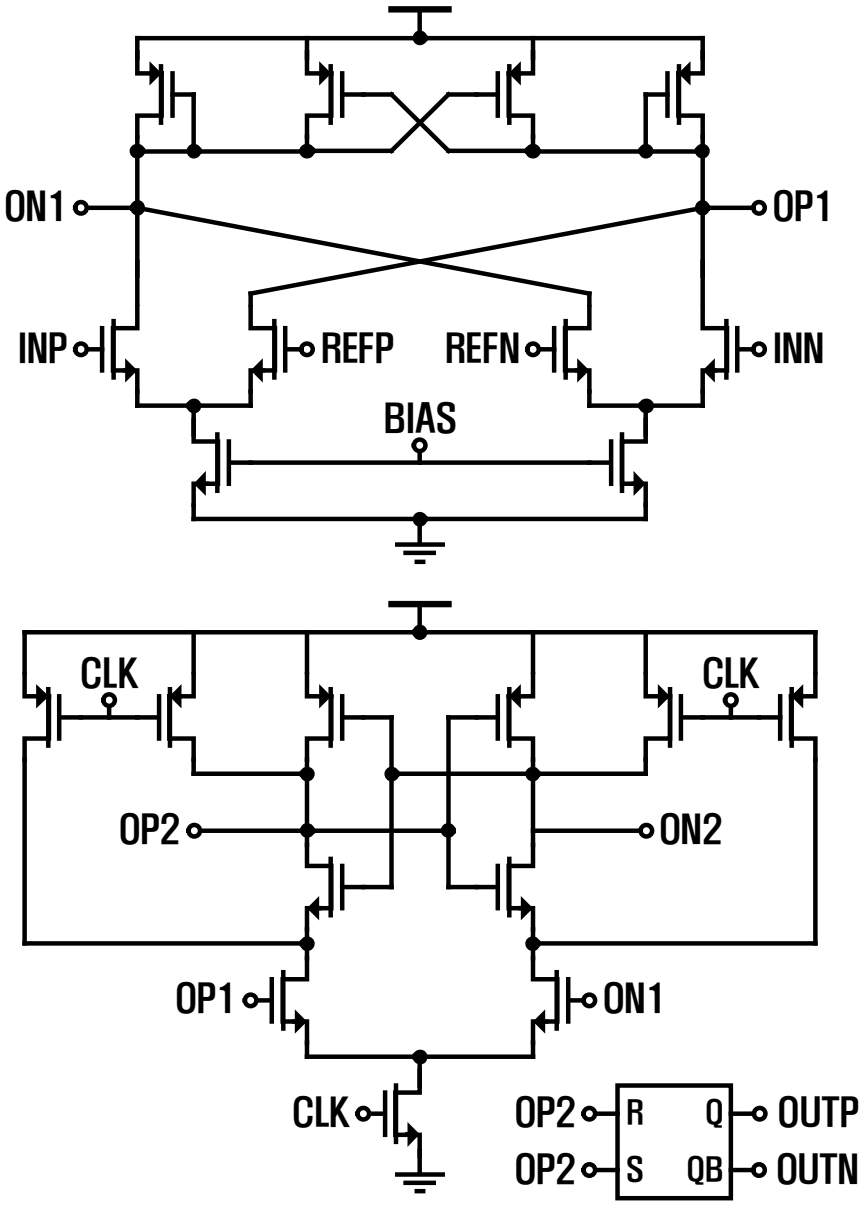

Figure 4.2.7 Schematic of the comparator.

4.2.3 CURRENT DAC

Figure 4.2.8 shows a schematic of the 4-bit current-steering feedback DAC. To minimize the effect of the mismatch between I_P and I_N, the current source devices M_P and M_N are sized to have large lengths. The distortion is generated by the combination of the parasitic capacitances at the current source nodes C_P and C_N, and the offsets of the first integrator [4.2.3]. Moreover, $C_{P,N}$ and the transitions of $V_{P,N}$ are proportional to an inter-symbol interference error current [4.2.4]. Therefore, parasitic capacitance of each current source node, including the capacitance of the layout, is kept below 5 fF. The current-steering DAC is designed to achieve 10-bit resolution, and it is verified by Monte-Carlo simulation. The unit current varies depending on the system mode. In the gingival-mode, both SW_0 and SW_1 are turned on. In other modes, only SW_0 is turned on.

It is well known that using a multi-bit quantizer is a good solution to mitigate the effect of clock jitter. However, it also causes current mismatches in feedback DAC cells at the same time. The DEM logic rotates the use of the feedback DAC cells, and thus randomize the noise from the feedback DAC. In general, the DEM logic is necessarily required in LP-CTDSM. However, the DEM logic in BPCTDSM might be a bad choice. The key point of the DEM logic is that the randomized noise from the feedback DAC is spread and increase the thermal noise. The performance of BPCTDSM, especially in case of F_C/F_B is small, is closely related to the thermal noise. Therefore, using a DEM logic may rather degrade the performance of BPCTDSM, and most BPCTDSMs do not include the DEM logic.

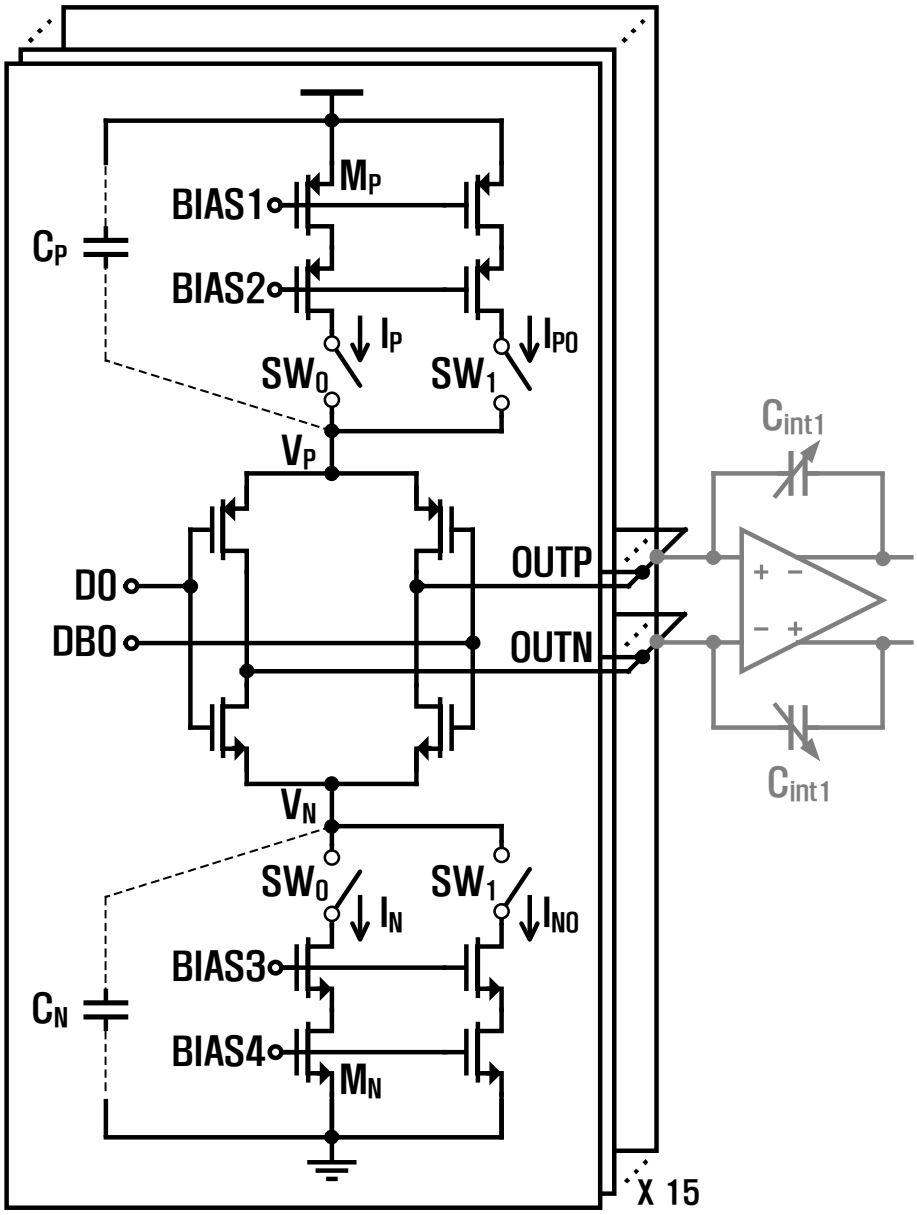

Figure 4.2.8 Schematic of the 4-bit current DAC.

4.2.4 PERIPHERAL BLOCKS

Thermometer-to-binary converter (T2B) is used to decrease the number of output bits, as shown in Figure 4.2.9. The 16-level quantizer output, T<14:0>, that presents the thermometer code is converted to 5-bit binary code, B<4:0>, where the LSB of the binary code is always VDD. A beta multiplier, which provides bias current for opamps, quantizer, and current DAC, is used. The output current from the beta multiplier can be adjusted in 4-bit control. The current varies from 75 % to 125 % of the target current, which can cover the variations of the current from PVT variations. I^2C block is included to control the 19 selection signals, which are DC. The required number of pins for I^2C block is only 4 that largely decreases the amount of package pins.

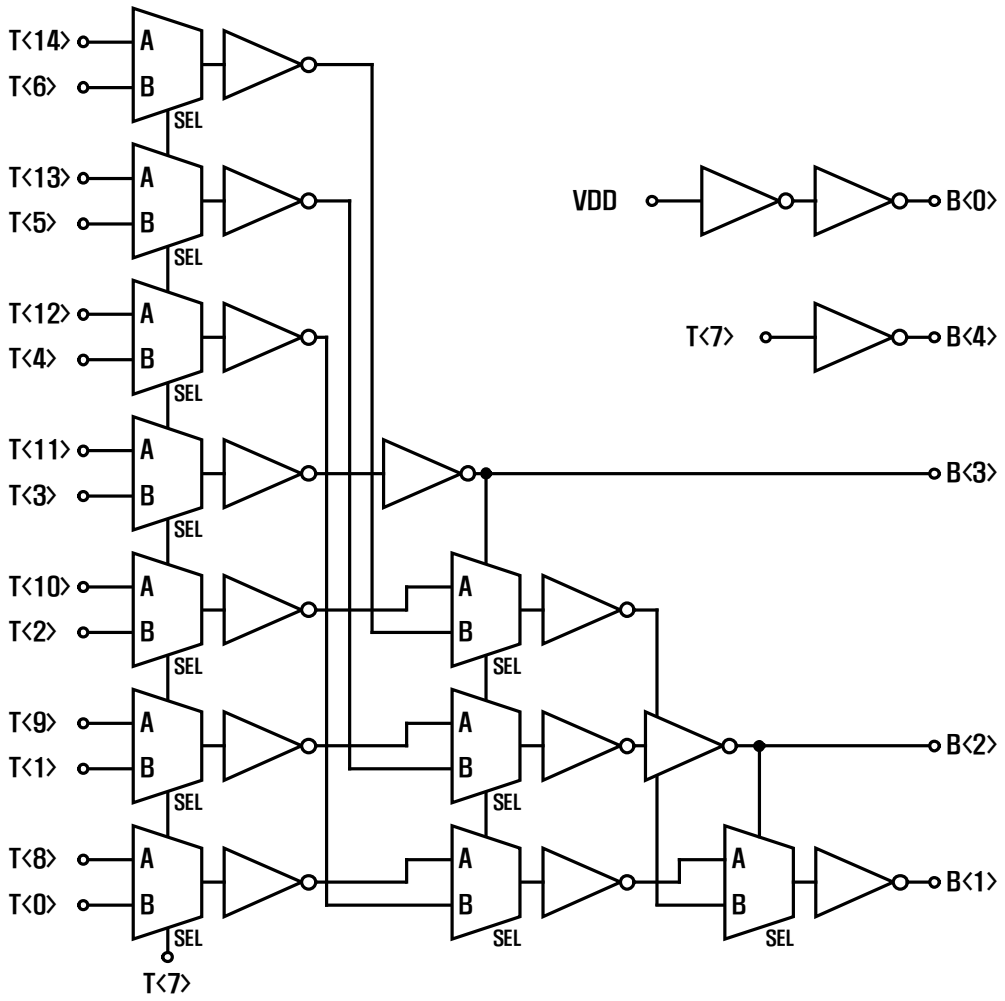

Figure 4.2.9 Schematic of the thermometer-to-binary converter.

4.3 SIMULATION RESULTS

Figure 4.3.1(a) and Figure 4.3.1(b) show the power spectral density of the gingival-mode BPCTDSM, where the center frequency and the sampling frequency of 20 MHz and 80 MHz are used, at –20 dBFS and –85 dBFS input signals, respectively. The SNDR of 65.2 dB and 6.7 dB are achieved at –20 dBFS and –85 dBFS input signals, respectively. To clarify the effect of our proposed high Q single-opamp resonator, simulations are performed to the modulator with the prior single-opamp resonator in [2.3.2], and the same opamp that used in the gingival-mode BPCTDSM is used. The power spectral density of the modulator with the prior single-opamp resonator at –20 dBFS achieves the SNDR of 46.2 dB, as shown in Figure 4.3.2. Due to the increased noise floor around the center frequency, from 100 dB to 80 dB, –85 dBFS input signal cannot be detected in the modulator with the prior single-opamp resonator. As expected, the prior single-opamp resonator is severely affected by the finite GBW of an opamp. The simulation results show that applying the proposed high Q single-opamp resonator in a BPCTDSM largely improves the performance.

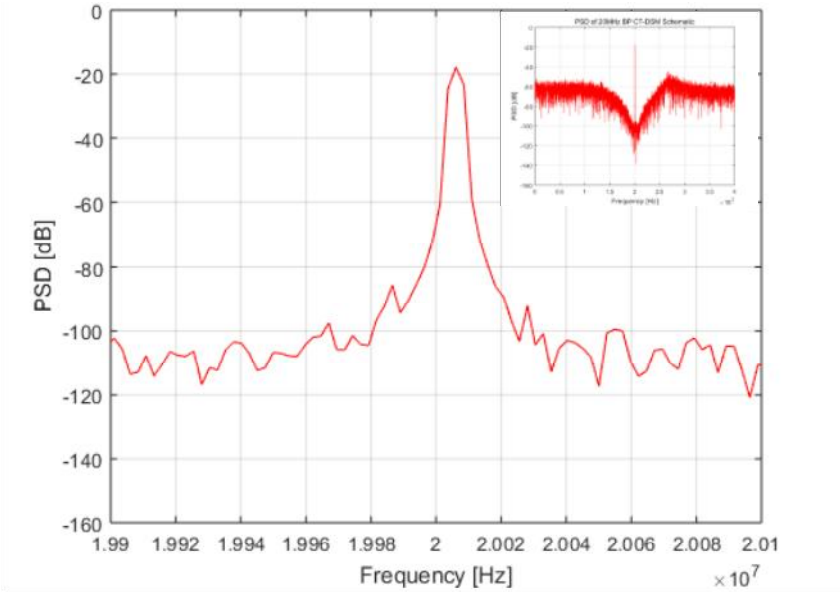

(a)

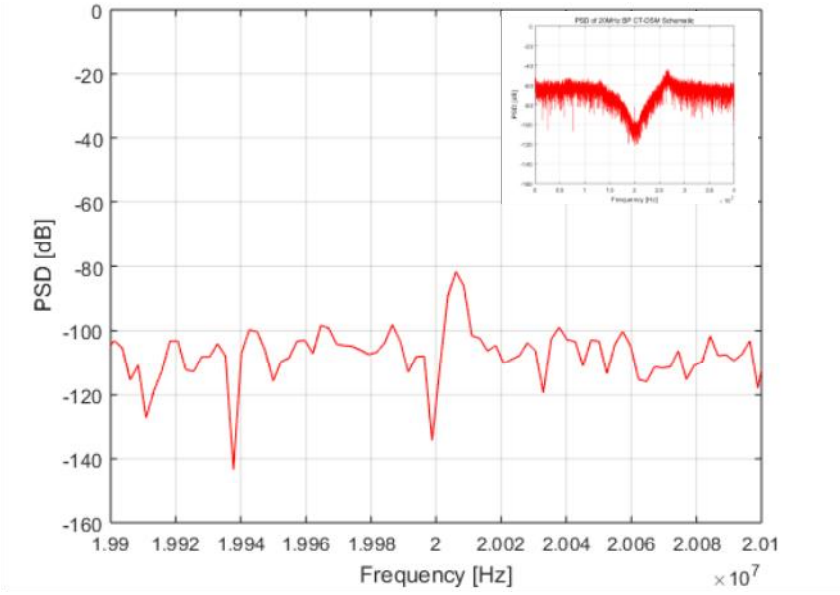

(b)

Figure 4.3.1 Output spectrum density of the gingival-mode BPCTDSM, using the proposed high Q single-opamp resonator, at (a) –20 dBFS input signal and (b) –85 dBFS input signal.

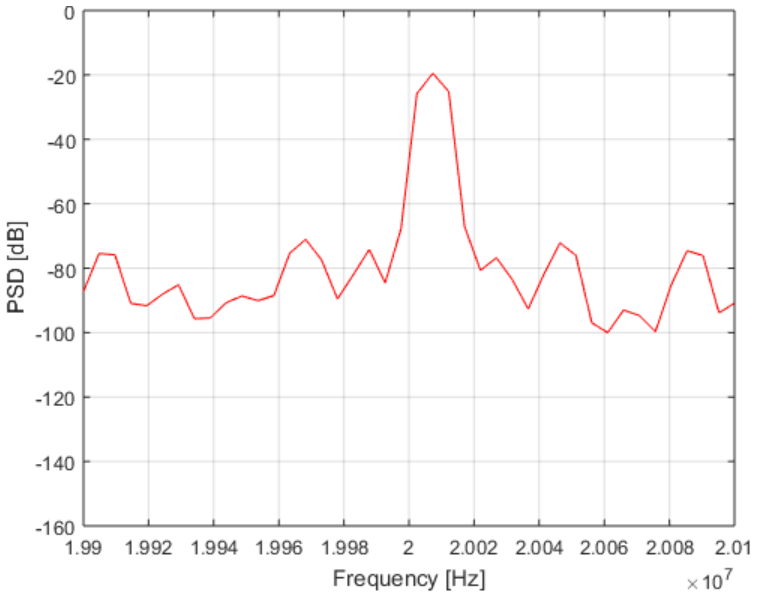

Figure 4.3.2 Output spectrum density of the gingival-mode BPCTDSM, using the prior single-opamp resonator, at –20 dBFS input signal.

CHAPTER 5

MEASUREMENT RESULTS

5.1 MEASUREMENT SETUP

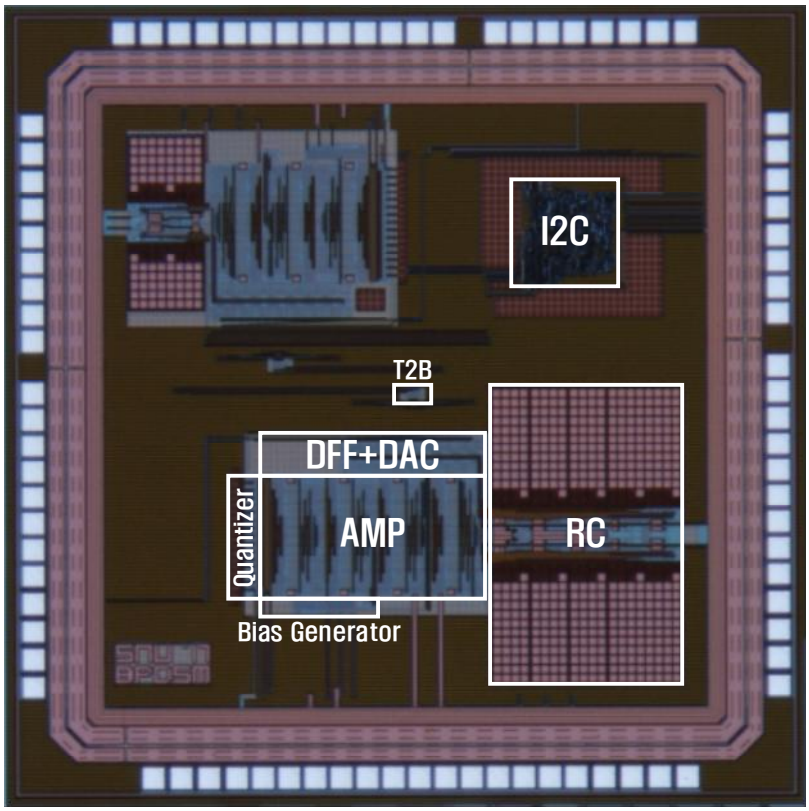

Figure 5.1.1 Chip microphotograph.

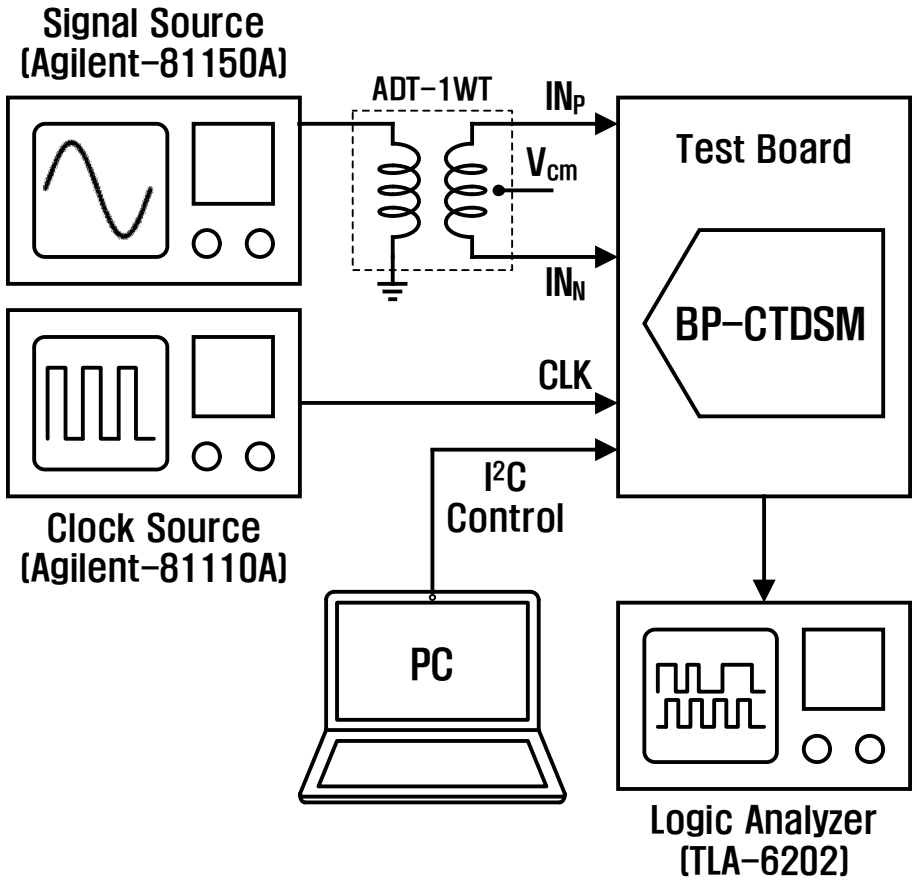

Figure 5.1.2 Experimental setup.

Figure 5.1.1 shows the chip microphotograph of the proposed multi-mode BPCTDSM, which consists of RC network, opamps, quantizer, DAC, a bias generator, T2B, and I^2C. Our BPCTDSM is implemented in 180 nm CMOS process and occupies an area of 0.845 mm^2. A QFN type package with 88 pins are used. To increase the utilization of the test board, a socket is used to connect the test board and the packaged chip. The

experimental setup is shown in Figure 5.1.2. A differential input signal is produced by combining a signal source (Agilent 81150A) through a transformer. The linearity of the differential signals from the transformer can be enhanced by cascading two transformers. The pattern generator (Agilent 81110A) is used to generate the sampling frequency of 8 MHz, 20 MHz, and 80 MHz. The output of the modulator, which is a 5-bit signal, is captured by the logic analyzer (Tektronix TLA6202). A PC is used to control the I^2C block.

5.2 MEASUREMENT RESULTS

Figure 5.2.1(a) shows the measured power spectral density of the gingival-mode BPCTDSM at –6.61 dBFS input signal. The NTF presents a band-pass characteristic and the noise floor around the center frequency of 20 MHz is in the order of 100 dB. Figure 5.2.1(b) shows the measured SNDR against the input amplitude. The input amplitude for the maximum measured SNDR of 68.56 dB is –6.61 dBFS and the minimum detectable signal amplitude is –94.67 dBFS, which indicates a DR of 88.06 dB. To evaluate the effectiveness of utilizing the proposed high Q single-opamp resonator on the modulator, the performance of the modulator is measured with reducing the bias current of the opamp in half, which is shown in Figure 5.2.2(a). When the bias current of the opamp is reduced in half, the gain of the opamp at the center frequency decreases from 41.03 dB to 34.85 dB. Other specifications are shown in Table 5.2.1. Despite the reduced GBW, the NTF maintains the original shape, and the performance is not degraded. Figure 5.2.2(b) shows the measured SNDR against the input amplitude with the reduced bias current of the opamp. The input amplitude for the maximum measured SNDR of 68.58 dB is –6.63 dBFS and the minimum detectable signal amplitude is –97.02 dBFS, which indicates a DR of 90.39 dB. In ideal case, the performance of the modulator can be maintained even if the bias current of the opamp decreases continuously. However, since a low GBW of an opamp increases the fluctuations of the virtual ground nodes, the stability of the modulator might be affected. So, there is a limitation in reducing the bias current without degrading the performance of the modulator.

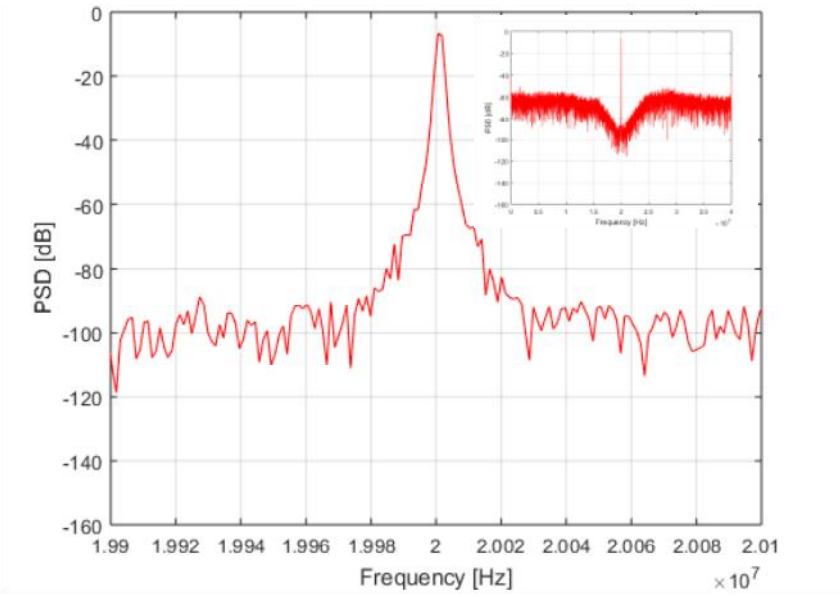

(a)

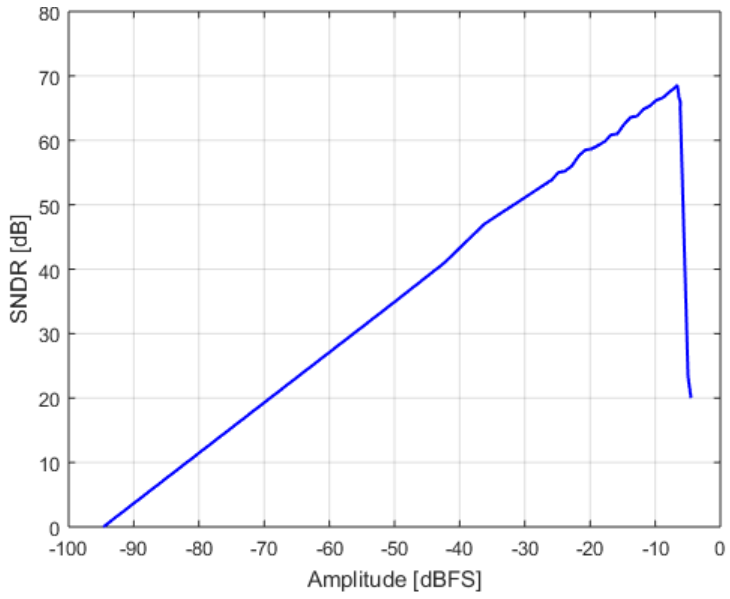

(b)

Figure 5.2.1 (a) Power spectral density of the proposed gingival-mode BPCTDSM at –6.61 dBFS input signal and (b) measured SNDR against the input amplitude.

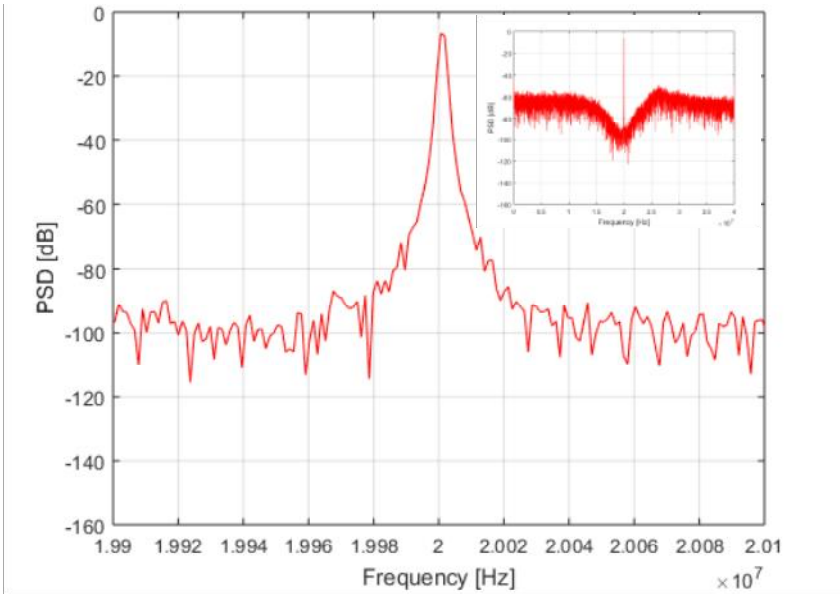

(a)

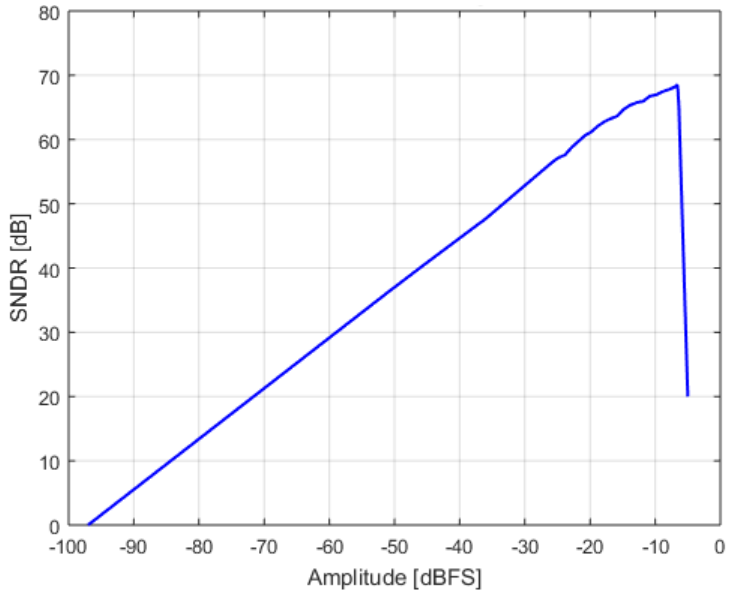

(b)

Figure 5.2.2 (a) Power spectral density of the proposed gingival-mode BPCTDSM with reduced bias current of the opamp at –6.63 dBFS input signal and (b) measured SNDR against the input amplitude.

Table 5.2.1 Specifications of the opamp in each mode with reduced bias current

	Gingival-Mode	**Vascular-Mode**	**Cardiac-Mode**
Gain @ DC	52.99 dB	42.66 dB	38.18 dB
Gain @ F_C	33.78 dB	34.37 dB	33.77 dB
Phase Margin	103.23 °	102.01 °	91.94 °
Unit GBW	1.74 GHz	0.87 GHz	0.85 GHz
Current Consumption	3.54 mA	1.77 mA	1.26 mA

Figure 5.2.3(a) shows the measured power spectral density of the vascular-mode BPCTDSM at –5.56 dBFS input signal, where the maximum SNDR of 67.84 dB is achieved. The minimum detectable signal amplitude is –90.2 dBFS, which indicates a DR of 84.65 dB, as shown in Figure 5.2.3(b). Figure 5.2.4(a) shows the measured power spectral density of the vascular-mode BPCTDSM, with reducing the bias current of the opamp in half, at –5.25 dBFS input signal, where the maximum SNDR of 70.03 dB is achieved. The minimum detectable signal amplitude is –93.66 dBFS, which indicates a DR of 88.42 dB, as shown in Figure 5.2.4(b). Figure 5.2.5(a) shows the measured power spectral density of the cardiac-mode BPCTDSM at –4.98 dBFS input signal, where the maximum SNDR of 69.86 dB is achieved. The minimum detectable signal amplitude is –93.01 dBFS, which indicates a DR of 88.03 dB, as shown in Figure 5.2.5(b). Figure 5.2.6(a) shows the measured power spectral density of the cardiac-mode BPCTDSM,

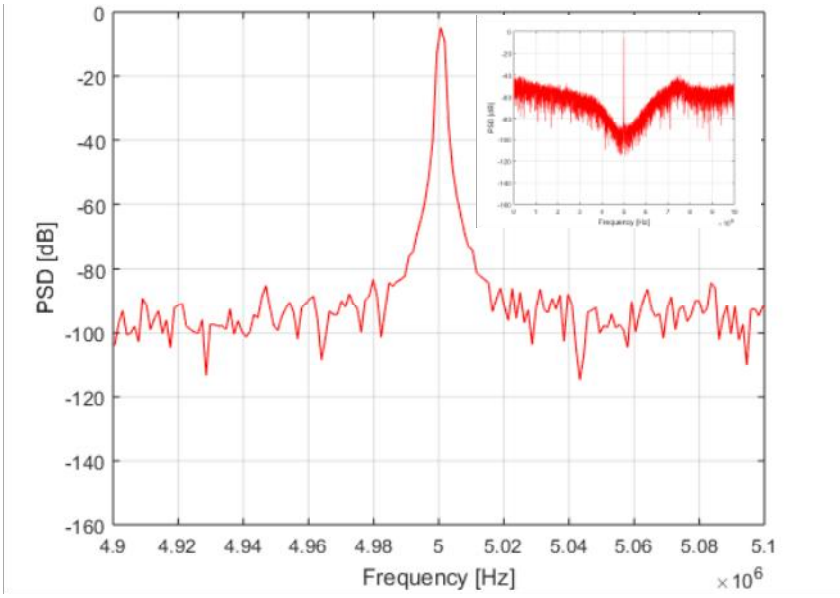

(a)

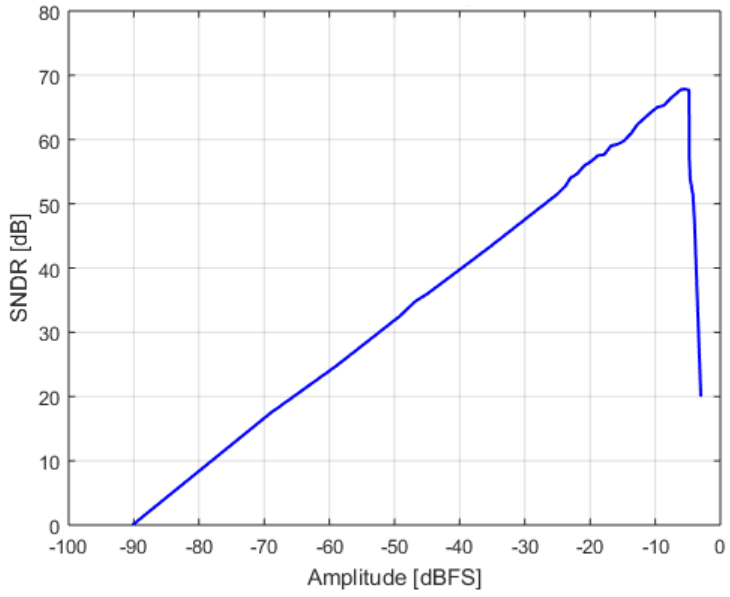

(b)

Figure 5.2.3 (a) Power spectral density of the proposed vascular-mode BPCTDSM at –5.56 dBFS input signal and (b) measured SNDR against the input amplitude.

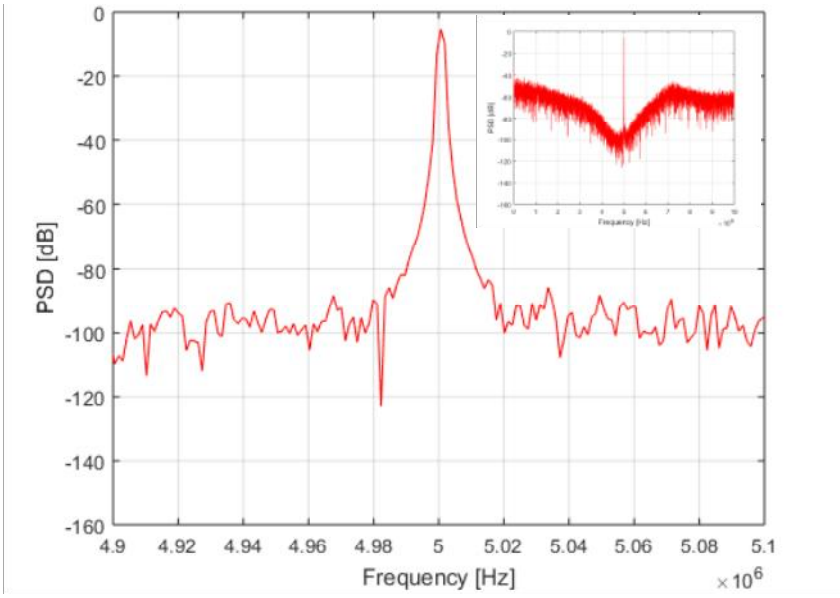

(a)

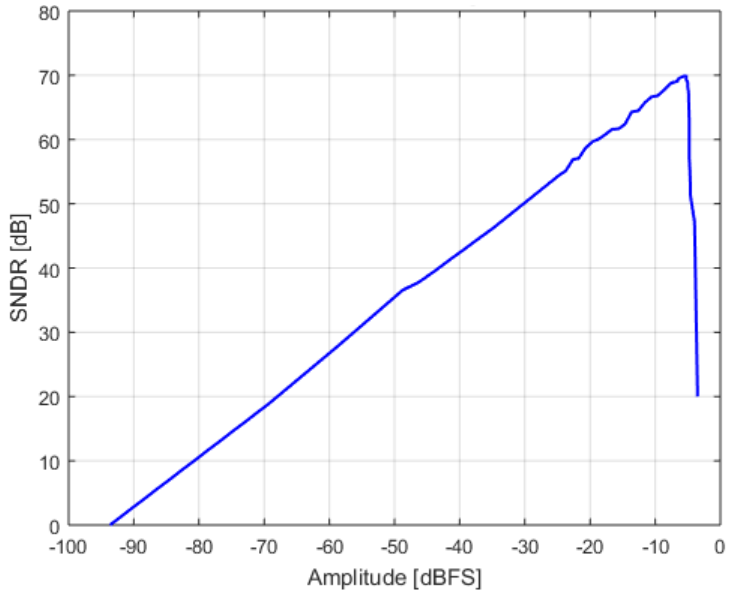

(b)

Figure 5.2.4 (a) Power spectral density of the proposed vascular-mode BPCTDSM with reduced bias current of the opamp at –5.25 dBFS input signal and (b) measured SNDR against the input amplitude.

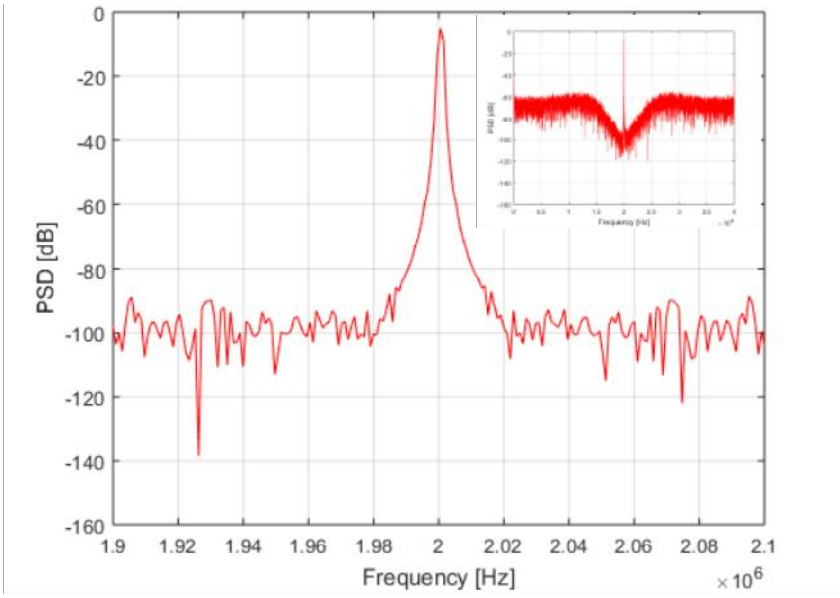

(a)

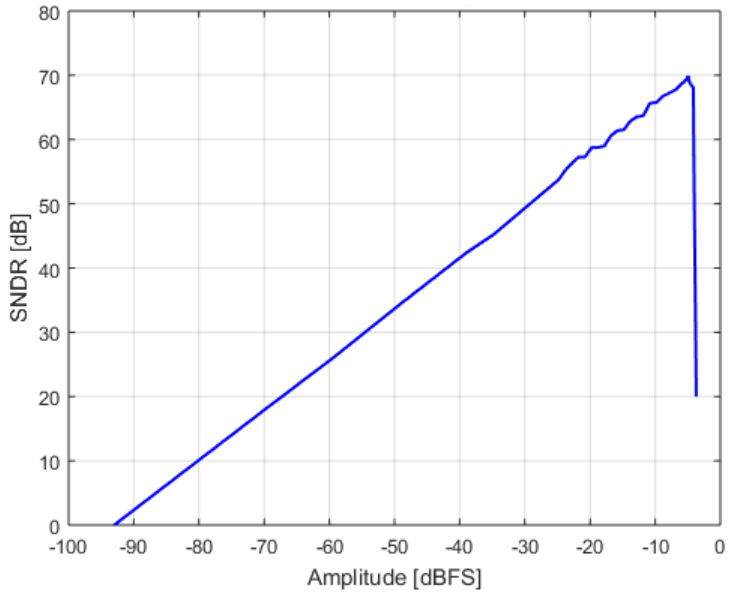

(b)

Figure 5.2.5 (a) Power spectral density of the proposed cardiac-mode BPCTDSM at –4.98 dBFS input signal and (b) measured SNDR against the input amplitude.

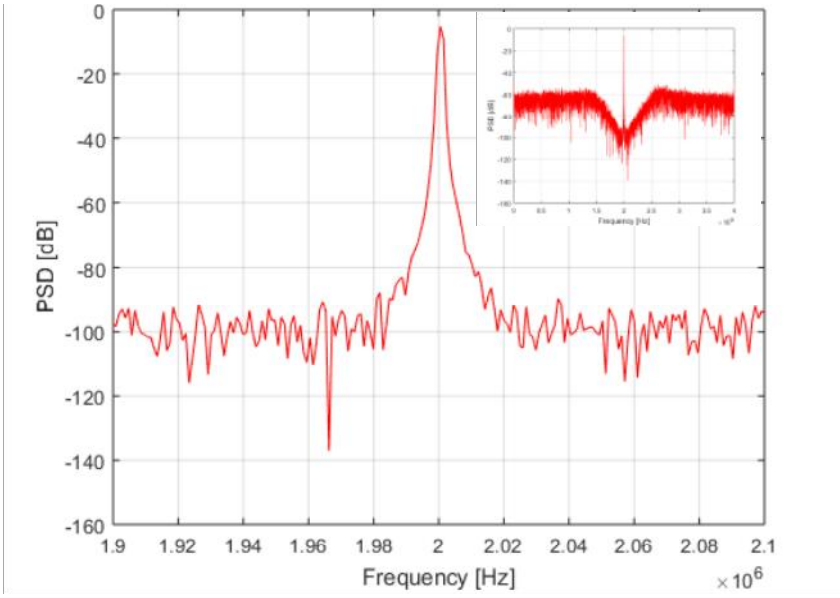

(a)

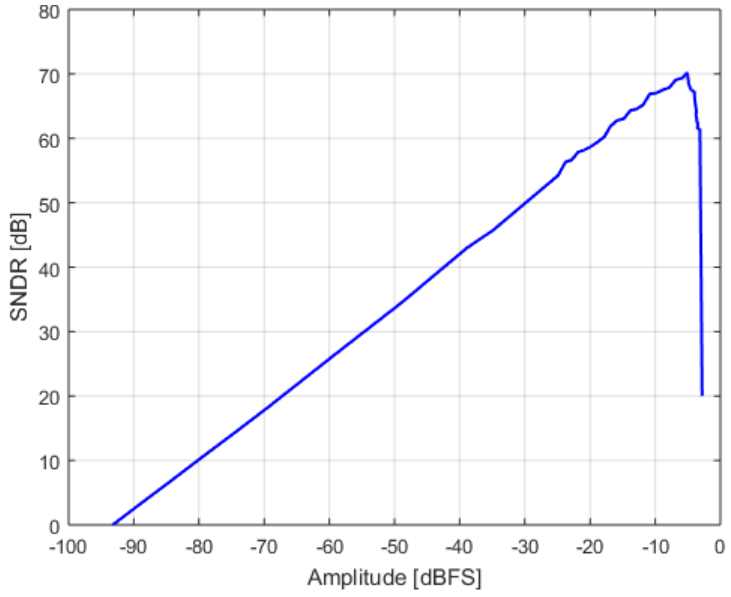

(b)

Figure 5.2.6 (a) Power spectral density of the proposed cardiac-mode BPCTDSM with reduced bias current of the opamp at –5.09 dBFS input signal and (b) measured SNDR against the input amplitude.

Table 5.2.2 Performance summary

Specification	This Work	JSSC 2016	JSSC 2014	JSSC 2008	JSSC 2003
Order	4/6/6	6	4	4	4
F_C [MHz]	20/5/2	200	24	0–12.6	60
F_S [MHz]	80/20/8	800	800	40	80
F_B [MHz]	0.2	25	24	0.31	0.27
DR [dB]	90.39/88.42/88.15	70	60	76	86
SNDR [dB]	68.58/70.03/70.2	69	58	71	78
Supply [V]	1.8	1.2	1.2	1.8	3
Power [mW]	25.75/18.77/14.73	35	12	115	24
FOM* [dB]	159.3/158.7/159.5	158.5	153.0	140.3	156.5

*FOM = DR + 10log(F_B/Power)

with reducing the bias current of the opamp in half, at –5.09 dBFS input signal, where the maximum SNDR of 70.2 dB is achieved. The minimum detectable signal amplitude is –93.24 dBFS, which indicates a DR of 88.14 dB, as shown in Figure 5.2.6(b). Table 5.2.2 compares the performance of our multi-mode BPCTDSM against other designs. Our modulator exhibits better figure-of-merit (FOM) than any other references.

CHAPTER 6

CONCLUSION

We have presented a multi-mode BPCTDSM that achieves wide DR by using a proposed high Q single-opamp resonator. The wide DR multi-mode BPCTDSM can be applied to CW Doppler receiver for pencil probe applications, which requires wide DR to detect the received CW Doppler signal that consists of a large stationary signal and small Doppler signal. Analog mixers in the conventional CW Doppler receiver, which are the main reason to limit the performance of the receiver and consume lots of power, can be replaced with a digital mixer by using a BPCTDSM. The center frequency of the implemented BPCTDSM can be adjusted to 2 MHz, 5MHz, and 20 MHz for measuring the blood velocities in heart, vessel, and gingiva. A wide DR BPCTDSM can be achieved by using a high Q resonator, which is affected mainly by the finite GBW of the utilized opamp in the resonator. As the center frequency of the BPDSM increases, the requirements for an opamp increases to achieve a higher Q, resulting in an increase of overall power consumption. We proposed a high Q single-opamp resonator, which can alleviate the effect of finite GBW of the opamp to Q and relaxes the requirements to the opamp. The multi-mode BPCTDSM is implemented in 180nm CMOS technology with a

supply voltage of 1.8 V. The measurement results show the effectiveness of the proposed high Q single-opamp resonator. A certain level of performance is maintained even if the bias current of the opamp is reduced, which results in the decrease of GBW of the opamp. The DR of 90.39 dB, 88.42 dB and 88.15 dB, the maximum SNDR of 68.58 dB, 70.03 dB, and 70.2 dB, and the power consumption of 25.5 mW, 18.6 mW, and 14.7 mW are achieved in gingival-mode, vascular-mode, and cardiac-mode BPCTDSMs, respectively.

BIBLIOGRAPHY

[1.1.1] Thomas L. Szabo, "Diagnostic Ultrasound Imaging: Inside Out," Elsevier Academic Press, 2004.

[1.1.2] J. Scampini, "Overview of ultrasound imaging systems and the electrical components required for main subfunctions." Maxim Integ., Tech. Doc. AP4696, May 2010.

[1.1.3] M. Ali, D. Magee, and J. Dasgupta, "Signal processing overview of ultrasound systems for medical imaging," Texas Intr., Tech. Doc. SPRAB12, Nov. 2008.

[1.1.4] B. A.J. Angelsen, H. Torp, S. Holm, K. Kristoffersen, and T.A. Whittingham, "Which transducer array is best?," *Eur. J. Ultrasound*, vol. 2, no. 2, pp. 151–164, Apr. 1995.

[1.1.5] D. A. Christopher, P. N. Burns, J. Armstrong, and F. S. Foster, "A high-frequency continuous-wave Doppler ultrasound system for the detection of blood flow in the microcirculation," *Ultrasound Med. Biol.*, vol. 22, no. 9, pp. 1191–1203, Sep. 1996.

[1.1.6] N. S. Anavekar and J. K. Oh, "Doppler echocardiography: A contemporary review," *J. Cardiology*, vol. 54, no. 3, pp. 347–358, Dec. 2009.

[1.1.7] L. L. Lay, S. J. Carey, J. V. Hatfield, and C. M. Gregory, "Receiving electronics for intra-oral ultrasound probe," in *Proc. IEEE Int. Biomed. Circuits Syst.*, Sep. 2004.

[1.2.1] D. maulik, "Physical principles of Doppler ultrasonography," in *Doppler ultrasound in obstetrics and gynecology*, 2nd ed. Mineola, NY: Springer, 2005, pp. 9–17.

[1.2.2] N. Skubas, "Principles of echocardiography for the anesthesiologist," *Greek E. J. Perioper. Med.*, vol. 1, pp. 26–39, 2003.

[1.3.1] M. S. Kassam, C. W. Lau, R. S. C. Cobbold, and K. W. Johnston, "Directional CW Doppler ultrasound using a double-heterodyne demodulator," *IEEE*

Ultrasonics Symp. Boston, Nov. 1980.

[1.3.2] A. Shahein, M. Afifi, M. Becker, N. Lotze, and Y. Manoli, "A power-efficient tunable narrow-band digital front end for bandpass sigma-delta ADCs in digital FM receivers," *IEEE Trans. Circuits Syst. II, Exp. Briefs*, vol. 57, no. 11, pp. 883–887, Nov. 2010.

[1.3.3] J. Scampini, "Continuous-wave Doppler (CWD) design challenges in compact ultrasound-imaging equipment," Maxim Integ., Tech. Doc. AP4455, Sep. 2016.

[2.1.1] R. Schreier and G. C. Temes, "Introduction," in Understanding delta-sigma data converter, Piscataway, NJ: Wiley-Interscience, 2005, pp. 1–20.

[2.1.2] I. Galton, "Why dynamic-element-matching DACs work," *IEEE Trans. Circuits Syst. II, Exp. Briefs*, vol. 57, no. 2, pp. 69–74, Feb. 2010.

[2.1.3] R. Schreier and G. C. Temes, "Bandpass and quadrature delta-sigma modulation," in Understanding delta-sigma data converter, Piscataway, NJ: Wiley-Interscience, 2005, pp. 139–178.

[2.2.1] M. Ortmanns and F. Gerfers, "Continuous-time ΔΣ modulators," in Continuous-time sigma-delta A/D conversion fundamentals, performance limits and robust implementations, Heidelberg, Berlin: Springer, 2006, pp. 39–84.

[2.2.2] M. Ortmanns and F. Gerfers, "DAC nonidealities in continuous-time ΔΣ modulators," in Continuous-time sigma-delta A/D conversion fundamentals, performance limits and robust implementations, Heidelberg, Berlin: Springer, 2006, pp. 85–115.

[2.2.3] J. Lim, Y. Cho, K. Jung, J. Park, J. Choi, and J. Kim, "A wide-band active-RC filter with a fast tuning scheme for wireless communication receivers," in *Proc. IEEE CICC*, Sep. 2005.

[2.2.4] D. Li, D. Basak, Y. Zhang, Z. Fu, and K.-P. Pun, "Improving power efficiency for active-RC delta-sigma modulators using passive-RC low-pass filter in feedback," *IEEE Trans. Circuits Syst. II, Exp. Briefs*, to be published.

[3.1.1] R. Zanbaghi, P. K. Hanumolu, and T. S. Fiez, "An 80-dB DR, 7.2-MHz bandwidth single-opamp biquad based CT ΔΣ modulator dissipating 13.7-mW,"

IEEE J. Solid-State Circuits, vol. 48, no. 2, pp. 487–501, Feb. 2013.

[3.1.2] H. Chae, J. Jeong, G. Manganaro, and M. P. Flynn, "A 12 mW low power continuous-time bandpass ΔΣ modulator with 58 dB SNDR and 24 MHz bandwidth at 200 MHz IF," *IEEE J. Solid-State Circuits*, vol. 49, no. 2, pp. 405–415, Feb. 2014.

[3.1.3] K. Matsukawa, Y. Mitani, M. Takayama, K. Obata, H. Dosho, and A. Matsuzawa, "A fifth-order continuous-time delta-sigma modulator with single-opamp resonator," *IEEE J. Solid-State Circuits*, vol. 45, no. 4, pp. 697–706, Apr. 2010.

[3.1.4] G.-H. Weng, T.-A. Wei, E. Alpman, C.-T. Fu, Y.-T. Tseng, and T.-H. Lin, "An 8.5MHz 67.2dB SNDR CTDSM with ELD compensation embedded twin-T SAB and circular TDC-based quantizer in 90nm CMOS," in *Symp. VLSI Circuits, Dig. Tech. Papers*, Jun. 2014, pp. 1–2.

[3.1.5] S. Zeller, C. Muenker, and R. Weigel, "A 9th-order continuous time ΣΔ-ADC with X-coupled differential single-opamp resonators," in *Proc. IEEE MWSCAS*, Aug. 2011.

[3.1.6] J. Wagner, S. Reich, R. Ritter, J. Anders, and M. Ortmanns, "Finite GBW in single opamp CT ΣΔ modulators," in *Proc. IEEE ICECS*, Dec. 2016.

[3.1.7] T. Salo, S. Lindfors, and K. Halonen, "A low-voltage single-opamp 4th-order band-pass ΔΣ-modulator," in *Proc. IEEE ISCAS*, May 2001.

[3.1.8] M. Ortmanns, F. Gerfers, and Y. Manoli, "Compensation of finite gain-bandwidth induced errors in continuous-time sigma-delta modulators," *IEEE Trans. Circuits Syst. I, Reg. Papers*, vol. 51, no. 6, pp. 1088–1099, Jun. 2004.

[4.1.1] S.-I. Na, S. Kim, Y. Yang, and S. Kim, "Estimating non-ideal effects within a top-down methodology for the design of continuous-time delta-sigma modulators," *J. Semiconductor Technology and Science*, vol. 16, no.3, pp. 319–329, Jun. 2016.

[4.2.1] L. J. Breems, R. Rutten, R. H. M. Veldhoven, and G. Weide, "A 56 mW continuous-time quadrature cascaded ΣΔ modulator with 77 dB DR in a near

zero-IF 20 MHz band," *IEEE J. Solid-State Circuits*, vol. 42, no. 12, pp. 2696–2705, Dec. 2007.

[4.2.2] C.-Y. Ho, W.-S. Chan, Y.-Y. Lin, and T.-H. Lin, "A quadrature bandpass continuous-time delta-sigma modulator for a tri-mode GSM-EDGE/UMTS/ DVB-T receiver, *IEEE J. Solid-State Circuits*, vol. 46, no. 11, pp. 2571–2582, Nov. 2011.

[4.2.3] K. Matsukawa, Y. Mitani, M. Takayama, K. Obata, Y. Tokunaga, S. Sakiyama, and S. Dosho, "A 69.8 dB SNDR 3rd-order continuous time delta-sigma modulator with an ultimate low power tuning system for a worldwide digital TV-receiver," in *Proc. IEEE CICC*, Sep. 2010.

[4.2.4] S.-H. Wu, T.-K. Kao, Z.-M. Lee, P. Chen, and J.-Y. Tsai, "A 160MHz-BW 72dB-DR 40mW continuous-time ΔΣ modulator in 16nm CMOS with analog ISI-reduction technique," in *IEEE ISSCC Dig. Tech. Papers*, Feb. 2016, pp. 280–281.

한글초록

연속-시간 도플러 신호는 펜슬 타입의 트랜스듀서를 통해 높은 주파수 대역의 신호를 인체에 송신하고 수신기에서 혈액의 이동속도에 따른 주파수 변화를 관찰함으로써 빠른 혈류의 속도를 측정하는 데 사용된다. 연속-시간 도플러 신호 수신기에서 전달받는 신호는 고정된 조직으로부터 발생하는 강한 신호와 혈류로부터 발생하는 약한 도플러 신호로 구성된다. 도플러 신호는 고정된 조직으로부터 발생하는 강한 신호보다 40–60 dB 작기 때문에 넓은 동적 범위가 요구된다. 기존의 연속-시간 도플러 신호 수신기에서 성능을 제한하는 가장 큰 요소인 아날로그 혼합기는 밴드-패스 연속-시간 델타-시그마 모듈레이터를 사용함으로써 디지털 영역으로 그 동작을 이동시킬 수 있어 효율적인 연속-시간 도플러 신호 수신기를 구현할 수 있다. 밴드-패스 연속-시간 델타-시그마 모듈레이터의 성능은 공진기의 품질 인자에 의해 결정되며, 공진기의 품질 인자가 중심 주파수 대 신호 대역폭 비율보다 작으면 모듈레이터의 성능에 큰 영향을 미친다. 연속-시간 도플러 신호 수신기의 경우, 중심 주파수가 크게는 수십 MHz에 달하는 반면 신호의 대역폭은 200 kHz 내외에 불과하므로 밴드-패스 연속-시간 델타-시그마 모듈레이터가 넓은 동작 대역을 얻기 위해서는 높은 품질 인자를 가지는 공진기가 요구된다.

최근, 전력 소모를 줄이기 위해 단일-연산증폭기 기반의 공진기가 널리

사용되고 있다. 하지만, 두 개의 증폭기를 사용하는 기본 구조와 비교했을 때 증폭기의 유한 이득-대역폭에 의한 공진기의 품질 인자 저하가 크게 나타난다. 증폭기의 유한 이득-대역폭을 높이기 위해 다단계 증폭기가 효과적으로 사용될 수 있으나 중심 주파수 대 신호 대역폭 비율이 커짐에 따라 증폭기의 요구조건은 점점 높아지고 전력 소모량도 늘어나게 된다. 증폭기의 유한 이득-대역폭에 의해 변형된 잡음 전달 함수를 복구하기 위해 모듈레이터의 계수를 보상하는 방식은 중심 주파수 대 신호 대역폭 비율이 커지더라도 증폭기의 요구조건은 변하지 않은 채 계수만 변경하여 모듈레이터의 성능을 높일 수 있다는 장점이 있다. 하지만 변경된 계수들을 단위 저항과 단위 커패시터로 구현하기 어려운 경우가 발생할 수 있으며 단위 소자를 사용하지 않아 발생하는 미스매치가 모듈레이터의 성능을 저하시킬 수 있다. 증폭기의 유한 이득-대역폭은 루프 필터 내에 지연으로 나타낼 수도 있어 지연을 보상하는 피드백 통로를 추가하는 것으로도 증폭기의 유한 이득-대역폭의 영향을 보상할 수 있지만 추가 피드백 디지털-아날로그 변환기가 사용된다는 단점이 있다.

증폭기의 유한 이득-대역폭이 공진기의 품질 인자를 저하시키는 영향을 완화시키기 위해 포지티브 피드백 저항을 사용하여 공진기의 품질 인자를 보상할 수 있는 단일-연산증폭기 기반의 공진기를 제안하였으며 이는 증폭기의 설계 요구조건을 높이지 않은 상태에서 적용 가능하다. 또한,

공진기의 계수들을 단위 저항과 단위 커패시터로 구현하여 소자 사이에서 발생하는 미스매치를 최소화하고 추가되는 포지티브 피드백 저항 또한 단위 저항을 사용하여 구현 가능하다. 본 연구에서는 품질 인자를 보상할 수 있는 단일-연산증폭기 기반의 공진기를 이용하여 펜슬 프로브 어플리케이션에 적용 가능한 다중 모드의 넓은 동작 대역을 갖는 밴드-패스 연속-시간 델타-시그마 모듈레이터를 제안하였다. 제안된 모듈레이터는 2 MHz, 5 MHz, 및 20 MHz의 중심 주파수를 사용하여 각각 심장, 혈관 및 잇몸의 혈류를 측정하는 데 적용 가능하며 제안된 공진기를 활용함으로써 증폭기가 유한한 이득-대역폭을 가지더라도 넓은 동작 대역을 만족할 수 있다. 칩은 180 nm CMOS 공정으로 구현되었으며 0.845 mm^2의 면적을 가진다. 측정을 통해 각각 심장, 혈관 및 잇몸 모드에서 88.15 dB, 88.42 dB 및 90.39 dB의 동작 대역과 70.2 dB, 70.03 dB 및 68.58 dB의 최대 신호 대 잡음 비율을 얻었으며 1.8 V 공급 전압에서 14.73 mW, 18.77 mW 및 25.75 mW의 전력을 소모하였다.

주요어 : 넓은 동작 대역; 밴드-패스 연속-시간 델타-시그마 모듈레이터; 높은 공진 인자; 단일-연산증폭기 기반의 공진기; 유한 이득-대역폭.

학 번 : 2011-20806